

**Investigations of Faraday Rotation Maps of
Extended Radio Sources in order to determine
Cluster Magnetic Field Properties**

Dissertation
der Fakultät für Physik
der
Ludwig-Maximilians-Universität München

angefertigt von
Corina Vogt
aus Görlitz

München, den September 3, 2004

1. Gutachter: Prof. Dr. Rashid Sunyaev
2. Gutachter: Prof. Dr. Andreas Burkert

Tag der mündlichen Prüfung: 26. November 2004

”Vom Himmel lächelte der Herr zufrieden – weil es genau dies war, was Er wollte, nämlich daß jeder die Verantwortung für sein Leben in die eigenen Hände nahm. Schließlich war dies ja die größte Gabe, die Er seinen Kindern gegeben hatte: Die Fähigkeit selbst zu wählen und zu bestimmen.

Nur Männer und Frauen mit der heiligen Flamme im Herzen hatten den Mut, sich Ihm zu stellen. Und nur sie kannten den Weg, der zurück zu Seiner Liebe führte, weil sie am Ende begriffen hatten, daß das Unglück keine Strafe, sondern eine Herausforderung war.”

aus *Der Fünfte Berg* - Paulo Coelho

Contents

Abstract	xi
1 Introduction	1
1.1 Magnetised Plasma	2
1.2 Observing Astrophysical Magnetic Fields	5
1.2.1 The Zeeman Effect	5
1.2.2 Polarisation of Optical Starlight	6
1.2.3 Synchrotron Emission	7
1.2.4 Faraday Rotation	10
1.3 The state of the Art - Cluster Magnetic Fields	16
1.3.1 Radio Haloes and Relics	16
1.3.2 Rotation Measures	18
1.4 Some Statistical Tools	21
1.4.1 Least-Squares & Error Weighting	21
1.4.2 Autocorrelation and Power Spectra	23
1.4.3 Bayesian Statistics	25
1.4.4 Structure of the Thesis	28
2 Is the <i>RM</i> Source-Intrinsic or not?	29
2.1 A Long Lasting Debate	29
2.2 The Argument Reconsidered	31
2.3 Statistics Comes to Aid	33
2.4 Avoidable and Unavoidable Correlated Noise	36
2.5 Results	37
2.6 Conclusions	39
3 Measuring Magnetic Field Power Spectra	41
3.1 Introduction	41
3.2 The Philosophy	42
3.3 The Method	45
3.3.1 Real Space Formulation	45
3.3.2 Fourier Space Formulation	48
3.3.3 Testing the Model & Influences of Observational Artefacts	51
3.3.4 Assessing the Influence of the Window Function	53
3.4 Application	55
3.4.1 3C75, 3C465 & Hydra A - the Data	55

3.4.2	Real Space Analysis	56
3.4.3	Fourier Space Analysis	58
3.4.4	Test the model and assess the influence of the window function	60
3.5	Results	64
3.6	Conclusions	67
4	<i>Pacman</i> – A new <i>RM</i> Map Making Algorithm	71
4.1	Introduction	71
4.2	The new <i>Pacman</i> algorithm	73
4.2.1	The Idea	73
4.2.2	The Basic Algorithm	74
4.2.3	Improving Quality	78
4.2.4	Restricting Gradients	78
4.2.5	Topological Defects	78
4.2.6	Spurious Points	79
4.2.7	Multi-Frequency Fits	79
4.2.8	Additional Information	80
4.3	Testing the Algorithm	80
4.4	Statistical Characterisation of Improved <i>RM</i> Maps	81
4.4.1	Gradient Vector Product Statistic	81
4.4.2	Error Under or Over Estimation	82
4.4.3	Magnetic Power Spectra	83
4.5	Application to Data	83
4.5.1	Abell 2255E	83
4.5.2	Hydra North	88
4.5.3	The Quest for Hydra South	94
4.6	Lessons & Conclusions	97
5	A Bayesian View on Faraday Rotation Maps	99
5.1	Introduction	99
5.2	Maximum Likelihood Analysis	100
5.2.1	The Covariance Matrix C_{RM}	100
5.2.2	Evaluation of the Likelihood Function	103
5.2.3	Binning and Rebinning	103
5.2.4	The Algorithm	104
5.3	Testing the Algorithm	106
5.4	Application to Hydra A	108
5.4.1	The Data Δ	108
5.4.2	The Window Function	109
5.5	Results and Discussion	111
5.6	Conclusions	115
	Conclusions	117
	Bibliography	119
	Acknowledgements	125

List of Tables

2.1	<i>A</i> and <i>V</i> statistics of various data sets	38
3.1	Results for the correlation analysis	66

List of Figures

1.1	$n\pi$ -ambiguity	12
1.2	RM distribution of Hydra A	14
1.3	Radio map of the Coma cluster	17
1.4	RM cluster point source sample	20
2.1	RM distribution of PKS 1246-410	30
2.2	$RM - \varphi_0$ scatter plots	32
3.1	RM autocorrelation function of A400, A2634 and Hydra A	57
3.2	Magnetic autocorrelation function $w(r)$ in real space	58
3.3	Magnetic energy spectrum for A2634, A400 and Hydra A	59
3.4	Dependence of the magnetic field strength on the integration interval	60
3.5	Testing the window function by calculating $\chi^2(x_\perp)$	61
3.6	Fourier transformed RM map of A400 and Hydra A	62
3.7	Response function for A2634	63
3.8	Expected and measured magnetic field in comparison	64
3.9	Determination of the spectral indices	65
4.1	Flow chart of the algorithm <i>Pacman</i>	75
4.2	Testing the <i>Pacman</i> algorithm	81
4.3	Comparison between <i>Pacman</i> and standard fit RM maps	85
4.4	A pixel-by-pixel comparison between <i>Pacman</i> and standard fit RM Map	86
4.5	Various Power Spectra for the Cluster Source A2255E	87
4.6	A pixel-by-pixel comparison between <i>Pacman</i> and standard fit RM Map for Hydra A North	89
4.7	Various power spectra for Hydra North	91
4.8	Various power spectra for Hydra North using different thresholds	92
4.9	A reduced χ^2_{vij} and \tilde{V} map of Hydra North	93
4.10	Individual RM fits across an RM jump	95
4.11	Various power spectra for Hydra South	96
5.1	Generated RM maps with known power spectrum	106
5.2	Calculated power spectra for the test case	107
5.3	RM maps of Hydra North	109
5.4	Window function in comparison to the RM dispersion	110
5.5	Various power spectra for different scaling exponents α_B	112
5.6	The log-likelihood for various scaling parameters α_B	113

5.7	Two power spectra for different inclination angles θ	114
5.8	The integrated magnetic field energy E_B for various scaling parameters α_B	114

Abstract

In this work, statistical analyses and tests of Faraday rotation measure (RM) maps are developed in order to determine the properties of the magnetic fields which are associated with the plasma in clusters of galaxies.

Whenever linearly polarised radio emission passes through a magnetised medium, the plane of polarisation is rotated – an effect called Faraday rotation effect. It is sometimes debated which magnetised medium is mainly responsible for this Faraday rotation. Does the magnetised medium close to the source of the polarised radio emission dominate or does the Faraday rotation mainly take place in the magnetised medium which is located between the source and the observer, the intra-cluster gas? After investigations which provide confidence that the Faraday rotation is mainly due to the magnetised medium which is external to the source, the question arises how one can analyse the observed Faraday rotation maps to gain insight into cluster magnetic field properties. Therefore, a statistical approach to analyse the RM maps in terms of autocorrelation function and power spectrum is developed and applied to the data. Realising that map making artefacts and noise in the data have a noticeable effect on this analysis, especially for measuring power spectra, a new RM map making algorithm called *Pacman* is introduced. *Pacman* provides high quality RM maps which allow precise estimates of power spectra. In order to use the full potential of these maps, an accurate power spectrum estimator based on Bayesian maximum likelihood methods is developed and successfully applied to characterise cluster magnetic field properties such as magnetic field strength, magnetic field autocorrelation length and the shape of the magnetic power spectrum.

In this work, the origin of the high Faraday rotation measures found for polarised radio galaxies in clusters is investigated. The two most likely sites of Faraday rotation are within magnetic fields local to the radio source, or within magnetic fields located in the foreground intra-cluster medium (ICM). In order to distinguish these two scenarios in the data, a gradient alignment statistic aimed to find correlations between the intrinsic polarisation angle φ_0 and RM maps is introduced. Such correlations were proposed to result in the case of source local RM screens. The statistic is applied to a number of extended radio sources in galaxy clusters (PKS 1246-410, Cygnus A, Hydra A, and 3C465). In no case, a significant large-scale alignment of φ_0 and RM maps is detected. However, a significant small-scale co-alignment is found in all cases. This co-alignment can be fully identified with map making artefacts through a suitable statistical test. At present, there is no existing evidence for Faraday rotation local to radio lobes. Given the existing independent pieces of evidence, it is concluded that the observed Faraday screens are produced by intra-cluster magnetic fields.

Having realised this, a statistical analysis of RM maps is developed. The auto-

correlation function and similarly the Fourier power spectrum of an RM map of an extended background radio source can be used to measure the components of the magnetic autocorrelation and power spectrum tensor within a foreground Faraday screen. It is possible to reconstruct the full non-helical part of this tensor in the case of an isotropic magnetic field distribution statistics. The magnetic field strength, the energy spectrum and the autocorrelation length λ_B can be obtained from this non-helical part alone. It is demonstrated that λ_B can differ substantially from λ_{RM} , which is the characteristic scale of an RM map. In typical astrophysical situations $\lambda_{RM} > \lambda_B$.

Strategies to analyse observational data are discussed, taking into account – with the help of a window function – the limited extent of the polarised radio source, the spatial distribution of the electron density and the average magnetic energy density in the screen, and allowing for noise reducing data weighting. The effects of possible observational artefacts, and strategies to avoid them are briefly discussed.

This technique of Faraday rotation measure map analysis is applied to three galaxy clusters, Abell 400, Abell 2634 and Hydra A, in order to estimate cluster magnetic field strengths, length scales and power spectra under the assumption that typical field values scale linearly with the electron density. The difficulties involved in the application of the analysis to observational data are investigated. Magnetic power spectra are derived for the three clusters and influences on their shapes caused by the observational nature of the data such as limited source size and resolution are discussed. Various tests are successfully applied to validate the assumptions of the analysis.

It is shown that magnetic fluctuations are probed on length scales ranging over at least one order of magnitude. Using this range for the determination of the magnetic field strengths of the central cluster gas yields $3 \mu\text{G}$ in Abell 2634, $6 \mu\text{G}$ in Abell 400 and $12 \mu\text{G}$ in Hydra A as conservative estimates. The magnetic field autocorrelation length λ_B is determined to be 4.9 kpc for Abell 2634, 3.6 kpc for Abell 400 and 0.9 kpc for Hydra A. For the three clusters studied, it is found that $\lambda_{RM} \simeq 2...4\lambda_B$. Furthermore, in a response analysis it is investigated if it is possible to determine the spectral slopes of the power spectra. It is found that the integrated numbers can be reliably determined from this analysis but differential parameters such as spectral slopes have to be treated differently.

Realising that such a statistical analysis can be corrupted by map making artefacts, a new method to calculate Faraday rotation measure maps from multi-frequency polarisation angle data sets is proposed. In order to solve the so called $n\pi$ -ambiguity problem which arises from the observational ambiguity of the polarisation angle determined only up to additions of $\pm n\pi$, where n is an integer, it is suggested to use a global scheme. Instead of solving the $n\pi$ -ambiguity for each data point independently, the proposed algorithm, which was chosen to be called *Pacman* (Polarisation Angle Correcting rotation Measure ANalysis), solves the $n\pi$ -ambiguity for a high signal-to-noise region “democratically” and uses this information to assist the computations in adjacent low signal-to-noise areas.

The *Pacman* algorithm is tested on artificially generated RM maps and applied to two polarisation data sets of extended radio sources located in the Abell 2255 and Hydra A cluster. The RM maps obtained using *Pacman* are compared to RM maps obtained employing already existing methods. The reliability and the robustness of *Pacman* is demonstrated. In order to study the influence of map making artefacts, which are imprinted by wrong solutions to the $n\pi$ -ambiguities, and of the error treatment of

the data, magnetic field power spectra were calculated from various RM maps. The sensitivity of the statistical analysis to artefacts and noise in the RM maps is demonstrated and thus, the importance of an unambiguous determination of RM values and of an understanding of the nature of the noise in the data. Statistical tests are presented and performed in order to estimate the quality of the derived RM maps, which demonstrate the quality improvements due to *Pacman*.

In order to take the window function properly into account in the measurement of the magnetic power spectrum of clusters of galaxies, a Bayesian maximum likelihood analysis of RM maps of extended radio sources is developed. Using this approach, it is also possible to determine the uncertainties in the measurements. This approach is applied to the RM map of Hydra A North and the power spectrum of the cluster magnetic field is derived. For Hydra A, a spectral index of a Kolmogorov type turbulence is observed over at least one order of magnitude in k -space. A dominant scale at about 3 kpc is found on which the magnetic power is concentrated. Furthermore, the influence of the assumptions about the sampling volume (described by a window function) on the magnetic power spectrum is investigated and it is found that the typical magnetic energy density scales approximately linearly with the electron density (and not with the field strength as assumed before). The central magnetic field strength is determined to be $7 \pm 2 \mu\text{G}$ for the most likely geometries.

Chapter 1

Introduction

Magnetic fields are ubiquitous throughout the Universe. It is the magnetic field of the planet earth which prevents the solar wind and the high energy particles ejected by the Sun from reaching the atmosphere and thus, making life possible on Earth. It is the magnetic field of the Sun which strongly influences the appearance of Sun's surface and generates stunning events such as sun spots, arches and flares. It is the magnetic field of pulsars which drives the exactly timed radio pulses coming from these objects on the sky.

However, magnetic fields are detected not only on small scales such as planets, like Earth or Jupiter, or stars, but also on large scales in galaxies and on even larger scales in clusters of galaxies. They are also observed on intermediate scales, i.e. in molecular clouds which are the progenitor of proto stars, thus, magnetic fields are detected in the interstellar medium (ISM) where the star forming takes place. Magnetic fields are believed to be important for these star forming processes but to what extent and during what stages the magnetic fields become important is still under debate. However, magnetic fields remove angular momentum from proto stellar clouds making star formation possible (for a review, see Bourke & Goodman 2004).

For the ISM, the magnetic energy density is at least comparable to the energy density of the thermal gas, it is comparable to the energy of cosmic rays and it is also comparable to the energy of the turbulent motion of the ISM. On larger scales in clusters of galaxies, magnetic fields also introduce an additional pressure component to the energy balance of the cluster gas, which is a hot plasma. The dynamical importance of magnetic fields for this plasma is still under debate. However, a complete description of the state of the plasma, and in particular the role of particle transport processes, requires knowledge of the strength and the morphologies of intra-cluster magnetic fields.

Related to these processes magnetic field constrain the heat conductivity. Transport coefficients, e.g. heat conduction, are determined by the rate of change of (thermal) electron momenta. In a fully magnetised plasma, particles experience momentum changes not only through mutual collisions but perhaps primarily due to the Lorentz force which leads to a confinement of their motion mainly along field lines. These field lines may be tangled on scales less than the Coloumb mean free path, which is about tens of kilo parsecs in a cluster atmosphere. Treating the field tangling scale in a simple approximation as an effective mean free path, one can estimate the change

in heat conductivity due to the field. The comparison of the actual heat conductivity with the Spitzer value which relies on the Coulomb interaction will determine the value of the effective mean free path. However, if the heat conductivity is too high, observed phenomena such as cooling cores and cold fronts of clusters cannot be sustained. Therefore, thermal conduction must be inhibited by sufficiently strong magnetic fields ordered on small scales.

Magnetic fields are also fundamental to the observed properties of jets and lobes in radio galaxies. They might be a primary element in the generation of relativistic outflows from accreting black holes. One important property of magnetic fields related to this and other processes is that magnetic fields couple relativistic gas with non-relativistic gas dynamically.

Cosmologically, magnetic fields might not have influenced the formation of the large scale structures of the universe. However they shaped and supported the galaxy formation and evolution and therefore it is necessary to understand the influences the magnetic fields have on astrophysical processes.

And yet, other key questions which remain to be answered are: Where did these fields come from? When were the first magnetic fields generated? Which mechanisms did amplify the fields to the strength of which they are observed? Knowing the present day structure, strength and coherence length scales is important to discriminate between the theoretical models for amplification mechanisms – mostly described as dynamo mechanisms – and models for magnetic field seeding.

In order to determine the properties of magnetic fields, the observation of the Faraday rotation effect is a very powerful tool. It is observed whenever linearly polarised radio emission passes through a magnetised plasma (such as the cluster gas). It manifests itself by rotation of the plane of polarisation. In this work, the analysis of Faraday rotation observations is used to shed light on the properties of the effect producing magnetic fields, and thus, to shed light on possible influences of magnetic fields on astrophysical processes and objects.

Before the observation of astrophysical magnetic fields, in particular the detection of the Faraday rotation effect is explained in Sect. 1.2, some basics about magnetised plasma is described in Sect. 1.1. Since this work focuses on the analysis of Faraday rotation data in order to derive properties of cluster magnetic fields, a short review of the current knowledge about magnetic fields in clusters of galaxies is given in Sect. 1.3. Since this work made extensive use of statistics in order to understand observations and to fit models to them, Sect. 1.4 is devoted to statistical tools.

1.1 Magnetised Plasma

Plasma is often referred to as the 'fourth' state of matter. In a plasma, electrons and ions can move independent from each other. Since there are positive and negative charges moving freely, electrical currents are easily induced. Therefore a plasma is very sensitive to electrical and magnetic fields. On the other side, the free charges can also produce electrical and magnetic fields.

Assuming a globally neutral plasma of electrons and protons being all at the same temperature T_0 with a mean particle density n_0 and assuming for this plasma local

thermodynamical equilibrium, the charge densities are given by

$$n_q(\phi) = n_0 \exp\left(\frac{-q\phi}{T_0}\right) \simeq \left(1 - \frac{q\phi}{T_0}\right), \quad (1.1)$$

where ϕ is the electrostatic potential, $q = e, -e$ is the charge of the particle. Furthermore, it is assumed that the plasma is weakly coupled, i.e. $|q\phi/T_0| \ll 1$. A test charge q_t placed at the origin would experience an electrostatic potential ϕ following from the Poisson equation

$$\nabla^2 \phi = 4\pi e [n_e(\phi) - n_p(\phi)] - 4\pi q_t \delta^{(3)}(\vec{x}), \quad (1.2)$$

where n_e and n_p indicate the electron and the proton density, respectively. Substituting Eq. (1.1) into Eq. (1.2) results in

$$\nabla^2 \phi - \frac{1}{\lambda_D^2} \phi = -4\pi \delta^{(3)}(\vec{x}), \quad (1.3)$$

where

$$\lambda_D = \sqrt{\frac{T_0}{8\pi n_0 e^2}} \quad (1.4)$$

is the Debye length. This length can be interpreted such that for a test particle the Coulomb potential has the usual Coloumb form but it will be suppressed at large distances $r > \lambda_D$ by a Yukawa term ($\exp(-r/\lambda_D)$).

There are two other quantities, the plasma frequency ω_p and the gyrofrequency or Larmor frequency ω_L , which characterise a magnetised plasma. The plasma frequency ω_p is the oscillations frequency of the electrons when they are displaced from their equilibrium configuration in a background of approximately fixed ions

$$\omega_p = \sqrt{\frac{4\pi n_0 e^2}{m_e}}, \quad (1.5)$$

where m_e is the electron mass. The gyrofrequency ω_L is found by considering the particle motion in a static uniform magnetic field. The particle is spiralling around the magnetic field line with the frequency

$$\omega_L = \frac{|q| B}{\gamma m_e c}, \quad (1.6)$$

where $\gamma = 1/\sqrt{1 - v^2/c^2}$ is the Lorentz factor.

As mentioned already, plasma and electromagnetic fields interact strongly. Magnetohydrodynamics (MHD) describes this interaction on macroscopic time and length scales (see, for example, Jackson 1975; Sturrock 1994). This description is an approximation that holds when charge separation effects are negligible. In this approach, the matter is described as a single conducting fluid. Furthermore, it assumes that the simple form of Ohm's law is valid but it ignores the displacement current of Ampère's Law, i.e. $\partial \vec{E} / \partial t = 0$. Under these assumption and expressed in Gaussian units,

Maxwell's equations take the following pleasant form

$$\nabla \cdot \vec{E} = 4\pi\rho, \quad (1.7)$$

$$\nabla \cdot \vec{B} = 0, \quad (1.8)$$

$$\nabla \times \vec{E} = -\frac{1}{c} \frac{\partial \vec{B}}{\partial t}, \quad (1.9)$$

$$\nabla \times \vec{B} = \frac{4\pi}{c} \vec{j}, \quad (1.10)$$

where \vec{E} is the electrical field strength, \vec{B} is the magnetic field strength, ρ is the charge density and \vec{j} is the current density.

In this description, Ohm's law is given by

$$\vec{j}' = \sigma \vec{E}', \quad (1.11)$$

where σ is the conductivity and the primed quantities refer to the rest frame of the fluid. Since most astrophysical fluids are electrically neutral and nonrelativistic, $\vec{j}' = \vec{j}$ and $\vec{E}' = \vec{E} + (\vec{v} \times \vec{B})/c$. Thus, Ohm's law becomes

$$\vec{j} = \sigma \left(\vec{E} + \frac{1}{c} \vec{v} \times \vec{B} \right). \quad (1.12)$$

Multiplying this expression by $\nabla \times$ and substituting Maxwell's Eq. (1.9) and Eq. (1.10) into Ohm's law¹ results in the magnetic diffusivity equation

$$\frac{\partial \vec{B}}{\partial t} = \nabla \times (\vec{v} \times \vec{B}) + \eta (\nabla^2) \vec{B}, \quad (1.13)$$

where $\eta = c^2/\sigma 4\pi$ is the magnetic diffusion coefficient as approximated here to be spatially constant. The first term $\nabla \times (\vec{v} \times \vec{B})$ in the equation above is the *dynamo* or *convective* term. It describes the tendency of magnetic fields lines to be frozen in and the amplification of magnetic fields. The second term $\eta (\nabla^2) \vec{B}$ on the right hand side of Eq. (1.13) is the *diffusive* term which represents the resistive leakage of magnetic field lines across the conducting fluid. Thereby, it describes the dissipation of magnetic fields since it allows dilution and cancellation of magnetic fields.

Since the diffusive and the convective term are competing, it is useful to introduce a dimensionless parameter, *the magnetic Reynolds number* R_M ,

$$R_M \simeq \frac{|\text{convective term}|}{|\text{diffusive term}|} = \frac{L^{-1}vB}{\eta L^{-2}B}, \quad (1.14)$$

so that $R_M \simeq Lv/\eta$, where L is a length characteristic of the spatial variation of the magnetic field. Note that this equation only refers to orders of magnitude. Depending on whether $R_M \ll 1$ or $R_M \gg 1$ the convective or the diffusive term, respectively, dominates. In typical astrophysical situations, R_M is a large number and thus, the diffusive term is negligible. An interesting regime to note is an infinite magnetic Reynolds number being equivalent to infinite conductivity (ideal MHD). In this regime, the magnetic field lines are frozen in the plasma and thus, follow the movements of the fluid.

¹while using the equality for $(\nabla^2)\vec{B} = \nabla(\nabla \cdot \vec{B}) - \nabla \times (\nabla \times \vec{B})$ and Maxwell's Equation $\nabla \cdot \vec{B} = 0$.

1.2 Observing Astrophysical Magnetic Fields

There are several methods in order to measure strength and structure of astrophysical magnetic fields (e.g. Ruzmaikin et al. 1988; Kronberg 1994; Beck et al. 1996; Widrow 2002, for reviews). The four widely used methods are the observation of the Zeeman effect, the analysis of the observed polarisation of optical starlight scattered on dust particles, the observation of synchrotron emission and, the analysis of multi-wavelength studies of linearly polarised radio sources in order to measure the Faraday rotation effect. Their use for different scales and objects in the universe is strongly dependent on the sensitivity of the signal which is aimed to be detected by these methods as briefly described in the following.

1.2.1 The Zeeman Effect

One of the most obvious possibilities is the effect of magnetic fields on spectral lines named after and discovered by Pieter Zeeman in 1896. Twelve years after its discovery, it was used by Hale (1908) to detect magnetic fields in sun spots which was the first observations of extraterrestrial magnetic fields. Bolton & Wild (1957) proposed to use the Zeeman splitting of the 21 cm line of neutral hydrogen to detect magnetic fields in the ISM. Ten years later, this measurement was realised by Verschuur (1968).

In the absence of external fields, the electronic energy levels of atoms are independent on the direction of the total angular momentum \mathbf{J} (orbital angular momentum \mathbf{L} plus spin \mathbf{S}) of electrons. The energy levels are degenerate. An external magnetic field removes the degeneracy and leads to a dependence of the energy levels on the orientation of the angular momentum with respect to the magnetic field. The energy levels are split into $2j + 1$ equidistant levels, where j is the quantum number associated with the total angular momentum \mathbf{J} .

The energy difference between neighbouring levels which are split by the influence of the magnetic field is

$$\Delta E = g\mu B, \quad (1.15)$$

where $\mu = e\hbar/2m_e c = 9.3 \times 10^{-21} \text{ erg G}^{-1}$ is Bohr's magneton and g is the Lande factor, which relates the angular momentum of an atom to its magnetic moment. Once this energy difference ΔE is measured, the magnetic field can be determined without the need of any further assumption. Furthermore, Zeeman splitting is sensitive to the total magnetic field strength in contrast to other methods such as synchrotron emission and Faraday rotation which are sensitive to the magnetic field component perpendicular and parallel to the line of sight, respectively. Thus, the observation of the Zeeman effect is the most direct way to detect astrophysical magnetic fields strength.

Unfortunately, the Zeeman effect is extremely difficult to detect. The line shift resulting from the energy splitting is

$$\frac{\Delta\nu}{\nu} = 1.4g \frac{B}{\nu} \frac{\text{Hz}}{\mu\text{G}}. \quad (1.16)$$

For the two most commonly used spectral lines for Zeeman splitting observations in astrophysics, which are the 21 cm neutral hydrogen absorption line and the 18 cm OH molecule line, $\Delta\nu/\nu \simeq 10^{-9}g(B/\mu\text{G})$ and thus, assuming a magnetic field of 10 μG , the line shift is only about 30 MHz. The line shift due to thermal Doppler line

broadening is $\Delta\nu/\nu \simeq v_T/c \simeq 6 \times 10^{-7} (T/100\text{K})^{1/2}$, where v_T and T are the mean thermal velocity and temperature of the atoms, respectively. Thus, the line half-width is about $\Delta\nu = 10^4$ MHz at $T = 100$ K. Therefore, Zeeman splitting is described rather as a change in the shape of a thermally broadened line (abnormal broadening).

Given these observational constraints, the detection of the Zeeman effect is confined to regions of low temperatures and high magnetic fields such as molecular clouds in our own Galaxy. Observation of the Zeeman effect in Galactic neutral hydrogen (HI) regions lead to magnetic field strengths of $\overline{B} \simeq 2 \dots 10 \mu\text{G}$, where the higher values were detected in dark clouds and HI shells (Heiles 1990, and references therein). At present however, due to its weakness the Zeeman effect has not been detected in extragalactic sources yet.

1.2.2 Polarisation of Optical Starlight

Davis & Greenstein (1951) proposed a connection between polarised optical star light and the galactic magnetic field. Optical starlight is polarised by elongated dust grains orientating in a preferred direction in an interstellar magnetic field. For prolate grains, one of the short axis aligns parallel to the magnetic field direction. The dust grains absorb star light which is polarised along the long axis of the grains, i.e. perpendicular to the magnetic field direction. As a result, the transmitted radiation possesses a polarisation direction parallel to the magnetic field.

The polarising mechanism can also be understood by considering that scattering and absorption of starlight on dust grains occurs differently at different planes. Therefore the correlation between the degree of polarisation due to absorption and the degree of starlight reddening due to scattering is a good argument for the connection between polarised optical starlight and magnetic fields. Light of unreddened stars is usually non-polarised. In a typical situation the degree of star light polarisation is increased by 3% along a path of 1 kpc in the Galactic plane.

So far, some attempts have been made to interpret starlight polarisation measurements with respect to the interstellar field. The classical study of polarisation directions of 1800 stars in the Galactic plane was performed by Mathewson & Ford (1970). Starlight polarisation for external galaxies have also been performed (e.g. for M51, Scarrott et al. 1987). One can statistically analyse such maps for fluctuations in the polarisation direction in order to get information on the chaotic magnetic field component. However, the starlight polarisation data alone cannot distinguish between field directions allowing reversals of the polarity without observable consequences.

For a more comprehensive understanding of starlight polarisation data, one needs to understand how grains align with the magnetic field (see e.g. Martin 1978, Chap. 9) which would be based on concepts of the dust particle structure. Unfortunately, this understanding does not exist yet. However, a simple statement about the compositions of the dust grains can be drawn from the fact that the particle align with their long axis perpendicular to the magnetic field line direction. Ferromagnetic particles, such as iron filings, would exactly align the opposite way and therefore dust grains can not be ferromagnetic. The most favoured alignment mechanism is paramagnetic relaxation proposed by Davis & Greenstein (1951).

Apart from the need of better theories describing the alignment of dust particles in a magnetic field, the interpretation of starlight polarisation observation is limited due

to two other effects. Firstly, the polarisation can be obscured by the anisotropic scattering of starlight on dust. This polarising scattering and the polarising absorption of optical star light can not be observationally distinguished. Secondly, since the starlight polarisation effect is depending on extinction, it is self-obscuring leading to a decrease in luminosity (for a more detailed discussion, see Scarrott et al. 1987). On the other hand, optical measurements have normally higher resolution than radio observations allowing the detection of small-scale fluctuations in galactic magnetic fields.

1.2.3 Synchrotron Emission

Relativistic electrons which are spiralling around magnetic field lines radiate synchrotron emission in the direction of their movement (Rybicki & Lightman 1979), which is partially polarised. Therefore, synchrotron emission is a direct indicator for magnetic fields. The total synchrotron emission is used as an estimate of the magnetic field strength and its polarisation indicates the uniformity and structure of magnetic fields.

The emissivity $J(\nu, E)$ of a single relativistic electron spiralling around a magnetic field line depending on frequency ν and electron energy E is determined by

$$J(\nu, E) \propto B_{\perp} \left(\frac{\nu}{\nu_c} \right)^{1/3} f \left(\frac{\nu}{\nu_c} \right), \quad (1.17)$$

where B_{\perp} is the component of the magnetic field perpendicular to the line of sight, the critical frequency $\nu_c \equiv \nu_L(E/m_e c^2)^2$, the Larmor frequency $\nu_L = (eB_{\perp}/2\pi m_e c)$ and the cut-off function $f(\nu/\nu_c)$ approaches unity for $(\nu/\nu_c) \rightarrow 0$ and vanishes rapidly for $(\nu/\nu_c) \gg 1$. Furthermore, from this equation it can be seen that the synchrotron emission at frequency ν is dominated by electrons possessing energies of about $E \simeq m_e c^2 \sqrt{\nu/\nu_L}$.

The relativistic electron energy distribution $n_e(E)$ is normally described by a power law which is valid over some range of energy

$$n_e(E)dE = n_{e0} \left(\frac{E}{E_0} \right)^{-\alpha} dE, \quad (1.18)$$

where α is the spectral index (e.g. $\alpha = 2.6, \dots, 3.0$ for a typical spiral galaxies) and $n_{e0} \equiv n_e(E_0)$ gives the normalisation.

The synchrotron emissivity of an ensemble of relativistic electrons is determined by

$$j_{\nu} = \int dE J(\nu, E) n_e(E) \quad (1.19)$$

As mentioned earlier, the synchrotron emission at frequency ν is dominated by electrons with energy $E \simeq m_e c^2 \sqrt{\nu/\nu_L}$ which allows to approximate Eq. (1.17) by $J(\nu, E) \propto B_{\perp} \nu_c \delta(\nu - \nu_c)$. One can now substitute $E \propto \sqrt{\nu_c/\nu_L}$ and $dE \propto d\nu_c/\sqrt{\nu_L \nu_c}$ into this approximation. From the equation for the Larmor frequency, it also follows that $\nu_L \propto B_{\perp}$. Inserting this into Eq. (1.19) and integrating the resulting expression with respect to ν_c yields

$$j_{\nu} \propto n_{e0} \nu^{(1-\alpha)/2} B_{\perp}^{(1+\alpha)/2}. \quad (1.20)$$

This synchrotron emission spectrum can then be related to the energy density of relativistic electrons $\epsilon_{re} = \int dE n_e(E)E$ and the magnetic field B_\perp (Burbidge 1956; Pacholczyk 1970; Leahy 1991). Suppose that the total flux density S_ν emitted by the source in a frequency range $\nu_1 < \nu < \nu_2$ and the angular size of the source Θ are measured, one can obtain the relativistic energy density ϵ_{re}

$$\epsilon_{re} = \int_{\nu_1}^{\nu_2} dE n_e(E)E = aB^{-3/2}\Theta^2 S_\nu(\nu_0), \quad (1.21)$$

where ν_0 is a characteristic frequency between ν_1 and ν_2 and the proportionality factor a is a known function which depends on ν_1, ν_2 and α (see e.g. chap. 7, Pacholczyk 1970).

If the relativistic particle energy can be determined by an additional method, the estimation of the magnetic field strength follows from Eq. (1.21). Often this necessary information is not directly available. Therefore, an additional assumption is often used by considering the total energy budget

$$\epsilon_{tot} = \epsilon_{re} + \epsilon_{rp} + \epsilon_B, \quad (1.22)$$

where $\epsilon_B = B^2/8\pi$ is the magnetic energy density, ϵ_{re} and ϵ_{rp} are the relativistic energy density of the electrons and of the heavy particles, respectively. Assuming that the energy density of heavy particles is proportional to the energy density of the relativistic electrons $\epsilon_{rp} = k\epsilon_{re}$, where $k \sim 100$ for relativistic particles in our Galaxy (Beck et al. 1996), Eq. (1.22) reduces to

$$\epsilon_{tot} = (1 + k)\epsilon_{re} + \epsilon_B. \quad (1.23)$$

In order to estimate the magnetic field strength, one can either assume equipartition between the energies $(1 + k)\epsilon_{re} = \epsilon_B$ or minimise ϵ_{tot} with respect to B . The latter results in

$$\frac{\partial \epsilon_{tot}}{\partial B} = 0 = -(1 + k) \frac{3c}{2} \Theta^2 S_\nu(\nu_0) B^{-5/2} + \frac{1}{4\pi} B, \quad (1.24)$$

where Eq. (1.21) was used, leading to a magnetic field estimate of the form $B^{7/2} \propto \Theta^2 S_\nu(\nu_0)$. However, the equipartition assumption leads to a similar result which deviates only by a factor of 8/6. As an example using equipartition arguments, Niklas (1995) determined a mean magnetic field strength of $9 \pm 3 \mu G$ from a sample of 74 spiral galaxies, however larger field strength have been locally detected in Galaxies (Beck et al. 1996).

The assumption of equipartition or minimum energy is continuously under debate. It is not clear if this assumption is valid over all length and time scales. On large length scales or long time scales equilibrium might have developed whereas on small length or short time scales this may not be true. However, in our Galaxy the assumption of equipartition can be tested, since independent measurement of the relativistic electron energy density and of the relativistic proton energy density exist. A combination of these information yields an excellent agreement with the estimates using the equipartition assumption (Beck 2001).

Another possibility to use synchrotron emission in order to estimate the magnetic field strength for extragalactic sources is the comparison between inverse Compton (IC) X-ray emission and radio synchrotron emission (Harris & Grindlay 1979;

Rephaeli et al. 1987). The presumption for this case is that the X-ray emission is a result from the inverse Compton scattering of fossil cosmic microwave background photons with the synchrotron radiation producing relativistic electrons.

The IC X-Ray emissivity is proportional to the energy density in the photon field of the fossil photons ϵ_{CMB} . On the other hand, the synchrotron emissivity is proportional to the magnetic energy density ϵ_B . This leads to a simple proportionality between IC X-Ray L_{IC} and synchrotron radio L_{syn} luminosity: $L_{syn}/L_{IC} \propto \epsilon_B/\epsilon_{CMB}$. Since the IC X-ray and synchrotron emission are generated by the same relativistic particle population, IC X-ray and synchrotron emission share the same spectral index Γ which is related to the α of the relativistic electron energy distribution by $\Gamma = 2\alpha + 1$. Assuming $\Gamma = -1$, the magnetic field can be expressed by (e.g. Harris & Grindlay 1979; Rephaeli et al. 1987)

$$B = 1.7 (1 + z)^2 \left(\frac{S_r \nu_r}{S_x \nu_x} \right)^{0.5} \mu\text{G}, \quad (1.25)$$

where S_r and S_x are the radio and the X-ray flux densities at observed radio ν_r and X-ray ν_x frequencies, respectively.

In order to use this method for the estimation of magnetic fields in galaxy cluster atmospheres, the principal difficulty in this approach is the confusion due to thermal emission from the galaxy cluster gas. One can separate these two components by spectroscopical means in X-ray observations. The IC emission has a harder power law spectrum in comparison with the thermal bremsstrahlung emission. However, lower limits on cluster magnetic field strength of about 0.2 . . . 0.4 have been determined by studying IC emission by Rephaeli et al. (1994, 1999) and Fusco-Femiano et al. (2000, 2001).

So far the discussion was concentrated on the estimation of the magnetic field strength. As mentioned earlier the observation of polarisation of synchrotron emission can be used as an indicator for the structure of the magnetic field in which the synchrotron radiating particle are moving. Synchrotron emission of a single relativistic electron is elliptically polarised. For any distribution of particles that varies smoothly with the pitch angle (angle between magnetic field and velocity), the elliptical component will cancel out. Thus, the radiation will be partially linearly polarised.

The degree of polarisation p can be defined as the ratio of the linearly polarised emission intensity and the total intensity. For a homogenous magnetic field and a homogenous electron distribution following Eq. (1.18) and if the source is optically thin to synchrotron radiation (valid for galaxies and clusters), the degree of polarisation is

$$p_{max} = \frac{\alpha + 1}{\alpha + 7/3}, \quad (1.26)$$

where α is the spectral index of the electron energy distribution (Eq. 1.18), (Ginzburg & Syrovatskii 1964; Ruzmaikin et al. 1988). For $\alpha = 2.7$ for our Galaxy, the degree of polarisation would be $p_{max} = 0.73$. However, in normal spiral galaxies where the magnetic field is never strictly homogeneous, values for a degree of polarisation of $p = 0.3$ were measured in the upper limit, values between $p = 0.1 \dots 0.2$ are normal. The difference between the intrinsic polarisation of synchrotron emission and the observed one can be explained by various effects which lead to the depolarisation of the synchrotron emission. These effects can be explained by the presence of a

fluctuating magnetic field component along the line of sight, inhomogeneities in the electron distribution and the magnetised medium, Faraday depolarisation (see next section) and beam smearing (e.g. Sokoloff et al. 1998).

Based on heuristic arguments, Burn (1966) proposed a simple expression for the depolarisation by a fluctuating magnetic field component

$$p = p_{max} \frac{\overline{B}^2}{B^2}, \quad (1.27)$$

where \overline{B}^2 is the energy density in the regular field component and B^2 is the energy density in the total field. This expression is to be treated in a statistical sense. Ignoring for the moment other depolarising effects, this means that only about 20% of the total magnetic field in spirals is associated with the large scale/regular component of the field. This ratio would be higher if other depolarising effects were included.

1.2.4 Faraday Rotation

When linearly polarised radio emission propagates through a magnetised plasma, the polarisation plane of the radiation is rotated. This phenomenon is called Faraday rotation effect. Its detection is one of the most powerful methods to study magnetic field structure and strength.

An electromagnetic wave is usually described as

$$\vec{E}(\vec{x}, t) = \vec{E}_0 \exp i(\vec{k}\vec{x} - \omega t), \quad (1.28)$$

where \vec{k} is the wave vector and \vec{E}_0 is the amplitude of the wave. For the study of wave propagation in a uniform cold magnetised plasma, where for convenience $\vec{B} = (0, 0, B)$, one has to evaluate the following wave equation

$$\vec{k} \times (\vec{k} \times \vec{E}) + \frac{\omega^2}{c^2} \mathcal{K} \cdot \vec{E} = 0, \quad (1.29)$$

where \mathcal{K} is the dielectric tensor (see e.g. chap. 6, Sturrock 1994). If the wave propagation along the magnetic field in a plasma is considered the dispersion relation is different for right and left hand circularly polarised waves introducing a phase velocity difference as the waves pass through it. A linearly polarised wave propagating along the magnetic field in a magnetised plasma can be decomposed into opposite-handed circularly polarised waves which are then characterised by different wave vectors

$$k_{R,L} = \frac{\omega}{c} \left[1 - \frac{\omega_p^2}{\omega(\omega \pm \omega_g)} \right]^{1/2}, \quad (1.30)$$

where R and $+$ corresponds to right hand, L and $-$ corresponds to left hand polarisation, respectively, (as seen by the observer receiving the waves), ω_p is the plasma frequency (Eq. 1.5) and ω_g is the gyrofrequency $\omega_g = eB/m_e c$. Assuming the same amplitude E_0 , their wave description is

$$E_1 = 2E_0 \cos \left(\frac{k_L + k_R}{2} z - \omega t \right) \cos \left(\frac{k_L - k_R}{2} z \right) \quad (1.31)$$

$$E_2 = 2E_0 \sin \left(\frac{k_L + k_R}{2} z - \omega t \right) \sin \left(\frac{k_L - k_R}{2} z \right). \quad (1.32)$$

The combined wave will be still linearly polarised but the direction of the electric field vector will change with distance z .

If φ denotes the angle between electric field vector and the x -axis so that $\tan \varphi = E_2/E_1$, one can derive

$$\varphi = \frac{k_L - k_R}{2}z, \quad (1.33)$$

and thus,

$$\frac{d\varphi}{dz} = \frac{1}{2}(k_L - k_R). \quad (1.34)$$

In radio astronomy, propagation over large distances are considered over which ω_p and ω_g are slowly varying, i.e. $k_{R,L}$ are also changing slowly with distance d . Therefore, φ can be expressed by

$$\varphi = \int_0^d dl \frac{d\varphi}{dl} = \int_0^d dl \frac{1}{2}(k_L - k_R). \quad (1.35)$$

In the intra-cluster space, magnetic fields of the order of $\sim \mu\text{G}$ are observed leading to gyro-frequencies of about $\omega_g \sim \text{Hz}$. Furthermore, the electron density in the plasma is about $n_e \sim 10^{-3} \text{ cm}^{-3}$ causing plasma frequencies of a few $\omega_p \sim \text{kHz}$. Radio astronomy detects radiation at frequencies from 10 MHz to 10 GHz. Thus, the wave vector $k_{R,L}$ can be approximated (using $\omega_g, \omega_p \ll \omega$) by

$$k_{R,L} = \frac{\omega}{c} \left[1 - \frac{\omega_p^2}{2\omega^2} \left(1 \mp \frac{\omega_g}{\omega} \right) \right]. \quad (1.36)$$

Inserting this expression into Eq. (1.34) yields

$$\frac{d\varphi}{dl} = \frac{\omega_p^2 \omega_g}{2c\omega^2} \quad (1.37)$$

and substituting the expressions for ω_g and ω_p yields

$$\frac{d\varphi}{dl} = \frac{2\pi n_e e^3 B}{m_e^2 c^2 \omega^2}. \quad (1.38)$$

Hence, integrating this expression gives the total rotation of the plane of polarisation over the path of propagation of radio waves

$$\varphi = \frac{e^3}{2\pi m_e^2 c^2} \frac{1}{\nu^2} \int_0^d dl n_e B_{\parallel} + \varphi_0, \quad (1.39)$$

where the frequency of the wave is expressed as $\nu = \omega/2\pi$ and φ_0 is the intrinsic polarisation angle. So far it was assumed that the electromagnetic wave propagates parallel (or anti-parallel) to the magnetic field. If one considers a more general direction of propagation and still uses the approximation $\omega \gg \omega_g, \omega_p$, one would find that the rotation of the plane of polarisation is still expressed by Eq. (1.39), where B_{\parallel} represents then the magnetic field component parallel to the wave vector \vec{k} .

Equation (1.39) can be written in a more convenient way

$$\varphi = a_0 \lambda^2 \int_0^d dl n_e B_{\parallel} + \varphi_0, \quad (1.40)$$

where $a_0 = e^3/(2\pi m_e^2 c^4)$ is a constant, the wavelength $\lambda = c/\nu$. The proportionality constant between the polarisation angle and the wavelength squared is called rotation measure (RM):

$$RM = a_0 \int_0^d dl n_e B_{\parallel}, \quad (1.41)$$

and thus,

$$\varphi = RM\lambda^2 + \varphi_0. \quad (1.42)$$

By convention, RM is positive (negative) for a magnetic field directed toward (away from) the observer. In order to determine the RM values for a given source, one usually observes the linearly polarised source at at least three different wavelengths. The RM value is then determined for each point of the source using Eq. (1.42) employing a least-squares fit. One major difficulty involved in performing this fit is that the polarisation angle is observationally only constrained to values between 0 and π leaving a freedom of additions of $\pm n\pi$ which leads to the so called $n\pi$ -ambiguity. This problem is illustrated in Fig. 1.1. In this work, a method is proposed in order to solve this problem (see Chapter 4).

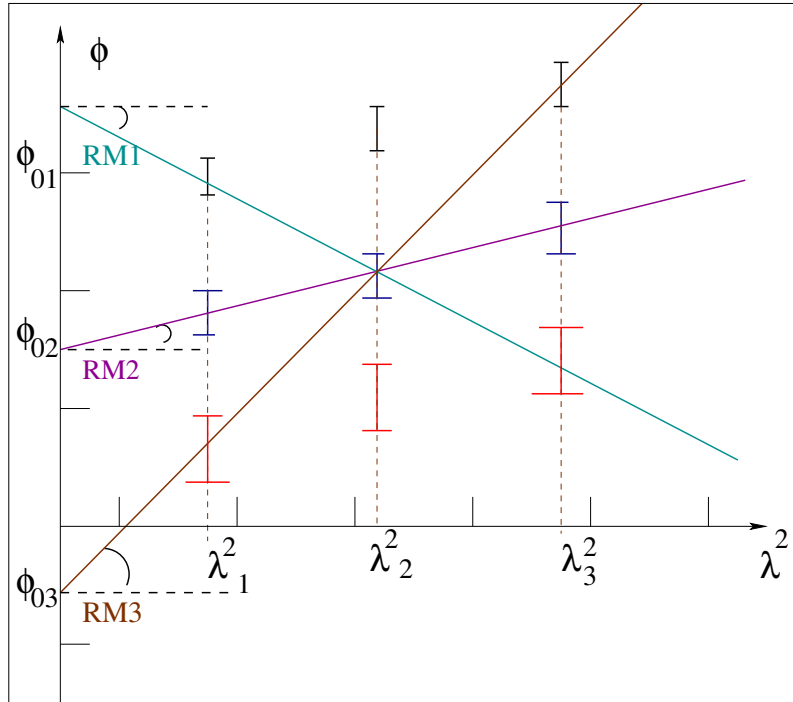


Figure 1.1: The so-called $n\pi$ -ambiguity arising in the determination of the RM is illustrated. The RM is the slope of the linear regression expressed by Eq. (1.42). Clearly, additions of $\pm\pi$ change the slope significantly. This plot is adapted from Ruzmaikin & Sokoloff (1979); Giovannini (2004).

As mentioned in Sect. 1.2.3, the observed degree of polarisation of radiation differs from the expected value meaning that it is substantially depolarised between its origin and the observer. One depolarising effect mentioned is Faraday depolarisation

which is discussed in the following. A first mechanism is observed when the emission region of the polarised radiation coincides with the Faraday rotating region – the Faraday screen. If this region is spatially extended along the line of sight, the emission of polarised radiation by relativistic electrons within the source will occur at different depths experiencing different Faraday rotation angles caused by different path lengths. Eventually this results in a depolarisation of radiation and it is called *internal* or *differential depolarisation*.

If the source is represented by an optically thin slab where magnetic field and thermal electron distribution are both homogeneous, the degree of polarisation can be expressed by (Razin 1958; Burn 1966)

$$p = p_0 \left| \frac{\sin(RM\lambda^2)}{RM\lambda^2} \right|, \quad (1.43)$$

where p_0 is the intrinsic polarisation degree and RM is the total rotation measure produced in the whole slab. If the field is also characterised by a random component, the dependence of polarisation and wavelength λ is smoothed.

A second depolarising effect due to Faraday rotation is caused by the combined action of random magnetic fields and the finite size of a telescope beam. Consider several cells being encompassed by the telescope beam which have differently directed internal magnetic fields and thus, their Faraday rotation differs from cell to cell. Hence, this effect, which is called *external* or *beam depolarisation*, diminishes the resulting polarisation.

It is rather difficult to distinguish between internal and external Faraday depolarisation. However, there are some general rules. If the depolarisation were internal, the most depolarised region should be those with highest $|RM|$ (Garrington & Conway 1991). There should also be a correlation between surface brightness and depolarisation if it were internal. Furthermore, a considerable deviation from the λ^2 - law within a 90° rotation of the polarisation angle should be observed (Burn 1966).

A third depolarising effect is observed due to the finite transmission bandwidth of a telescope receiver. Since any radio telescope receives radiation within a certain wavelength interval $\Delta\lambda$ centred around the observation wavelength λ . This effect is called *bandwidth depolarisation*.

So far the origin of the Faraday rotation effect, its detection and the consequences it has on the polarisation of radiation has been explained. It is left to understand the interpretation of the RM data. In the following, it is assumed that the emission region of polarised radiation is well separated from the Faraday screen and is located behind the screen. This assumption has been challenged by Bicknell et al. (1990) and Rudnick & Blundell (2003). In Chapter 2, this question is discussed in more detail and arguments in favour of the assumption that the Faraday rotation is external to the source will be given.

Considering the Faraday rotation to be external, Eq. (1.41) enables the study of large-scale fields being responsible for the RM together with a model for the thermal electron density distribution normally derived from independent X-ray measurements. A fast estimate of a minimum field strength can be derived by assuming a uniform magnetic field and a constant electron distribution throughout the Faraday screen

$$\langle RM \rangle = a_0 B_{\parallel} n_e L, \quad (1.44)$$

where L is the size of the Faraday screen along the line of sight. However, Faraday rotation distribution are normally patchy indicating a small-scale structure of the magnetic field. In Fig. 1.2, an example of an RM distribution for the source Hydra A is shown where this patchiness clearly can be seen.

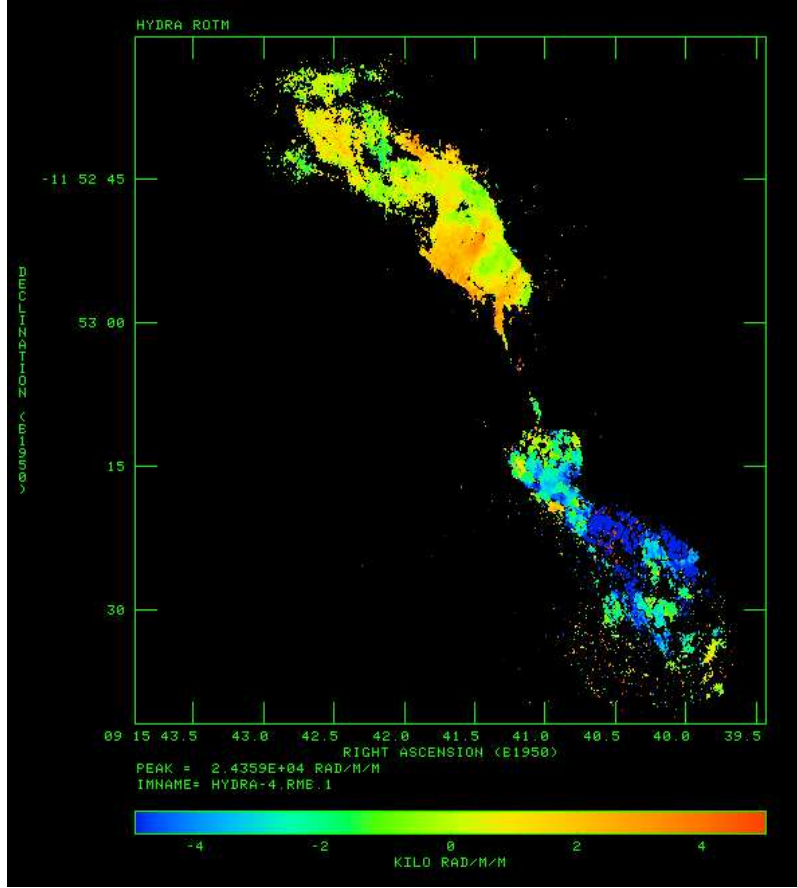


Figure 1.2: Faraday rotation measure distribution of the cluster source Hydra A (adapted from Taylor & Perley 1993). Note that the shape of the RM distribution is due to the shape of the region with polarised emission. However, the Faraday screen is situated in the foreground and goes beyond the shape of the source.

The patchiness of RM distributions indicates that the magnetic fields are not regularly ordered having a coherence length on kpc scale. The simplest model assumes the Faraday screen to consist of cells with a uniform length scale λ_c having a uniform magnetic field B but random directions. The RM for each line of sight through such a Faraday screen would build up in a random walk process. Assuming a Gaussian distribution of the field directions yields a mean value $\langle RM \rangle = 0$ and the dispersion $\langle RM^2 \rangle$ is non zero. Under the assumption of a constant electron density distribution:

$$\langle RM^2 \rangle = a_0^2 \lambda_c \int (n_e B_{\parallel})^2 dl. \quad (1.45)$$

For this cell model, one can use a more realistic description for the electron density

distribution, the so called β -profile (Cavaliere & Fusco-Femiano 1976):

$$n_e(r) = n_{e0}(1 + r^2/r_c^2)^{-3\beta/2}, \quad (1.46)$$

where n_0 is a characteristic electron density (i.e. at the cluster centre $n_{e0} = n_e(0)$), r_c is the cluster radius, and the β parameter fit to the X-ray observations. Assuming this density profile in the calculation of the RM dispersion, the following relation can be derived by integrating Eq. (1.45) (Felten 1996; Feretti et al. 1995)

$$\sqrt{\langle RM^2(r_\perp) \rangle} = \frac{KBn_0r_c^{1/2}\Lambda_c^{1/2}}{(1 + r_\perp^2/r_c^2)^{(6\beta-1)/4}} \sqrt{\frac{\Gamma(3\beta - 0.5)}{\Gamma(3\beta)}}, \quad (1.47)$$

where r_\perp is the projected distance from the cluster centre, Γ is the Gamma function, the constant $K = 624$ if the source lies completely beyond the cluster and $K = 441$ if the source is halfway embedded in the cluster. Usually, the cell size λ_c and the RM dispersion is estimated from the observed RM distribution and the electron density is given by X-ray measurements. The only unknown in Eq. (1.47) is the magnetic field strength B which is then easy to determine.

Crusius-Waetzel et al. (1990) and Goldshmidt & Rephaeli (1993) propose a similar method based on a cell model to evaluate Eq. (1.45) directly. They assume that the field correlation length $l_0 \ll r_c$ and that the characteristic scale for variations of the electron density is small compared to the field correlation length l_0 resulting in

$$\langle RM^2 \rangle = a_0^2 \frac{l_0}{3} \int ds_1 n^2(s_1) \langle B^2(s_1) \rangle, \quad (1.48)$$

where s_1 is some location at the RM distribution. Their analysis also employs a single correlation scale.

This analysis of RM distributions is very oversimplified. A Faraday screen which is build up of uniform cells with uniform fields but random field directions violates Maxwell's equation $\nabla \cdot \vec{B} = 0$. Furthermore, it is most likely that a distribution of length scales exist. In that case, it is also not clear how the cell size λ_c is defined. It might differ significantly from the coherence length of the RM distribution λ_{RM} which in turn is not necessarily equivalent to the coherence length of the magnetic field λ_B .

A completely different method compared to the ones mentioned above was suggested by Kolatt (1998) who proposes to apply a maximum likelihood method to analyse Faraday rotation correlation in order to derive the primordial magnetic field.

In this work, a statistical analysis of RM distributions is proposed. First, the concept of RM autocorrelation and its relation to magnetic field autocorrelation and power spectrum are derived. This analysis relies on the condition $\nabla \cdot \vec{B} = 0$ and thus, incorporates one important property of magnetic fields directly. Furthermore, a definition of field and RM correlation length is given. This approach has been successfully applied to data and the results are discussed in Chapter 3. In Chapter 5, a Bayesian maximum likelihood approach is suggested in order to determine the power spectrum of the magnetic field fluctuations from observed RM distributions. This method also allows the calculation of error bars.

1.3 The state of the Art - Cluster Magnetic Fields

Clusters of galaxies are the largest gravitationally bound systems and the largest virialised structures in the Universe. At optical wavelengths, clusters appear as overdensities of galaxies with respect to the field average density. Apart from the galaxies, they contain a hot ($T \simeq 10^8$ K) and low density ($n_e \simeq 10^{-3} \text{ cm}^{-3}$) plasma – the intra-cluster medium (ICM). This plasma is observed through its luminous X-ray emission ($L_X \simeq 10^{43} \dots 10^{45} \text{ erg s}^{-1}$) which is produced by thermal bremsstrahlung radiation.

The ICM is magnetised which is directly demonstrated by the observation of large-scale diffuse synchrotron sources as shown in Fig. 1.3. Relativistic electrons of the energy \simeq GeV spiralling around in μG magnetic fields emit synchrotron radiation in the radio wavelength range. For the observation of cluster magnetic fields, this diffuse large-scale synchrotron emission observed as *radio haloes* and *relics* (Sect. 1.3.1) and Faraday rotation measurements of point sources and individual extended radio sources (Sect. 1.3.2) in or behind cluster environments can be used. In the following, a short review is given about our knowledge of the magnetic field strength and structure in the ICM (for detailed reviews see Kronberg 1994; Carilli & Taylor 2002; Widrow 2002).

1.3.1 Radio Haloes and Relics

Willson (1970) observed diffuse radio emission in the centre of the Coma cluster which could not be associated with any cluster source (see Fig. 1.3). A detailed study revealed that the emission is characterised by a steep spectral index. No structure on scales less than $30'$ were detected. Willson (1970) proposed that the diffuse emission is synchrotron radiation. By applying equipartition arguments a field strength of $2 \mu\text{G}$ was deduced. Various sky surveys have increased the number of such large-scale diffuse sources to the present day (e.g. Giovannini et al. 1999; Hunstead & The Sumss Team 1999; Venturi et al. 2000; Kempner & Sarazin 2001). Still the number is quite small (~ 50).

However, a couple of properties have been derived for radio haloes. They are located in the cluster centre and are of roughly spherical shape extending about ~ 1 Mpc. They are characterised by steep spectral indices ($\alpha \geq 1$, if $S_\nu \propto \nu^{-\alpha}$), by a low surface brightness ($\sim 10^{-6} \text{ Jy arcsec}^{-2}$ at 1.4 GHz) and by low polarised flux ($\leq 5\%$). This low degree of polarisation suggests strong depolarisation due to internal Faraday depolarisation since emission region and Faraday screen coincide. Since these sources are very extended, only low resolution observations are possible, therefore also beam depolarisation might play a role when the magnetic fields are disordered on smaller scales than the resolution. The low resolution observations prevent detailed investigations of the magnetic field structure on small scales.

However, minimum/equipartition arguments for the synchrotron emission yield field strength estimates averaged over the radio halo volume (~ 1 Mpc). For this analysis as described in Sect. 1.2.3, usually a low energy cut-off of 10 MHz, a high energy cut-off of 10 GHz are used and a scaling factor between relativistic proton and electron energy density $k = 1$ is assumed. These arguments lead to field strengths of $0.1 \dots 1 \mu\text{G}$ (Feretti 1999).

Another type of diffuse large-scale synchrotron sources are the *radio relics*. In

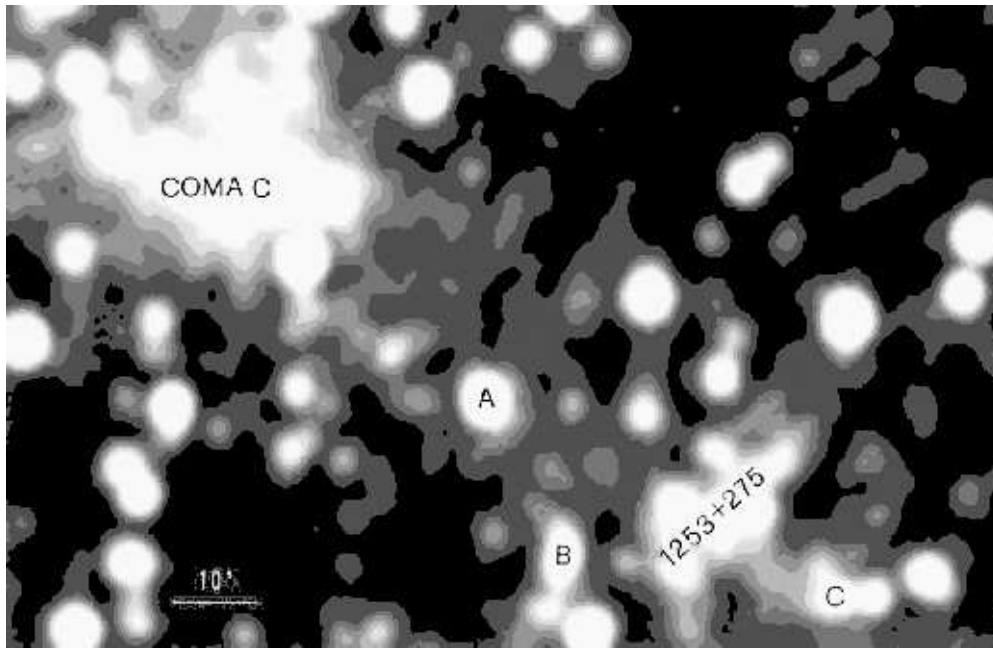


Figure 1.3: A Westerbork Synthesis Radio Telescope map at 327 MHz of the Coma cluster from Giovannini et al. (1991). The central extended radio source C is a so called *radio halo* and a *radio relic* 1253+275 is observed at the periphery. The capital letters indicate extended Coma cluster galaxies, A = NGC 4839, B = NGC 4827, C = NGC 4789. $10'$ correspond to $400 \text{ kpc } h_{50}^{-1}$

contrast to haloes, radio relics are observed at the periphery of clusters and show elongated or irregular shape. They are strongly polarised which can be understood by low internal Faraday depolarisation due to the expected lower magnetic field strength and lower electron densities at the periphery of the clusters.

The prototype for such a relic is the source 1253+275 at the periphery of the Coma cluster (see Fig. 1.3), which was first classified by Ballarati et al. (1981). At 20 cm, its polarisation is 25...30% and the magnetic field is oriented along the source major axis. Minimum energy arguments yield a magnetic field strength $\sim 0.55 \mu\text{G}$ for the synchrotron emitting plasma (Giovannini et al. 1991).

Another example of complex large-scale radio emission in a cluster can be found in Abell 2256 (Bridle & Fomalont 1976; Röttgering et al. 1994). Several head-tail radio galaxies, a central radio halo and two large relic sources are detected in this cluster. The relics are highly polarised, on average 20-30 % but values of up to 50 % are observed (Clarke & Enßlin 2001). The intrinsic magnetic field direction traces the bright filaments in the relics and it appears that there is a large scale order to the fields. Other large relic sources have been detected for instance in Abell 2255 (Burns et al. 1995; Feretti et al. 1997), in Abell 1300 (Reid et al. 1999), in Abell 2744 (Govoni et al. 2001a), in Abell 754 (Kassim et al. 2001) and in Abell 3667 (Röttgering et al. 1997; Johnston-Hollitt et al. 2003). In the latter cluster, there are two almost symmetric relics.

In general, equipartition magnetic fields in relics are determined to be $\sim 0.5 \dots 2 \mu\text{G}$ (Govoni et al. 2001a). However due to the believed origin of the relics, the magnetic fields might be compressed (as discussed below) in these sources and, thus, might not be indicative for the overall magnetic field in the peripheral regions of the cluster.

There is growing evidence that relics are results of ongoing merger events. Enßlin et al. (1998) suggest that relics are caused by first order Fermi acceleration of relativistic particles in shocks produced during cluster merger events. Another scenario suggests that relics are fossil radio sources which were revived by compression associated with mergers (Enßlin & Gopal-Krishna 2001). Both types of relics might exist in reality.

As described in Sect. 1.2.3, apart from equipartition arguments there is also the comparison of synchrotron radio emission with the Inverse Compton X-ray emission. Hard X-ray excess was detected in the spectrum of Coma (e.g. Fusco-Femiano et al. 1999; Rephaeli et al. 1999). A measurement using *BeppoSAX* data detected a non-thermal excess with respect to the thermal radiation of Hard X-ray at a $\sim 4.8\sigma$ level (Fusco-Femiano et al. 2004). Although, this detection is currently under debate (see footnote in Enßlin & Hansen 2004), applying Eq. (1.25), however, yields a volume averaged intra-cluster magnetic field of $\sim 0.2 \mu\text{G}$. The IC and equipartition estimates for the Coma cluster agree very well with each other.

Another example where excess Hard X-ray emission has been detected is in the cluster Abell 2256 (Fusco-Femiano et al. 2000; Rephaeli & Gruber 2003). The analysis of this excess leads to magnetic field strength of $0.05 \mu\text{G}$ in the relic region at the periphery. Higher fields of about $\sim 0.5 \mu\text{G}$ in the region of the halo in the cluster centre could be present.

1.3.2 Rotation Measures

In order to study cluster magnetic fields through RM measurements, polarised radio sources embedded or behind cluster environments have to be observed. In principle, any extragalactic RM consists of different components

$$RM = RM_{intr} + RM_{ICM} + RM_{gal} + RM_{ion,sp}, \quad (1.49)$$

where RM_{intr} is the source intrinsic Faraday rotation, RM_{gal} is the Faraday rotation due to the galactic foreground, $RM_{ion,sp}$ is the Faraday rotation due to the ionosphere of the Earth and RM_{ICM} is the Faraday rotation associated with the cluster gas. The contribution from the Ionosphere of the Earth is in general very small and can be neglected. The galactic component can be subtracted by comparison with RM point source catalogues of pulsars tracing the RM distribution of our Galaxy which is of the order of 10 rad m^{-2} up to 300 rad m^{-2} for sources at low galactic latitudes (e.g. Simard-Normandin et al. 1981; Han et al. 1999).

Once the galactic contribution is subtracted from the RM signal, the contribution from the ICM should dominate the residual RM signal. High resolution RM studies of Cygnus A (Dreher et al. 1987) reveal high RM values with large gradients on arcsec scale which cannot be attributed to a galactic origin or to a thermal gas mixed with the synchrotron emitting plasma. It is concluded that the RM must arise in an external screen of magnetised, ionised plasma. This high resolution studies have been performed on several other extended sources resulting in the same conclusion. Another

strong argument for the dominance of the RM signal from the ICM is the detected asymmetrical depolarisation found in double radio lobes located within galaxy clusters. This asymmetry can be understood as a result from differing Faraday depths of the two lobes – known as the Laing-Garrington effect (Laing 1988; Garrington et al. 1988). In fact, the lobe pointing toward to the observer is less depolarised.

The observing strategy in order to get insight into magnetic field strength and structure is twofold. High resolution RM studies of extended sources located at different cluster impact parameter can be performed by means of determining the mean $\langle RM \rangle$ and the dispersion $\langle RM^2 \rangle$ as described in Sect. 1.2.4. On the other hand, RM samples of point sources located behind or within clusters can be compared to control RM samples of sources whose line of sight does not intersect a cluster.

Concerning the latter method, Lawler & Dennison (1982) were the first to successfully statistically demonstrate Faraday rotation from radio sources observed through cluster atmospheres. They detected a broadening of RM in cluster sources with respect to sources in a control sample. For the Coma cluster, this analysis has been performed by Kim et al. (1990). They evaluated a sample of 18 radio sources and found a significant enhancement of the RM in the inner parts of the cluster. They deduced a magnetic field of $2\mu\text{G}$ assuming a cell size of $\lambda_c = 10 \dots 30$ kpc. Using a sample of 106 radio sources, Kim et al. (1991) deduced a magnetic field strength of about $\sim 1\mu\text{G}$ in the cluster gas.

A more recent study of point sources has been performed by Clarke et al. (2001). The RM 's for a representative sample of 16 cluster radio sources were analysed with respect to a control sample consisting of radio sources being not associated with a cluster atmosphere. The result of this study is shown in Fig. 1.4. A significant broadening of the RM distribution in the cluster sample is detected. Furthermore, an increase in the width of the RM distribution toward smaller impact radii b is observed. Clarke et al. deduce a magnetic field strength of $\sim 4 \dots 8\mu\text{G}$ in the cluster gas assuming a cell size $\lambda_c = 15$ kpc.

Studies of individual, extended RM sources have been first performed on cooling flow clusters since they host powerful radio sources. Extreme values of up to several thousands rad m^{-2} have been detected in these sources (e.g. in Hydra A, see Fig. 1.2). For Hydra A, Taylor & Perley (1993) deduced a magnetic field strength of $5\mu\text{G}$ up to $30\mu\text{G}$ in the innermost regions of this cluster assuming cell sizes $\lambda_c \sim 100 \dots 4$ kpc. Similar high magnetic field strengths were derived for Cygnus A (Dreher et al. 1987), for 3C295 (Perley & Taylor 1991; Allen et al. 2001), for Abell 1795 (Ge & Owen 1993) and the Centaurus cluster (Taylor et al. 2002). For the cooling core cluster 3C129, Taylor et al. (2001) could not detect such high magnetic fields. They derived a field strength of $6\mu\text{G}$ on coherence scales of ~ 5 kpc observed out to ~ 450 kpc.

Extended sources without a cooling core have also been analysed which are not necessarily located in the cluster centre. The analysis of the RM distribution of NGC4869 in the Coma cluster performed by Feretti et al. (1995) resulted in magnetic field strength of $7\mu\text{G}$ tangled on scales of ~ 1 kpc and a weaker field component of $0.2\mu\text{G}$ ordered on a scale of a cluster radius. Extended RM distributions in other non-cooling clusters have also been analysed, i.e. in Abell 119 (Feretti et al. 1999a), in Abell 514 (Govoni et al. 2001b), in Abell 400 and in Abell 2634 (Eilek & Owen 2002). The patchiness of the observed RM distributions indicates magnetic field strengths of $2 \dots 8\mu\text{G}$ on scales $\sim 5 \dots 15$ kpc.

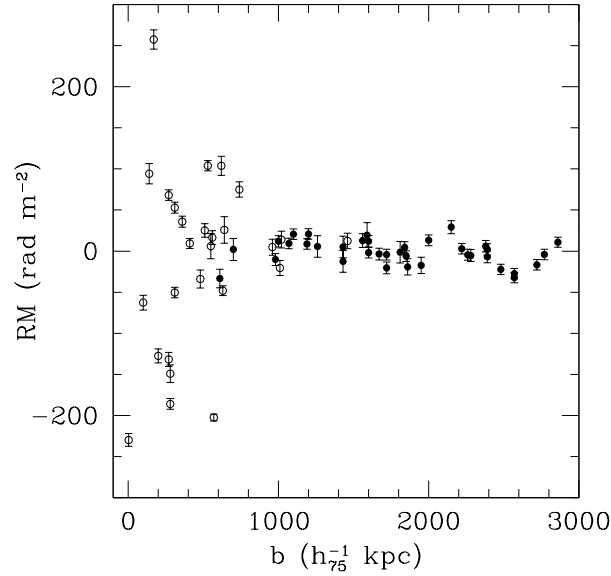


Figure 1.4: RM cluster sample taken from Clarke et al. (2001). For the sample of 16 Abell clusters, galaxy-corrected rotation measure are plotted as a function of source impact parameter b in kiloparsec. The open points represent the *cluster* sources located behind or embedded in the thermal cluster gas while the closed points are the *control* sources at impact parameters beyond the cluster gas. Note the broadening in the width of the RM distribution toward smaller impact parameters.

In general for all these sources, it is observed that the amplitude of the mean $|\langle RM(r) \rangle|$ and the dispersion $\langle RM^2(r) \rangle$ increase with smaller impact radii r . Especially the overall mean $\langle RM \rangle$ is non-zero even if the galactic foreground is subtracted indicating a magnetic field component which is ordered on larger scales than the radio source size. However, the RM distribution in most of the observed extended sources show a Gaussian distribution and appear to be patchy suggesting a field component which is ordered on scales ~ 10 kpc or less.

The magnetic field strengths derived for the cluster gas from RM measurements differ from the field strength derived using the equipartition/minimum energy arguments and the hard X-ray excess emission whereas the results derived from the latter two methods agree generally very well with each other. Synchrotron and IC emission originate from a large cluster volume and magnetic field estimates are averaged over the whole cluster volume. In contrary, RM measurements correspond to line-of-sight integrations and thus, two different sets of measurements will, in general, yield different field values (Goldshmidt & Rephaeli 1993). Furthermore, more realistic electron spectra should be considered in the analysis of synchrotron and IC emission (Enßlin et al. 1999; Petrosian 2001), which would allow for higher field strengths.

Another unrealistic scenario is the assumption of a uniform field throughout the cluster. If the field values detected in the centre of the cluster would extend to several core radii than the magnetic pressure would exceed the thermal pressure in the outer

parts of the cluster, Jaffe (1980) suggested that the magnetic field distribution in a cluster could depend on the thermal gas density

$$B(r) \propto n_e(r)^{\alpha_B}. \quad (1.50)$$

Interesting clues about the magnetic field distribution in clusters can also be gained by magneto-hydrodynamic cosmological simulations (Dolag et al. 1999, 2002). One of their result is that the magnetic field strength at any point within galaxy clusters is proportional to the gas density.

In the case of an only adiabatically compressed field which is frozen-in within the gas, one expects that the exponent $\alpha_B = 2/3$. Crusius-Waetzel et al. (1990) propose that the magnetic to gas pressure ratio is constant throughout the cluster indicating $\alpha_B = 1/2$. Finally, Dolag et al. (2001) find in their analysis an $\alpha_B = 0.9$ for Abell 119. However, there is no known argument which would exclude any value for the exponent α_B in Eq. (1.50).

In conclusion, cluster magnetic fields show a complex structure, i.e. are filamentary and/or have substructure with a range of coherence scales. Hence, the interpretation of RM data by a simple cell model is oversimplified and thus, it is necessary to consider in any analysis more realistic magnetic field distributions which fluctuate over a wide range of spatial scales and whose global distribution might obey Eq. (1.50).

1.4 Some Statistical Tools

Experience tells us that not all the *events that could happen*, or all conceivable *hypotheses* are equally likely. Statistic tries to measure the uncertainty involved.

Given a set of observations, one normally wants to condense and summarise these data sets by fitting a model to them with adjustable parameters. These models can be just straight lines, power laws or something different. Different statistical methods have been developed to fit models to data sets in a proper way (Lupton 1993; Bevington & Robinson 2003).

Ideally, such a method should provide an estimate of the uncertainty of the statistical analysis. In Sect. 1.4.1, the idea of least-squares fitting is presented. Often the power spectra and the autocorrelation function are needed which cannot be measured via a least-squares method. The concept of these two very important functions and their properties will be presented in Sect 1.4.2. A very powerful statistical tool to calculate power spectra is the Bayesian analysis of data in terms of a maximum likelihood approach. In Sect. 1.4.3, the ideas of Bayesian statistics and its applications are described.

1.4.1 Least-Squares & Error Weighting

A widely used method in order to fit models to data sets is least-squares fitting. It is important to note that one of the assumptions of this method is that the data follow a Gaussian probability distribution. An explanation of this is given in Sect. 1.4.3 where the Bayesian approach is discussed.

Suppose n data points (x_i, y_i) to which a model $y(x) = y(x_i, a_1, a_2, \dots, a_m)$ has to be fitted, where the a_1, a_2, \dots, a_m are m model depending parameters. Furthermore, assuming that the standard deviation σ_i of each data point is known and that the

standard deviations are uncorrelated, then the following function has to be minimised in order to find the best fitting model parameter

$$\chi^2 \equiv \sum_{i=1}^n \left(\frac{y_i - y_i(x_i; a_1, a_2, \dots, a_m)}{\sigma_i} \right)^2, \quad (1.51)$$

where the function $y(x) = y_i(x_i; a_1, a_2, \dots, a_m)$ is the expectation or a guess of the function which fits the data. This expression has to be minimised for the parameter a_1, a_2, \dots, a_m .

Assume now the special case of a simple linear model $y(x) = a_1x + a_2$. Particularly important for this work is the χ^2 -least squares fitting of the measured polarisation angle φ_i at different wavelengths λ_i in order to determine RM and the intrinsic polarisation angle φ_0 by fitting Eq. (1.42) to the observed data. Using Eq. (1.51), the function which has to be minimised with respect to the model parameters RM and φ_0 is

$$\chi^2(RM, \varphi_0) = \sum_{i=1}^n \left(\frac{\varphi_i - \varphi_0 - RM\lambda_i^2}{\sigma_i} \right)^2. \quad (1.52)$$

Thus, the following conditions have to be fulfilled.

$$\frac{\partial \chi^2}{\partial RM} = 0 = \overline{\lambda^2 \varphi} - \overline{\lambda^2} \varphi_0 - \overline{\lambda^4} RM \quad (1.53)$$

and

$$\frac{\partial \chi^2}{\partial \varphi_0} = 0 = \overline{\varphi} - \overline{\lambda^2} \varphi_0 - \overline{\lambda^2} RM, \quad (1.54)$$

where the following abbreviations were introduced

$$\overline{S} = \sum_{i=1}^n \frac{1}{\sigma_i^2}, \quad \overline{\lambda^2} = \sum_{i=1}^n \frac{\lambda_i^2}{\sigma_i^2}, \quad \overline{\lambda^4} = \sum_{i=1}^n \frac{\lambda_i^4}{\sigma_i^2}, \quad \overline{\varphi} = \sum_{i=1}^n \frac{\varphi_i}{\sigma_i^2}, \quad \overline{\lambda^2 \varphi} = \sum_{i=1}^n \frac{\lambda_i^2 \varphi_i}{\sigma_i^2},$$

Solving Eq. (1.53) and Eq. (1.54) for RM and φ_0 leads to the following expressions

$$RM = \frac{\overline{S} \overline{\lambda^2 \varphi} - \overline{\lambda^2} \overline{\varphi}}{\overline{S} \overline{\lambda^4} - \overline{\lambda^2}^2} \quad (1.55)$$

and

$$\varphi_0 = \frac{\overline{\varphi} \overline{\lambda^4} - \overline{\lambda^2} \overline{\lambda^2 \varphi}}{\overline{S} \overline{\lambda^4} - \overline{\lambda^2}^2}. \quad (1.56)$$

The standard error for RM and φ_0 can be calculated using the Gaussian propagation of errors which is given by:

$$\sigma_f^2 = \sum_{i=1}^n \sigma_i^2 \left(\frac{\partial f}{\partial y_i} \right)^2, \quad (1.57)$$

where $f = f(y_i)$ and σ_f are the errors. Finally, this leads to the standard errors for RM and φ_0 , respectively,

$$\sigma_{RM}^2 = \frac{\overline{S}}{\overline{S} \overline{\lambda^4} - \overline{\lambda^2}^2} \quad (1.58)$$

and

$$\sigma_{\varphi_0}^2 = \frac{\overline{\lambda^4}}{\overline{S\lambda^4} - \overline{\lambda^2}^2}. \quad (1.59)$$

Another quantity worth to consider is the covariance defined as

$$\text{cov}(y_i, y_j) = \langle (y_i - \langle y_i \rangle)(y_j - \langle y_j \rangle) \rangle = \langle y_i y_j \rangle - \langle y_i \rangle \langle y_j \rangle, \quad (1.60)$$

where the brackets $\langle \rangle$ denote the expectation value. The *variance* is defined as $\text{var}(y_i) = \text{cov}(y_i, y_i)$. The square root of the variance is the standard deviation σ_i in a measurement. However, one can understand the covariance $\text{cov}(y_i, y_j)$ as elements of a *covariance* matrix which describes correlations among the y_i 's. If the y_i and y_j were totally uncorrelated the off-diagonal elements of the covariance matrix would be zero.

Another interesting point related to the interpretation of measurements is the optimal error weighting of any data set. Consider a data set x_i, x_j, \dots, x_n with given standard errors $\sigma_1, \sigma_2, \dots, \sigma_n$. Then any error weighted mean \overline{x} can be expressed as

$$\overline{x} = \frac{\sum_{i=1}^n x_i / \sigma_i^\alpha}{\sum_{i=1}^n 1 / \sigma_i^\alpha}, \quad (1.61)$$

where the exponent α is a parameter for which the above expression has to be optimised. Following Gaussian error propagation, the standard error of the mean would be

$$\sigma_{\overline{x}}^2 = \sum_{i=1}^n \left(\sigma_i \frac{\partial \overline{x}}{\partial x_i} \right)^2. \quad (1.62)$$

The evaluation of the derivation in Eq. (1.62) using Eq. (1.61) leads to

$$\sigma_{\overline{x}}^2 = \frac{\sum_{i=1}^n \sigma_i^{2-2\alpha}}{(\sum_{i=1}^n 1 / \sigma_i^\alpha)^2} \quad (1.63)$$

The best data weighting is achieved when the resulting error is the smallest. Therefore, the minimum with respect to α of Eq.(1.63) is required

$$0 = \frac{\partial \sigma_{\overline{x}}}{\partial \alpha} = \left(\sum_{i=1}^n \ln \sigma_i \sigma_i^{2-2\alpha} \sum_{j=1}^n \sigma_j^{-\alpha} \right) - \left(\sum_{i=1}^n \sigma_i^{2-2\alpha} \sum_{j=1}^n \ln \sigma_j \sigma_j^{-\alpha} \right). \quad (1.64)$$

For this equation to be true the condition $2 - 2\alpha = -\alpha$ has to be fulfilled. Therefore, the optimal error weighting for the calculation of the mean of a data set is achieved for $\alpha = 2$.

1.4.2 Autocorrelation and Power Spectra

As discussed in the previous section, the magnetic field in clusters of galaxies seems to consist of a large-scale component and of a fluctuating component (see Sect. 1.3). This fluctuating component can be statistically described by using the *power spectrum* and the *autocorrelation* function. The concept of these descriptive statistics and their properties is introduced in the following (for a review see Kaiser 2003).

Consider a random scalar function of position in an n -dimensional space $f(\vec{r})$. The following arguments also apply for a vector function or functions of different variables. Furthermore, a *statistically homogeneous process* which specifies the fluctuations of $f(\vec{r})$ is considered. Homogeneity means that the statistical character of the fluctuations does not vary with location. The statistical description of such a random function is provided by the N -point distribution functions. The 1-point distribution function

$$p(f)df \quad (1.65)$$

gives the probability to observe a field value f at some randomly chosen location in space. The 2-point distribution function

$$p(f_1, f_2)df_1df_2 \quad (1.66)$$

describes the probability to observe $f(\vec{r}_1) = f_1$ and $f(\vec{r}_2) = f_2$ at two positions \vec{r}_1 and \vec{r}_2 . For a statistically homogeneous process, the 2-point distribution function only depends on the separation $\vec{r}_1 - \vec{r}_2$ and for a statistically isotropic process, it only depends on the modulus of the separation $|\vec{r}_1 - \vec{r}_2|$. Higher order distribution functions can easily be derived following the scheme above.

The integration of the distribution functions results in *correlation functions*. The most important one is the *2-point correlation function* or *autocorrelation function*

$$\xi(\vec{r}_{12}) = \langle f_1 f_2 \rangle = \int df_1 \int df_2 f_1 f_2 p(f_1, f_2), \quad (1.67)$$

where $\vec{r}_{12} = \vec{r}_1 - \vec{r}_2$. This function again only depends on the separation given the assumption of statistical homogeneity. The N -point correlation functions are *moments* of the corresponding distribution functions. However, the autocorrelation function is extremely useful since it allows to calculate the *variance* $\langle f^2 \rangle = \xi(0)$ of any *linear* function of the random field.

The autocorrelation function $\xi(r)$ is a real space statistic. Since the statistically homogeneous fields imply translational invariance, Fourier space statistic may also be useful

$$\tilde{f}(\vec{k}) = \int d^n r f(\vec{r}) e^{i\vec{k} \cdot \vec{r}}. \quad (1.68)$$

The *power spectrum* per volume $P(\vec{k})$ is defined as $P(\vec{k}) = (1/V) \langle \tilde{f}(\vec{k}) \tilde{f}^*(\vec{k}) \rangle$, where \tilde{f}^* is the complex conjugate of \tilde{f} . Consider the average of the following expression:

$$P(\vec{k}, \vec{k}') = \frac{1}{V} \langle \tilde{f}(\vec{k}) \tilde{f}^*(\vec{k}') \rangle = \frac{1}{V} \int d^n r \int d^n r' \langle f(\vec{r}) f(\vec{r}') \rangle e^{i\vec{k} \cdot \vec{r}} e^{-i\vec{k}' \cdot \vec{r}'}. \quad (1.69)$$

Under the condition of statistical homogeneity $\langle f(\vec{r}) f(\vec{r}') \rangle = \xi(\vec{r} - \vec{r}')$ and changing the second integration variable \vec{r}' to $\vec{z} = \vec{r} - \vec{r}'$ yields

$$P(\vec{k}, \vec{k}') = \frac{1}{V} \langle \tilde{f}(\vec{k}) \tilde{f}^*(\vec{k}') \rangle = \frac{1}{V} \int d^n r e^{i(\vec{k} - \vec{k}') \cdot \vec{r}} \int d^n z \xi(\vec{z}) e^{i\vec{z} \cdot \vec{k}} \quad (1.70)$$

and, finally

$$\langle \tilde{f}(\vec{k}) \tilde{f}^*(\vec{k}') \rangle = (2\pi)^n \delta^n(\vec{k} - \vec{k}') \hat{\xi}(\vec{k}), \quad (1.71)$$

where $\delta(\vec{k} - \vec{k}')$ denotes the Dirac δ -function and the Fourier transformed autocorrelation function is

$$\hat{\xi}(\vec{k}) = \int d^n r \xi(\vec{r}) e^{i\vec{k}\cdot\vec{r}}. \quad (1.72)$$

Equation (1.71) implies that the different Fourier modes (i.e. $\vec{k}' \neq \vec{k}$) are completely uncorrelated. This is a direct consequence of the assumed translational invariance, or the statistical homogeneity, of the field. In real space however, $f(\vec{r})$ will generally have extended correlations, i.e. $\langle f(\vec{r})f(\vec{r}') \rangle \neq 0$ for $\vec{r} \neq \vec{r}'$.

Some properties of the power spectrum worth noting are:

- The *Wiener-Khinchin* theorem states that the power spectrum per volume and the autocorrelation function are related by a Fourier transform: $P(\vec{k}) = V\hat{\xi}(\vec{k})$.
- Using the power spectrum, the variance of the field can be determined by taking the inverse transform of Eq. (1.72) at $\vec{r} = 0$ which gives

$$\langle f^2 \rangle = \xi(0) = \int \frac{d^n k}{(2\pi)^3} \hat{\xi}(\vec{k}) = \frac{1}{(2\pi)^n V} \int d^n k P(\vec{k}), \quad (1.73)$$

thus, by integration of the power spectrum, the total variance of the field can be derived.

- If the field can be considered to be statistically isotropic then the power spectrum only depends on the modulus of the wave vector: $P(\vec{k}) = P(k)$.
- If the field $f(\vec{r})$ is incoherent, i.e. $\xi(\vec{r}) \propto \delta(\vec{r})$, then the power spectrum is constant. Such fields are referred to as 'white noise'.

In real situation, one is faced with the problem of estimating the power spectrum from a finite sample of the infinite random field (e.g. the *RM* distributions which are limited by the finite radio source size even though the magnetised cluster gas extends beyond that). One can write such samples as $f_s(\vec{r}) = W(\vec{r})f(\vec{r})$, where the function $W(\vec{r})$ describes the sample geometry and is often referred to as the 'window function'.

The Fourier transform of such a finite sample of the field is the convolution of the transforms \hat{f} and \hat{W} , following the convolution theorem:

$$\hat{f}_s(\vec{k}) = \int \frac{d^n k'}{(2\pi)^n} \hat{f}(\vec{k}') \hat{W}(\vec{k} - \vec{k}'). \quad (1.74)$$

This means that the transform of the sample is a somewhat smoothed version of the intrinsically incoherent $\hat{f}(\vec{k})$. The width of the smoothing function \hat{W} is $\Delta k \sim 1/L$, where L is the size of the sampling volume. Hence, the transform \hat{f}_s will be coherent over scales $\delta k \ll L$ but will be incoherent on larger scales. Thus, the act of sampling introduces finite range correlations in the Fourier transform of the field.

1.4.3 Bayesian Statistics

A method in order to quantify uncertainties in a measurement are given by Bayesian ideas (for a review, see D'Agostini 2003). The two crucial aspects of these ideas are

- Probability is understood as the degree of belief that an event will occur.

- Probability depends on our state of knowledge, which is different for different people. Therefore probability is necessarily subjective.

Consider two *events* A and B where $P(A)$ and $P(B)$ are the probabilities of the event A or B , respectively. It is clear that for the probability $P(A)$ the following holds $0 \leq P(A) \leq 1$. Furthermore, for two events A and B

$$P(A \cup B) = P(A) + P(B) - P(A \cap B) \quad (1.75)$$

$$P(A \cap B) = P(B|A)P(A) = P(A|B)P(B), \quad (1.76)$$

where \cup denotes the logical OR and \cap denotes the logical AND. The probability $P(A \cup B)$ is the *logical sum* and $P(A \cap B)$ is the *logical product* of two probabilities $P(A)$ and $P(B)$. The latter is also often called the joint probability. The term $P(A|B)$ describes the probability of A under the condition that B is true and is shortened by saying probability of A given B .

Another important property is the *probabilistic independence* of events. If the probability of A does not change the status of B , the events A and B are said to be independent. In that case $P(A|B) = P(A)$, and $P(B|A) = P(B)$. Inserting this into Eq. (1.76) yields

$$P(A \cap B) = P(A)P(B). \quad (1.77)$$

From Eq. (1.76), Bayes Theorem is easily derived:

$$P(B|A) = \frac{P(A|B)P(B)}{P(A)}, \quad (1.78)$$

where $P(B)$ is called the *prior* probability, $P(B|A)$ is called the *posterior* probability and $P(A|B)$ is the *likelihood*. If one identifies event A with an observation and event B with some set of model parameters, the likelihood can be literally described as the probability of the observation A given the specific hypotheses B . In the same context, the probability of the observation $P(A)$ is a constant although it is unknown leaving the proportionality

$$P(B|A) \propto P(A|B)P(B), \quad (1.79)$$

the prior probability $P(B)$ is a statement about our knowledge of the hypotheses and is mostly assumed to be uniform when one does not know anything about the probability of the hypotheses. However, Bayes postulates that all priors should be treated as equal.

So far, it was implicitly assumed that the variable x is discrete and a probability function $p(x)$ is interpreted as the probability of the proposition $P(A)$, where A is true when the value of the variable is equal to x . However in most cases, continuous variables x have to be considered and the probability will be a continuous function interpreted as a probability density function $p(x)dx$. In terms of the probability $P(A)$, it is understood as A is true when the value of the variable lies in the range $x + dx$. In the further discussion, the latter perspective is assumed.

Assuming a set of data being the observations \mathbf{d} and a set of models $\boldsymbol{\theta}$ describing our expectations, then Eq. (1.79) becomes

$$p(\boldsymbol{\theta}|\mathbf{d}) \propto p(\mathbf{d}|\boldsymbol{\theta})p(\boldsymbol{\theta}). \quad (1.80)$$

If the data d_i are independent, then the likelihood $\mathcal{L}(\boldsymbol{\theta}; \mathbf{d}) = p(\mathbf{d}|\boldsymbol{\theta})$ can be expressed as

$$\mathcal{L}(\boldsymbol{\theta}; \mathbf{d}) = p(\mathbf{d}|\boldsymbol{\theta}) = \prod_i \mathcal{L}(\boldsymbol{\theta}; d_i). \quad (1.81)$$

As mentioned, if one knows so little about the appropriate values of the hypotheses parameter that for the prior $p(\boldsymbol{\theta})$ a uniform distribution is a practical choice and using the independence described by Eq. (1.81), Eq. (1.80) becomes

$$p(\boldsymbol{\theta}|\mathbf{d}) \propto p(\mathbf{d}|\boldsymbol{\theta}) = \prod_i \mathcal{L}(\boldsymbol{\theta}; d_i). \quad (1.82)$$

Therefore, the maximum of the posterior probability $p(\boldsymbol{\theta}|\mathbf{d})$, which is the interesting probability of the model given the data, can be found by maximising the likelihood $\mathcal{L}(\boldsymbol{\theta}; \mathbf{d})$ – maximising the probability of the data given the model. This consideration leads to the *maximum likelihood principle*.

In order to derive a least-squares formulae (Eq. 1.51) as presented in Sect. 1.4.1, one considers the likelihood to be described by a Gaussian distribution. Assuming that the data are independent consisting of pairs $\{x_i, y_i\}$, whose true value $\{\mu_{x_i}, \mu_{y_i}\}$ are related by a deterministic function $\mu_{y_i} = y(\mu_{x_i}, \boldsymbol{\theta})$ and with Gaussian errors σ_i only in y_i (i.e. $x_i \approx \mu_{x_i}$) then the likelihood function is a multivariate Gaussian

$$p(\boldsymbol{\theta}|\mathbf{x}, \mathbf{y}) = \mathcal{L}(\boldsymbol{\theta}; \mathbf{x}, \mathbf{y}) \propto \prod_i \exp \left[-\frac{(y_i - y(x_i, \boldsymbol{\theta}))^2}{2\sigma_i^2} \right] \quad (1.83)$$

$$= \exp \left[-\frac{1}{2} \chi^2(\boldsymbol{\theta}) \right], \quad (1.84)$$

where

$$\chi^2(\boldsymbol{\theta}) = \sum_i \frac{(y_i - y(x_i, \boldsymbol{\theta}))^2}{\sigma_i^2}, \quad (1.85)$$

which is the same as Eq. (1.51). Maximising the likelihood function is equivalent to minimising $\chi^2(\boldsymbol{\theta})$ with respect to $\boldsymbol{\theta}$. The interesting point is that this equation holds for independent variables and Gaussian distributions. One should keep these assumptions in mind when applying this method to data sets.

The uncertainty in $\boldsymbol{\theta}$ is determined by considering the covariance matrix \mathbf{V}

$$(V^{-1})_{ij}(\boldsymbol{\theta}) = \frac{1}{2} \frac{\partial^2 \chi^2}{\partial \theta_i \partial \theta_j} \Big|_{\boldsymbol{\theta}=\boldsymbol{\theta}_m}, \quad (1.86)$$

where $\boldsymbol{\theta}_m$ is the set of parameters which minimise the χ^2 -function. This is a consequence of the assumed multi-variate Gaussian distribution of $\boldsymbol{\theta}$. Expanding χ^2 in series around its minimum $\chi^2(\boldsymbol{\theta}_m)$

$$\chi^2(\boldsymbol{\theta}) \approx \chi^2(\boldsymbol{\theta}_m) + \frac{1}{2} \boldsymbol{\Delta\theta}^T \frac{\partial^2 \chi^2}{\partial \theta_i \partial \theta_j} \boldsymbol{\Delta\theta}, \quad (1.87)$$

where $\boldsymbol{\Delta\theta}$ is the difference $\boldsymbol{\theta} - \boldsymbol{\theta}_m$. Using Eq. (1.86), and inserting Eq. (1.87) into Eq. (1.83) and applying an appropriate normalisation results in the Likelihood function

$$\mathcal{L}(\boldsymbol{\theta}; \mathbf{x}, \mathbf{y}) \approx \frac{1}{(2\pi)^{n/2} (\det \mathbf{V})^{1/2}} \exp \left[-\frac{1}{2} \boldsymbol{\Delta\theta}^T \mathbf{V}^{-1} \boldsymbol{\Delta\theta} \right], \quad (1.88)$$

where n is the dimension of $\boldsymbol{\theta}$ and $\det \mathbf{V}$ indicates the determinant. It is noteworthy that Eq. (1.88) is exact when $y(\mu_{x_i}, \boldsymbol{\theta})$ depends linearly on the various θ_i .

The likelihood function can also be used as a power spectrum estimator since such an estimator has to minimise the variance. If one identifies the covariance matrix as defined by Eq. (1.60) and assuming the mean to be zero $\langle y_i \rangle = 0$, the likelihood function changes

$$\mathcal{L}(\boldsymbol{\theta}; \mathbf{x}) = \frac{1}{(2\pi)^{N/2}(\det \mathbf{C})^{1/2}} \exp \left[-\frac{1}{2} \boldsymbol{\Delta}^T \mathbf{C}^{-1} \boldsymbol{\Delta} \right], \quad (1.89)$$

where C is the covariance matrix, which expresses the theoretical expectations and depends on the model parameters, Δ_i are the data and N is the dimension of the covariance matrix.

1.4.4 Structure of the Thesis

The interpretation of the Faraday rotation data as being associated with an external Faraday screen has been challenged several times and is subject to a broad discussion. Therefore, Chapter 2 is devoted to this question. After being confident of the interpretation as Faraday rotation being external to the source, Chapter 3 describes the application of autocorrelation and power spectrum analysis to the Faraday rotation data. However, it was realised that the map making algorithm might produce artefacts related to the mentioned $n\pi$ -ambiguity influencing this analysis significantly. Therefore, in Chapter 4 a new *RM* map-making algorithm called *Pacman* is introduced and compared to the standard algorithms. Finally, motivated by the recent and great success of maximum likelihood methods in the determination of power spectra, this method is applied to Faraday rotation data in Chapter 5.

Chapter 2

Is the Faraday Rotation Source-Intrinsic or not?

For clusters of galaxies, the interpretation of Faraday rotation data relies on the assumption that the Faraday rotation medium and the source of the linearly polarised emission are well separated. This assumption has been challenged by Bicknell et al. (1990) and more recently by Rudnick & Blundell (2003). This chapter is aimed to give evidence in favour for the validity of the assumption of an external Faraday screen which is presumed in the following chapters. This work is published in Enßlin et al. (2003). My part in this work was the application of the statistics to several observational and generated data sets.

2.1 A Long Lasting Debate

As already mentioned in Sect. 1.2.4, it is difficult to distinguish between source intrinsic and source external Faraday depolarisation. Most authors argue in favour for the Faraday screen being external to an extragalactic extended radio source and identify the Faraday screen with the surrounding intra-cluster medium. Another scenario has also been widely discussed. In this scenario, the dominating Faraday rotating region is located in a dense, thin mixing layer around the radio source. The consequence of this scenario is that the estimated field strengths for the intra-cluster medium would be lower by at least one order of magnitude.

Bicknell et al. (1990) argue in favour of the latter scenario. They performed a three-dimensional smoothed particle hydrodynamical simulation of a transonic shear layer so that large-scale nonlinear surface waves can form on the lobes of extragalactic radio sources through the successive merging of smaller waves generated by the Kelvin-Helmholtz instability. They propose a theory which relates the surface waves developing to substantial variations in rotation measures. They argue, that such a model being a surface effect would also give rise to a dependence of the polarisation angle φ on the wavelength squared as observed.

Recently, Rudnick & Blundell (2003) proposed a different method in order to find arguments for the scenario of the Faraday rotating region being a thin dense layer around the radio source. They compare the intrinsic polarisation angle φ_0 with the RM at each point of the source PKS 1246-410 in the Centaurus cluster observed by

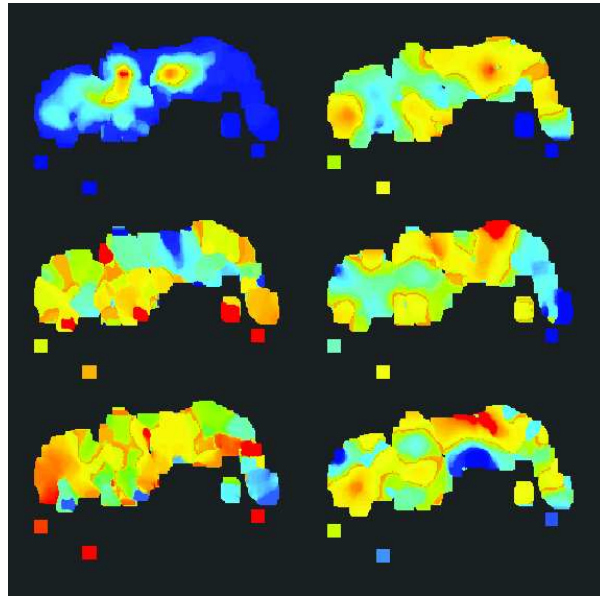


Figure 2.1: This plot is adapted from Rudnick & Blundell (2003) and shows polarisation structures of the source PKS 1246-410. The source is $\approx 30''$ long. Left column: Original data from Taylor et al. (2002) after applying a median weight filter. Top: polarised intensity at 8 GHz, peak flux density 4 mJy/beam (red); middle rotation measures ≈ -1300 (blue) to 1300 (red) rad/m^2 ; bottom: intrinsic polarisation angle $\varphi_0 - 90^\circ$ (blue) to 90° (red). Right Column: three different simulations of rotation measures having the same colour coding as the actual rotation measures have. Note the different patchiness of the simulated rotation measure images compared to the original data although they share the same RM power spectrum.

Taylor et al. (2002), which is shown in the middle left panel of Fig. 2.1 after applying a smoothing algorithm. If the RM is generated in a thin dense mixing layer enclosing the radio source, co-spatial structures in the φ_0 and RM distributions are expected. On the other hand, if the Faraday rotation is generated in an external intra-cluster medium then there should be no correlation observed between RM and φ_0 .

Rudnick & Blundell (2003) search for co-spatial structures in the distribution of RM and φ_0 . For that, they derive RM - φ_0 scatter plots in which they compare these two quantities at each point of the image. For the source PKS 1246-410, this scatter plot is shown in the upper middle panel of Fig. 2.2. Rudnick & Blundell argue that local co-alignment of φ_0 and RM should lead to strongly clustered point distributions in such a scatter plot. Since also statistically independent RM and φ_0 distributions may produce such clustering Rudnick & Blundell generate synthetic RM maps having the same power spectrum as the observed one, but random phases. They repeat their analysis with these simulated images and find that the scatter plots for the simulated maps show less clustering. They conclude that the scenario of a mixing layer is the most likely one.

2.2 The Argument Reconsidered

The conclusion of Rudnick & Blundell (2003) is statistically questionable since the human eye will detect in any data set apparent correlations. Furthermore, φ_0 and RM carry correlated noise as noted by Rudnick & Blundell since these two quantities are generated from the same set of polarisation angle distributions. In the worst case, this correlation will produce step-function like artefacts in the distributions at the same location. These artefacts are present in the original data.

The analysis performed by Rudnick & Blundell is designed to have the same RM power spectrum as the observation but higher order correlations are neglected by the random phase realisation. Unfortunately, the statistic used by Rudnick & Blundell is very sensitive to higher order correlations. Any clustering in the RM - φ_0 scatter plot is a result of patches of nearly constant values in the RM and φ_0 images. A special relation in the Fourier phases (or in higher order correlations) is required in order to recover the appearance of patches in the RM and φ_0 distributions.

The strength of the clustering in the scatter plot is indeed strongest if the φ_0 and RM features are correlated. However, the clustering does not disappear if the RM and φ_0 patches have independent distributions, since every φ_0 patch is still overlaid by a small number of RM patches, so that the associated clustering in the scatter plot only gets split into a corresponding number of smaller clusters. These clusters happen to be co-aligned on a vertical constant φ_0 line in the plot, since they all belong to the same φ_0 coherence patch. A corresponding mechanism splits the pixels of an RM cell into a horizontal constant RM line. Such vertical and horizontal features can be indeed seen in the scatter plot of PKS 1246-410 (upper middle panel of Fig. 2.2).

In order to perform an experiment which maintains also higher order statistics, one can simply exchange subregions of the RM image from one lobe to the other. This should keep the same RM correlation functions but it will destroy any real correlation between φ_0 and RM , since the different regions of the source are independent. This simple experiment was done by diving the source in roughly two equal regions about the centre and shifting the coordinates in right ascension such that two subregions overlap. The φ_0 distribution of the east (west) lobe is plotted against the RM data of the west (east) lobe. The shifting of lobes is preferable to a reflection about the centre eliminating possible radial influences on any correlation. The result of this experiment is shown in the upper right panel of Fig. 2.2. The clustering of points does not vanish even though the distributions should be independent.

By going a step further, one can generate patchy RM and φ_0 maps consisting of patches with nearly constant values but which are statistically independent from each other. For both maps similar recipes were used. First a number N of random seed points \vec{X}_i ($i \in \{1 \dots N\}$) within a square area is drawn, and then the area is split into cells around the seed points by means of a Voronoi-tessellation: Each point \vec{x} of the area belongs to the cell of its nearest seed \vec{X}_i . Then each seed is attributed a random value ψ_i (ψ stands in the following for both RM and φ_0) and a small two-dimensional random vector $\vec{\nabla}\psi_i$ (= auxiliary RM or φ_0 gradients within the patches, only used for the map construction). Each pixel \vec{x} within the cell of seed i gets a value

$$\psi(\vec{x}) = \psi_i + \vec{\nabla}\psi_i \cdot (\vec{x} - \vec{X}_i) + \sigma(\vec{x}), \quad (2.1)$$

where $\sigma(\vec{x})$ is a small random noise term. The resulting map consists of patches with

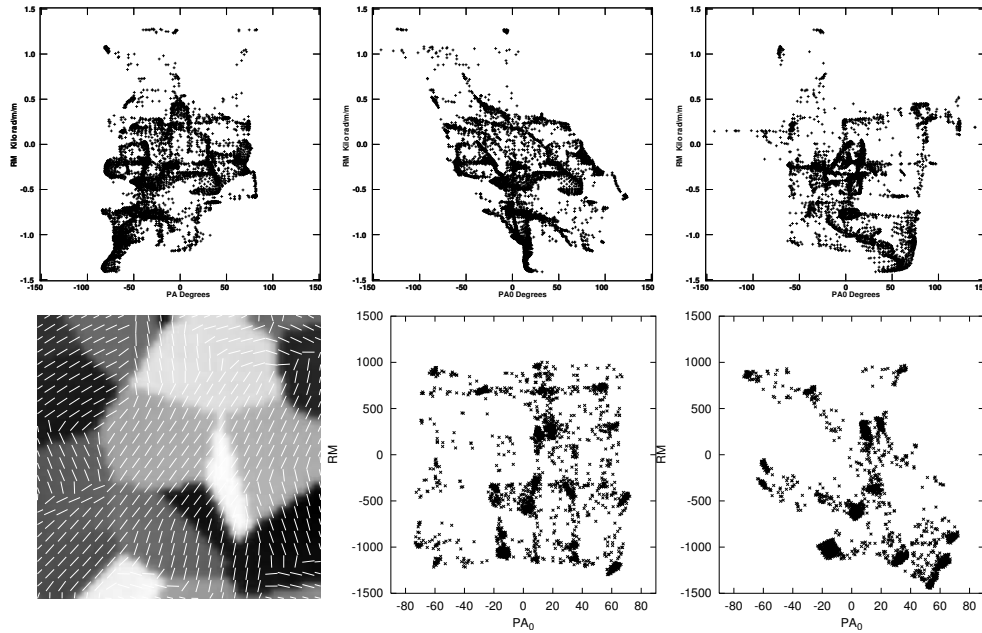


Figure 2.2: This plot is adapted from Enßlin et al. (2003). Upper left panel: Uncorrected φ - RM scatter plot of PKS 1246-410. The underlying maps were smoothed by a median weight filter. Upper middle panel: φ_0 - RM scatter plot of PKS 1246-410. Upper right panel: φ_0 - RM scatter plot of PKS 1246-410, but with the RM maps of the Eastern and Western radio lobe exchanged as an independent experiment. Lower left panel: Simulated φ_0 (white lines) and RM (grey scale) maps with independent coherence patches. Lower middle panel: φ_0 - RM scatter plot of the simulated independent φ_0 and RM maps shown on the left. Lower right panel: φ_0 - RM scatter plot of simulated maps with co-aligned φ_0 and RM coherence patches.

nearly constant values, but which exhibit some internal trends and noise.

The φ_0 and RM maps were slightly smoothed, a 20% border region was cut away in order to suppress edge effects, and a φ_0 - RM scatter plot is generated. A typical realisation of such a map and its scatter plot is shown in the lower left and lower middle panel of Fig. 2.2, respectively. A strongly clustered distribution is visible even though the individual φ_0 and RM maps were completely independent. Furthermore, nearly horizontal and vertical chains of clusters are visible for the reasons given above. The map smoothing produces bridges between these clusters, since it gives intermediate values to pixels which are at the boundaries of φ_0 and RM cells.

The deviations from the strict horizontal and vertical directions visible in the scatter plot of PKS 1246-410 should be caused by trends within the coherence cells. Note that such structures are also visible in the simulated scatter plots of Rudnick & Blundell, although the smooth realisations of their RM maps have smeared them out (see their Fig. 2 for a comparison of the patchiness of observed and simulated RM maps).

Therefore, one can conclude that the data of PKS 1246-410 favours statistically independent φ_0 and RM maps. The occurrence of vertical and horizontal lines in the scatter plot of the observational data demonstrates that the φ_0 and RM patches are

indeed misaligned.

In order to further investigate this, a model is constructed in which the φ_0 and RM patch positions are absolutely identical. This is constructed by moving the Voronoi-tessellation seed points of the RM map to the locations of nearby seed points of the φ_0 map, thereby assuring that there is a one-to-one mapping. All other variables (RM_i , φ_{0i} etc) were kept as before. The recomputed RM map has therefore exactly the same patch locations as the φ_0 map. The horizontal and vertical cluster alignments and stripes are absent there (see the lower right panel of Fig. 2.2). There are now several stripes with diagonal orientations due to pixels at the φ_0 - RM cell boundaries which received simultaneously intermediate values in φ_0 and RM by the smoothing.

2.3 Statistics Comes to Aid

The comparison of absolute values such as RM and φ_0 as suggested by Rudnick & Blundell does not seem to be a reliable statistical test. It relies on the one hand on the human eyes and thus, it is extremely subjective. On the other hand, the more pixels have a value in the RM and φ_0 maps the more the RM - φ_0 scatter plot will be covered by points and eventually no conclusion can be drawn anymore.

It is preferable to chose a statistic which fulfils the following requirements:

1. The statistic should be sensitive to the presence of correlated spatial changes of φ_0 and RM , independent of the local values of these quantities.
2. The statistic should not require a comparison between simulated and observed data, since it is problematic to reproduce the same statistical properties of the observed data set.
3. The statistic should provide unique expectation values, i.e. being equal to zero for the uncorrelated case and being unity for fully correlated maps.
4. The statistic should be analytic and sufficiently simple, allowing the derivation of basic properties and its analytical understanding.
5. The significance of the statistic should increase monotonically with the map size.

For the construction of such a statistic, a *gradient alignment statistic* A of different maps can be introduced. This statistic compares the gradients $\vec{p} = \vec{\nabla} RM$ and $\vec{q} = \vec{\nabla} \varphi_0$ and checks for alignment of these gradients indicating correlated changes in φ_0 and RM . The absolute values are of no significance for the question of co-alignment and thus, the comparison of the gradients should give the same signal for parallel and anti-parallel gradients. Hence, instead of the scalar product

$$\vec{p} \cdot \vec{q} = p q (\cos \phi_p \cos \phi_q + \sin \phi_p \sin \phi_q) = p_x q_x + p_y q_y, \quad (2.2)$$

where $\vec{p} = (p_x, p_y) = p (\cos \phi_p, \sin \phi_p)$ and $\vec{q} = (q_x, q_y) = q (\cos \phi_q, \sin \phi_q)$, an *alignment product* can be constructed

$$\begin{aligned} \langle \vec{p}, \vec{q} \rangle &= p q (\cos 2\phi_p \cos 2\phi_q + \sin 2\phi_p \sin 2\phi_q) \\ &= \frac{(p_x^2 - p_y^2)(q_x^2 - q_y^2) + 4 p_x p_y q_x q_y}{\sqrt{p_x^2 + p_y^2} \sqrt{q_x^2 + q_y^2}}. \end{aligned} \quad (2.3)$$

This alignment product has the following properties

$$\langle \vec{p}, \alpha \vec{p} \rangle = |\alpha| p^2, \quad (2.4)$$

$$\langle \vec{p}, \vec{q} \rangle = -pq, \quad \text{if } \vec{p} \perp \vec{q} \quad (2.5)$$

where α is a real (positive or negative) number. An isotropic average of the alignment product of two 2-dimensional vectors leads to a zero signal, since the positive (aligned) and negative (orthogonal) contributions cancel each other out.

Then the alignment statistics of the vector fields $\vec{p}(\vec{x}) = \vec{\nabla} RM(\vec{x})$ and $\vec{q} = \vec{\nabla} \varphi_0(\vec{x})$ can be defined as

$$A = A[\vec{p}, \vec{q}] = \frac{\int d^2x \langle \vec{p}(\vec{x}), \vec{q}(\vec{x}) \rangle}{\int d^2x |\vec{p}(\vec{x})| |\vec{q}(\vec{x})|}, \quad (2.6)$$

which fulfils the required properties mentioned above:

No. 1: The statistic does not depend on any global relation between φ_0 and RM . This can be demonstrated by changing a potential functional dependence using non-linear data transformations. Any non-pathological¹, piecewise continuous and piecewise monotonic pair of transformations $RM^* = S(RM)$ and $\varphi_0^* = T(\varphi_0)$ do not destroy the alignment signal due to the identity

$$\langle \vec{\nabla} RM^*, \vec{\nabla} \varphi_0^* \rangle = |S'(RM) T'(\varphi_0)| \langle \vec{\nabla} RM, \vec{\nabla} \varphi_0 \rangle. \quad (2.7)$$

Inserted into Eq. (2.6), one finds that the weights of the different contributions to the alignment signal might be changed by the transformation, but except for pathological cases any existing alignment signal survives the transformation and no spurious signal is produced in the case of uncorrelated maps.

No. 2 & 3: A simple calculation shows that the expectation value for A is zero for independent maps and it is unity for aligned maps. For illustration, the simulated pair of independent maps has $A = -0.03$, which can be regarded as a test of the statistic with a case where the statistic of Rudnick & Blundell incorrectly detects co-alignment. The simulated pair of co-aligned maps has $A = 0.89$ illustrating A 's ability to detect correlations. Property No. 3 implies requirement No. 2.

No. 4: From the discussion so far, it should be obvious that many essential properties of the alignment statistics can be derived analytically. However, as an additional useful example the effect of a small amount of noise present in both maps can be estimated. Each noise component is assumed to be uncorrelated with RM , to φ_0 , and also to the other noise component. For small noise levels, it can be found that

$$A[\vec{p} + \delta\vec{p}, \vec{q} + \delta\vec{q}] \approx \frac{A[\vec{p}, \vec{q}]}{(1 + \overline{\delta p^2/p^2})(1 + \overline{\delta q^2/q^2})}, \quad (2.8)$$

where the bar denotes the statistical average. This relation holds only approximately, since the non-linearity of A prevents exact estimates without specifying the full probability distribution of the fluctuations. As can be seen from Eq. (2.8), uncorrelated noise reduces the alignment signal, but does not produce a spurious alignment signal, in contrast to correlated noise, which usually does.

¹A pathological transformation would e.g. split the RM or φ_0 value range into tiny intervals, and randomly exchange them or map them all onto the same interval.

No. 5: If the RM and φ_0 maps are enlarged by an additional region with the same statistical properties the expectation value of A is unchanged, due to the averaging property of Eq. (2.6), and fluctuations in A decrease due to the central limit theorem.

Practically, gradients of a quantity ψ defined on RM and φ_0 maps by assigning the pixel position (i, j) were calculated by $\vec{\nabla}\psi = (\psi_{i+1,j} + \psi_{i+1,j+1} - \psi_{i,j} - \psi_{i,j+1}, \psi_{i,j+1} + \psi_{i+1,j+1} - \psi_{i,j} - \psi_{i+1,j})$, where $\psi_{i,j}$ denotes the value of ψ at the pixel position (i, j) . Neither the small diagonal shift by $1/2$ pixel in i and j directions, nor the missing normalisation of the so defined gradient have any effect on the statistic. φ_0 -gradients are calculated using subtraction modulo 180° in order to account for the cyclic nature of φ 's. This scheme was directly applied to the maps, even though for the synthetic maps gradient-like auxiliary quantities were defined and used during their construction.

However, before the gradient alignment statistic can be applied to real datasets, it has to be noted that it is very sensitive to correlations on small scales, since it is a gradient square statistic. Observed RM and φ_0 maps will always have some correlated fluctuations on small scales, since they are both derived from the same set of radio maps, so that any imperfection in the map making process leads to correlated fluctuations in both maps. Therefore, the strength of signal contamination by such correlated errors has to be estimated, and – if possible – minimised before any reliable statement about possible intrinsic correlations of φ_0 and RM can be made. This point can not be overemphasised! Therefore, the next Sect. 2.4 is devoted to the estimation of the level of expected correlated noise.

Fortunately, the noise correlation is of known functional shape, which is a linear anti-correlation of the φ_0 and RM errors. This allows to detect this noise via a *gradient vector-product statistic* V defined as

$$V = V[\vec{p}, \vec{q}] = \frac{\int d^2x \vec{p}(\vec{x}) \cdot \vec{q}(\vec{x})}{\int d^2x |\vec{p}(\vec{x})| |\vec{q}(\vec{x})|}. \quad (2.9)$$

This statistic is insensitive to any existing astrophysical φ_0 - RM correlation, since the latter should produce parallel and anti-parallel pairs of gradient vectors with equal frequency, thereby leading to $V = 0$. A map pair without any astrophysical signal, which was constructed from a set of independent random φ maps, will give $V = r \gtrsim -1$, where $-1 \leq r \leq 0$ is the correlation coefficient of the noise calculated in the following Sect. 2.4. The statistic V as a test for correlated noise fulfils therefore requirements similar to the ones formulated for A , with the only difference that a requirement like No. 1 is not necessary, since the functional shape of noise correlations is known.

It can be expected that correlated noise leads to a spurious φ_0 - RM co-alignment signal of the order $A \approx |V|$, since for perfectly anti-parallel gradients these quantities are identical. Therefore, it can be proposed to use the quantity $A + V$ as a suitable statistic to search for a source intrinsic φ_0 - RM correlation: The spurious signal in A caused by the map making process should be roughly compensated by the negative value of V , whereas any astrophysical co-alignment φ_0 - RM signal only affects A , and not V , since there should be no preference between parallel and anti-parallel RM and φ_0 gradients, leading to cancellation in the scalar-product average of V .

The statistic developed was applied to the RM and φ_0 maps of PKS 1246-410 from Taylor et al. (2002), Cygnus A from Dreher et al. (1987) and Perley & Carilli

(1996), Hydra A from Taylor & Perley (1993), and 3C465 from Eilek & Owen (2002). Ignoring any considerations about correlated noise, an application of the alignment statistic reveals co-spatial structures in the set of observed maps. The following values are found $A = 0.34, 0.56, 0.64,$ and $0.8,$ which have to be regarded as significant co-alignment signals. These values are anonymised here by numerical ordering. As long as the signal is dominated by map imperfections (correlated noise, artefacts), it is not specified which map gives which A and V values, since this could be regarded as a ranking of the quality of the maps. However, this would be improper, since the observations leading to these maps were driven by other scientific questions than is investigated here. Therefore the maps can not be expected to be optimal for the purposes discussed.

If one uses the uncorrected φ maps instead of φ_0 , one gets only $A = 0.24, 0.35,$ and 0.36 for the three sources for which φ maps were provided. These lower values indicate that the correlation signal is mostly due to noise in the *RM* maps, which imprints itself to the φ_0 map during the φ to $\varphi_0 = \varphi - RM \lambda^2$ correction. This is verified by the gradient vector-product statistics, which leads to $V = -0.32, -0.36, -0.58,$ and -0.69 for the set of maps, which clearly reveals a preferred anti-correlation of *RM* and φ_0 fluctuations. Visual evidence for this can be seen in the upper middle panel of Fig. 2.2, where diagonal stripes decreasing from left to right exhibit the presence of such anti-correlated noise. As argued above, any real astrophysical φ_0 -*RM* correlation should be best detectable in $A + V$, for which one gets values of $A + V = -0.02, -0.02, 0.11,$ and 0.32 . This indicates that at most in one case there could be an astrophysical correlation, however, its significance has to be investigated since one cannot always expect exact cancellation of V and A for correlated noise.

2.4 Avoidable and Unavoidable Correlated Noise in *RM* and φ_0 Maps

As mentioned in the last section, *RM* and φ_0 maps are generated from the same set of radio maps being subject to observational noise. Therefore, the noise of the *RM* and φ_0 maps should be expected to be correlated. In order to understand this correlation, one has to investigate the map making procedure in more detail.

In order to derive the *RM* maps, one requires a number m of polarisation angle φ maps at different wavelengths λ_i , which can be denoted by $\varphi_i(\vec{x})$. As mentioned in Sect. 1.2.4, the first crucial step is to solve the so called $n\pi$ -ambiguity, which arises from the fact that the φ is only defined modulo π , whereas the determination of *RM* requires absolute polarisation angle φ values, since

$$\varphi_i(\vec{x}) = \varphi_0(\vec{x}) + RM(\vec{x}) \lambda_i^2 \quad (2.10)$$

(see Eq.(1.42)) allows φ_i values which deviate more than π from φ_0 . Any mistake in solving this ambiguity leads to strong step-function like artefacts in *RM*, and correlated with these, steps in φ_0 maps. The impact of such steps on any sensitive correlation statistics can be disastrous. Fortunately, such $n\pi$ ambiguities can be strongly suppressed by using map-global algorithms to assign absolute φ 's (see Chapter 4).

However, even if the $n\pi$ -ambiguity is solved, observational noise $\delta\varphi_i$ in individual maps, which is assumed to be independent from map to map, leads to correlated

noise in RM and φ_0 , as described by the following analysis. Typical RM mapping algorithms use a χ^2 statistic, giving

$$RM^{\text{obs}} = (\overline{\lambda^2 \varphi} - \overline{\lambda^2} \overline{\varphi}) / (\overline{\lambda^4} - \overline{\lambda^2}^2), \quad \text{and} \quad \varphi_0^{\text{obs}} = \overline{\varphi} - RM \overline{\lambda^2}, \quad (2.11)$$

where $\overline{Y} = \sum_{i=1}^n Y_i / n$ in order to denote an average of a quantity Y over the different observed wavelengths (compare with Sect. 1.4.1). For the sake of simplicity, one can assume similar noise levels in all maps: $\langle \delta\varphi_i^2 \rangle = \langle \delta\varphi^2 \rangle$. Here, the brackets denote the statistical average and should not be confused with the alignment product. The errors can be written as $\delta RM = RM^{\text{obs}} - RM$ and $\delta\varphi_0 = \varphi_0^{\text{obs}} - \varphi_0$. Inserting Eq. (2.11) into these expressions yields

$$\langle \delta RM^2 \rangle = \langle \delta\varphi^2 \rangle / (n(\overline{\lambda^4} - \overline{\lambda^2}^2)), \quad \langle \delta\varphi_0^2 \rangle = \overline{\lambda^4} \langle \delta RM^2 \rangle, \quad (2.12)$$

and

$$\langle \delta RM \delta\varphi_0 \rangle = -\overline{\lambda^2} \langle \delta RM^2 \rangle, \quad (2.13)$$

which implies an anti-correlation between φ_0 and RM noise, with a correlation coefficient of

$$r = \langle \delta RM \delta\varphi_0 \rangle / \sqrt{\langle \delta RM^2 \rangle \langle \delta\varphi_0^2 \rangle} = -\overline{\lambda^2} / \sqrt{\overline{\lambda^4}}. \quad (2.14)$$

For the set of frequencies used to derive the RM map of PKS 1246-410, one finds $r = -0.89$, therefore, the noise in the RM and φ_0 maps of PKS 1246-410 are expected to be highly anti-correlated. The scalar products of the gradients, which enter the gradient scalar-product statistic V , have expectation values of

$$\langle \vec{\nabla} RM^{\text{obs}} \cdot \vec{\nabla} \varphi_0^{\text{obs}} \rangle = \langle \vec{\nabla} \delta RM \cdot \vec{\nabla} \delta\varphi_0 \rangle = -\langle |\vec{\nabla} \delta\varphi|^2 \rangle \overline{\lambda^2} / (n(\overline{\lambda^4} - \overline{\lambda^2}^2)). \quad (2.15)$$

Similarly, one finds

$$\langle |\vec{\nabla} \delta RM|^2 \rangle = \langle |\vec{\nabla} \delta\varphi|^2 \rangle / (n(\overline{\lambda^4} - \overline{\lambda^2}^2)), \quad (2.16)$$

and

$$\langle |\vec{\nabla} \delta\varphi_0|^2 \rangle = \langle |\vec{\nabla} \delta\varphi|^2 \rangle \overline{\lambda^4} / (n(\overline{\lambda^4} - \overline{\lambda^2}^2)) \quad (2.17)$$

so that for noise dominated maps there is a strong signal in the gradient scalar-product statistic $V = r = -\overline{\lambda^2} / \sqrt{\overline{\lambda^4}}$. In the case of non-constant astrophysical RM and φ_0 values, $|V|$ will be smaller. However, since noise is usually strongest on the smallest scales, the gradient of the noise can easily be stronger than the gradient of the astrophysical signal, leading to $V \sim r$.

2.5 Results

In order to suppress the spurious signal, which should be mostly located on small spatial scales of the order of the observational beam, in the following analysis the RM maps are smoothed with a Gaussian, leaving hopefully only the astrophysical signal carrying large-scale fluctuations. However smoothing a circular quantity like a φ_0 angle is not uniquely defined. A summary of the results are given in Tab. 2.1 which are discussed in more detail in the following.

source	FWHM _{beam}	A	V	$A + V$
PKS 1246-410	4''	0.07	-0.17	-0.10
Cygnus A	2''	0.07	-0.07	0.00
Hydra A	1''	0.05	-0.03	0.02
3C465	9.5''	0.13	0.03	0.16
$\varphi_0^{\text{east}}-RM^{\text{west}}$		-0.02	-0.02	-0.21
$\varphi_0^{\text{west}}-RM^{\text{east}}$		0.10	-0.30	-0.20
independent		0.06	0.05	0.11
co-aligned		0.89	-0.03	0.86

Table 2.1: The values for the statistics A and V obtained for various data sets. In the upper part of the table the resulting values for the statistics of the observational data are presented. For this data the FWHM is given to which the maps were smoothed. In the middle part, the values obtained for the exchanged subregions of PKS 1246-410 are given which can serve as an estimate of the statistical uncertainty. For comparison the lower part summarises the values obtained for a realisation of independent and co-aligned RM and φ_0 maps.

Applying the statistics to the data at hand (see the end of Sect. 2.3) yields for PKS1246-410 $A = 0.07$, $V = -0.17$, $A + V = -0.10$ (after smoothing to a 4'' FWHM beam), for Cygnus A $A = 0.07$, $V = -0.07$, $A + V = 0.00$ (FWHM = 2''), for Hydra A $A = 0.05$, $V = -0.03$, $A + V = 0.02$ (FWHM = 1''), and for 3C465 $A = 0.13$, $V = 0.03$, $A + V = 0.16$ (FWHM = 9.5''). Only 3C465 shows a marginal signature of source intrinsic co-alignment. However, its map size in terms of resolution elements is significantly smaller than e.g. the maps of Hydra A and Cygnus A, therefore a larger statistical variance of the alignment measurement is plausible.

In contrast to the observed maps, the synthetic maps are free of correlated noise. This is clearly revealed by the statistics, which give for the independent pair of maps $A = 0.06$, $V = 0.05$, $A + V = 0.11$, and for the co-aligned pair of maps $A = 0.89$, $V = -0.03$, $A + V = 0.86$. This illustrates the ability of the statistics introduced to discriminate between spurious and astrophysical signals.

In order to have an estimate of the statistical uncertainties, the approach was also applied to the swapped RM map of PKS 1246-410. This yields for the $\varphi_0^{\text{east}}-RM^{\text{west}}$ comparison $A = -0.02$, $V = -0.19$, $A + V = -0.21$, and for the $\varphi_0^{\text{west}}-RM^{\text{east}}$ comparison $A = 0.10$, $V = -0.30$, $A + V = -0.20$. This indicates that the statistical error is of the order $\delta A \sim 0.1$ and $\delta V \sim 0.2$ for this dataset, taking into account that the swapped maps have less corresponding pixel pairs compared to the original pair of maps.

Note that an inspection by eye reveals several sharp steps in the original RM map of PKS 1246-410, which are on length-scales below the beam size and therefore very likely map making artefacts (see Sect. 2.4). Thus, it is uncertain if this dataset has sufficiently high signal-to-noise to make it suitable for a φ_0 - RM alignment analysis.

In summary it can be concluded that no evidence for a significant large-scale co-alignment of φ_0 and RM maps of polarised radio sources in galaxy clusters was found.

Independent evidence for the validity of the assumption of an external Faraday screen can be found in the detection of the Laing-Garrington effect which was already mentioned in Sect. 1.3.2. It manifests itself by an asymmetric Faraday depolarisation of double radio lobes located within galaxy clusters (Garrington et al. 1988; Laing 1988). This asymmetry is caused by different path lengths for radio emission through the Faraday active medium between source and observer as suggested by Garrington & Conway (1991). However, this effect could also be explained by an asymmetric mixing layer being thin close to the head side of a FR II while getting thicker on the back-flow side of it. However, this explanation fails to give a convincing explanation for the large RM and depolarisation asymmetry observed for the FR I source Hydra A (Taylor & Perley 1993).

Further independent evidence for cluster wide magnetic fields is provided by the recent statistical RM investigation of point sources performed by Clarke et al. (2001) mentioned in Sect. 1.3.2. As described, it revealed larger RM values for sources observed through the intra-cluster gas in comparison to a control sample of sources where no intra-cluster gas was located between source and observer. This suggests that the enhancement of the RM towards the cluster centre results most probably from the magnetised cluster gas.

2.6 Conclusions

It was investigated if there is evidence for co-aligned structures in RM and φ_0 maps of extended radio sources in galaxy clusters as claimed by Rudnick & Blundell (2003) in order to argue for source-local RM generating magnetic fields.

First, it was demonstrated that the experiment performed by Rudnick & Blundell was poorly designed for testing the correlation between φ_0 and RM in PKS 1246-410. The lack of phase coherence in their simulated data resulted in less clustering in the simulated φ_0 - RM scatter plots compared to the observational scatter plots. Using independent, patchy distributions of φ_0 and RM it was shown that the correlations due to the mutual overlap of the RM and φ_0 patches produce horizontal and vertical chains of clusters as seen in the PKS 1246-410 data, whereas co-aligned φ_0 and RM patches produce diagonal stripes. The observed clustering therefore favours independent φ_0 and RM maps as expected from foreground intra-cluster magnetic fields.

Second, a novel *gradient alignment statistic* A was introduced. This statistic reveals φ_0 and RM correlations regardless of whether they are source intrinsic or due to artefacts in the observation or the RM map making process. Applying this statistic to a number of radio galaxies (PKS 1246-410, Cygnus A, Hydra A, and 3C465) does not reveal any significant large-scale co-alignment of φ_0 and RM maps. Significant small-scale co-alignment is found in all observed map pairs, but they can be fully identified with map making artefacts by another new suitable statistical test, the *gradient vector product statistic* V . Thus, two new tools were introduced in order to analyse data of Faraday rotation studies of extended radio sources. They are powerful in revealing and discriminating observational or map making artefacts (by V), and source-intrinsic φ_0 - RM correlations (by $A + V$), both are indicators of potential problems for RM based intra-cluster magnetic field estimates.

Future, sensitive searches for potential, weak source-intrinsic φ_0 - RM correlations

with the statistics developed above, or similar statistics would require observational datasets with a much higher signal to noise ratio, and a very well defined observational (*dirty*) beam. Note such datasets would also be crucial for detailed measurements of the magnetic power spectra of the intra-cluster medium, as proposed in the following Chapter 3.

In conclusion, the observed RM signals of radio galaxies embedded in galaxy clusters seem to be dominated by $\sim \mu\text{G}$ cluster magnetic fields in accordance with independent evidence.

Chapter 3

Measuring the Cluster Magnetic Field Power Spectra of Three Galaxy Clusters

In the last chapter, evidence was given for the validity of the assumption that the Faraday rotating medium is external to the radio source and can be identified with the intra-cluster gas – the ICM. Thus, the analysis of Faraday rotation maps of extended polarised radio sources located behind or embedded in galaxy clusters allows to understand the magnetic field strength and to get some hints about the structure of cluster magnetic fields.

A method relying on statistical methods in order to derive the magnetic field power spectrum from the RM autocorrelation function is developed in this chapter. The application of this approach to observational data and the difficulties involved are described. Emphasis is given to a critical discussion of the strengths and limits of the approach.

This work is published as Enßlin & Vogt (2003) and Vogt & Enßlin (2003). My part in this work was the contribution to the development of the formalism and the complete implementation in a computer code and the data handling involved.

3.1 Introduction

As mentioned in Sect. 1.2.4, the traditional analysis of RM maps assumes that the Faraday screen consists of cells which have a uniform size and a constant magnetic field strength with from cell to cell randomly varying field directions. The mean RM which would be produced by such a screen builds up in a random walk process and thus, has a zero mean but a non vanishing dispersion. This dispersion will be proportional to the square root of the number of cells along the line of sight, the cell size, the electron density profile and the magnetic field strength (see Eq. (1.47)).

However, there are some drawbacks to such a cell model. First of all, the divergence of the magnetic field in such a Faraday screen would be nonzero which contradicts Maxwell's equations. Secondly, a spectrum of scales for the cell sizes is more likely than a single scale.

Another important issue in previous analyses is the assumption that the RM ordering scale read off RM maps is equivalent to the magnetic field's characteristic length scale, the autocorrelation length λ_B . This might have led to underestimations of field strengths in the past since another simpler equation than Eq. (1.47) often used for the derivation of the magnetic field strength is

$$\langle B_z^2 \rangle = \frac{\langle RM^2 \rangle}{a_0^2 n_e^2 L \lambda_z}, \quad (3.1)$$

where $\langle RM^2 \rangle$ is the RM dispersion, L is the depth of the Faraday screen, $a_0 = e^3 / (2\pi m_e^2 c^4)$, n_e is the electron density and λ_z is a characteristic length scale of the fields. At this point it becomes clear that the definition of the characteristic length scale λ_z is crucial for the derivation of magnetic field strength. The assumption of a constant magnetic field throughout the cluster leads to a definition of $\lambda_z = L$ and thus, $\langle B_z^2 \rangle \propto L^{-2}$. The characteristic length scale for the cell model would be the size of each cell $\lambda_z = l_{cell}$. Another definition one could think of is the RM ordering scale, $\lambda_z = \lambda_{RM}$. However, the correct length scale is the autocorrelation length λ_z of the z -component of the magnetic field measured along the line of sight.

In order to overcome such limitations, a purely statistical approach which incorporates the vanishing divergence of the magnetic field is developed in Sect. 3.3 whereas its philosophy is outlined in Sect. 3.2. This approach relies on the assumption that the fields are statistically isotropically distributed in Faraday screens such that the z -component is representative for all components. Starting from this assumption, a relation between the observationally accessible RM autocorrelation function and the magnetic autocorrelation tensor is established in real and in Fourier space such that one gains access to the power spectrum of the magnetic field inhabited by the Faraday screen.

In Sect. 3.4, this statistical analysis is applied to observational data by reanalysing the Faraday rotation measure maps of three extended extragalactic radio sources: Hydra A (Taylor & Perley 1993), 3C75 and 3C465 (Eilek & Owen 2002) which were kindly provided by Greg Taylor, Jean Eilek and Frazer Owen, respectively. The results are presented and discussed in Sect. 3.5.

Throughout the rest of this chapter a Hubble constant of $H_0 = 70 \text{ km s}^{-1} \text{ Mpc}^{-1}$, $\Omega_m = 0.3$ and $\Omega_\Lambda = 0.7$ in a flat universe is assumed.

3.2 The Philosophy

If magnetic fields are sampled in a sufficiently large volume, they can hopefully be regarded to be statistically homogeneous and statistically isotropic. This means that any statistical average of a quantity depending on the magnetic fields does not depend on the exact location, shape, orientation and size of the used sampling volume.

The quantity which is of interest is the autocorrelation (or two-point-correlation) function (more exactly: tensor) of the magnetic fields. The information contained in the autocorrelation function is equivalent to the information stored in the power spectrum, as stated by the Wiener-Khinchin Theorem (WKT) (compare Sect. 1.4.2). Therefore, two equivalent approaches are presented, one based in real space, and one based in Fourier space. The advantage of this redundancy is that some quantities are

easier accessible in one, and others in the other space. Further, this allows to cross-check computer algorithms based on this work by comparing results gained by the different approaches.

Faraday rotation maps of extended polarised radio sources located behind or embedded in a Faraday screen are the observables which can be used to access the magnetic fields. Since an RM map shows basically the line-of-sight projected magnetic field distribution, the RM autocorrelation function is mainly given by the projected magnetic field autocorrelation function. Therefore, measuring the RM autocorrelation allows to measure the magnetic autocorrelation, and thus, provides a tool to estimate magnetic field strength and correlation length.

The situation is a bit more complicated than described above, due to the vector nature of the magnetic fields. This implies that there is an autocorrelation tensor instead of a function, which contains nine numbers corresponding to the correlations of the different magnetic components against each other, which in general can all be different. The RM autocorrelation function contains only information about one of these values, the autocorrelations of the magnetic field component parallel to the line-of-sight. However, in many instances the important symmetric part of the tensor can be reconstructed and using this information the magnetic field strength and correlation length can be obtained. This is possible due to three observations:

1. **Magnetic isotropy:** If the sampling volume is sufficiently large, so that the local anisotropic nature of magnetic field distributions is averaged out, the (volume averaged) magnetic autocorrelation tensor is isotropic. This means, that the diagonal elements of the tensor are all the same, and that the off-diagonal elements are described by two numbers, one giving their symmetric, and one giving their anti-symmetric (helical) contribution.
2. **Divergence-freeness of magnetic fields:** The condition $\vec{\nabla} \cdot \vec{B} = 0$ couples the diagonal and off-diagonal components of the symmetric part of the autocorrelation tensor. Knowledge of one diagonal element (e.g. from an RM measurement) therefore specifies fully the symmetric part of the tensor. The trace of the autocorrelation tensor, which can be called *scalar magnetic autocorrelation function* $w(r)$, contains all the information required to measure the average magnetic energy density $\varepsilon_B = w(0)/(8\pi)$ or the magnetic correlation length $\lambda_B = \int_{-\infty}^{\infty} dr w(r)/w(0)$.
3. **Unimportance of helicity:** Although helicity is a crucial quantity for the dynamics of magnetic fields, it does not enter any estimate of the average magnetic energy density, or magnetic correlation length, because helicity only affects off-diagonal terms of the autocorrelation tensor. The named quantities depend only on the trace of the tensor and are therefore unaffected by helicity. One cannot measure helicity from a Faraday rotation map alone, since it requires the comparison of two different components of the magnetic fields, whereas the RM map contains information on only one component.

In a realistic situation, the sampling volume is determined by the shape of the polarised radio emitter and the geometry of the Faraday screen, as given by the electron density and the magnetic field energy density profile. The sampling volume can

be described by a window function, through which an underlying virtually statistical homogeneous magnetic field is observed. The window function is zero outside the probed volume, e.g. for locations which are not located in front of the radio source. Inside the volume, the window function scales with the electron density (known from X-ray observations), with the average magnetic energy profile (guessed from reasonable scaling relations, but testable within the approach), and – if wanted – with a noise reducing data weighting scheme.

The effect of a finite window function is to smear out the power in Fourier-space. Since this is an unwanted effect one either has to find systems which provide a sufficiently large window or one has to account for this bias. The effect of a too small window on the results depends strongly on the shape and the size of the window. However, one can assess the influence of a finite window but it has to be done for each application at hand separately. In general, the analysis is sensitive to magnetic power on scales below a typical window size, and insensitive to scales above.

The same magnetic power spectrum can have very different realisations, since all the phase information is lost in measuring the power spectrum (for an instructive visualisation of this see Maron & Goldreich 2001). Since the presented approach relies on the power spectrum only, it is not important if the magnetic fields are highly organised in structures like flux-ropes, or magnetic sheets, or if they are relatively featureless random-phase fields, as long as their power spectrum is the same.

The autocorrelation analysis is fully applicable in all such situations, as long as the fields are sampled with sufficient statistics. The fact that this analysis is insensitive to different realisations of the same power spectrum indicates that the method is not able to extract all the information which may be contained in the map. Additional information is stored in higher order correlation functions, and such can in principle be used to make statements about whether the fields are ordered or purely random (chaotic). The information on the magnetic field strength (\overline{B}^2 , which is the value at origin of the autocorrelation function), and correlation length (an integral over the autocorrelation function) does only depend on the autocorrelation function and not on the higher order correlations.

The presented analysis relies on having a statistically isotropic sample of magnetic fields, whereas MHD turbulence seems to be locally inhomogeneous, which means that small scale fluctuations are anisotropic with respect to the local mean field. However, whenever the observing window is much larger than the correlation length of the local mean field the autocorrelation tensor should be isotropic due to averaging over an isotropic distribution of locally anisotropic subvolumes. This works if not a preferred direction is superposed by other physics, e.g. a galaxy cluster wide orientation of field lines along a preferred axis. However, even this case can in principle be treated by co-adding the RM signal from a sample of clusters, for which a random distribution of such hypothetical axes can be assumed. In any case, it is likely that magnetic anisotropy also manifests itself in the Faraday rotation maps, since the projection connecting magnetic field configurations and RM maps will conserve anisotropy in most cases, except alignments by chance of the direction of anisotropy and the line-of-sight.

There are cases where already an inspection by eye seems to reveal the existence of magnetic structures like flux ropes or magnetic sheets. As already stated, the presence of such structures does not limit the analysis, as long as they are sufficiently sampled. Otherwise, one has to replace e.g. the isotropy assumption by a suitable generalisation.

In many cases, this will allow an analysis similar to the one described here.

3.3 The Method

3.3.1 Real Space Formulation

For a line of sight parallel to the z-axis and displaced by \vec{x}_\perp from it, the Faraday rotation measure arising from polarised emission passing from the source at $z_s(\vec{x}_\perp)$ through a magnetised medium to the observer located at infinity is expressed by

$$RM(\vec{x}_\perp) = a_0 \int_{z_s(\vec{x}_\perp)}^{\infty} dz n_e(\vec{x}) B_z(\vec{x}), \quad (3.2)$$

where $a_0 = e^3/(2\pi m_e^2 c^4)$, $\vec{x} = (\vec{x}_\perp, z)$, $n_e(\vec{x})$ is the electron density and $B_z(\vec{x})$ is the magnetic field component parallel to the line of sight. In the following, any redshift effects are neglected, which can be included by inserting the factor $(1 + z_{\text{redshift}}(z))^{-2}$ into the integrand.

The focus of this work is on the statistical expectation of the two-point, or auto-correlation function of Faraday rotation maps which can be defined as

$$C_{RM}(\vec{r}_\perp) = \langle RM(\vec{x}_\perp) RM(\vec{x}_\perp + \vec{r}_\perp) \rangle_{\vec{x}_\perp}, \quad (3.3)$$

where the brackets indicate the map average with respect to \vec{x}_\perp . However, an observed RM map is limited in size which leads to noise in the calculation of the correlation function on large scales since less pixel pairs contribute to the correlation function for larger pixel separations. In order to suppress this under-sampling, the observable correlation function can be defined as

$$C_{RM}^{\text{obs}}(r_\perp) = \frac{1}{A_\Omega} \int dx_\perp^2 RM(\vec{x}_\perp) RM(\vec{x}_\perp + \vec{r}_\perp), \quad (3.4)$$

where the area A_Ω of the region Ω for which RM 's are actually measured is used as normalisation assuming that $RM(\vec{x}_\perp) = 0$ for $\vec{x}_\perp \notin \Omega$. Furthermore, it is required that the mean RM is zero since statistically isotropic divergence free fields have a mean RM of zero to high accuracy. A non vanishing mean RM in the observational data stems from foregrounds (e.g. the galaxy) which are of no interest here or has its origin in large scale fields to which the approach is insensitive by construction in order to suppress statistically under-sampled length scales.

As stated in Sect. 3.2, the virtually homogeneous magnetic field component can be thought to be observed through a window function $f(\vec{x})$ which describes the sampling volume. One would chose a typical position in the cluster \vec{x}_{ref} (e.g. its centre) and define $n_{e0} = n_e(\vec{x}_{\text{ref}})$ and $\vec{B}_0 = \langle \vec{B}^2(\vec{x}_{\text{ref}}) \rangle^{1/2}$. The window function can then be expressed as

$$f(\vec{x}) = \mathbf{1}_{\{\vec{x}_\perp \in \Omega\}} \mathbf{1}_{\{z \geq z_s(\vec{x}_\perp)\}} h(\vec{x}_\perp) g(\vec{x}) n_e(\vec{x}) / n_{e0}, \quad (3.5)$$

where $\mathbf{1}_{\{\text{condition}\}}$ is equal to one if the condition is true and zero if not. The dimensionless average magnetic field profile $g(\vec{x}) = \langle \vec{B}^2(\vec{x}) \rangle^{1/2} / B_0$ is assumed to scale with the density profile such that $g(\vec{x}) = (n_e(\vec{x}) / n_{e0})^{\alpha_B}$. Reasonable values for the exponent α_B range between 0.5 and 1 (see Sect. 1.3.2).

The function $h(\vec{x})$ allows to assign different pixels in the map different weights. If $h(\vec{x}_\perp) \neq 1$ for some $\vec{x}_\perp \in \Omega$ the corresponding weight has to be introduced into the analysis. The most efficient way to do this is to make the data weighting virtually part of the measurement process, by writing $RM(\vec{x}_\perp) \rightarrow RM^w(\vec{x}_\perp) = RM(\vec{x}_\perp) h(\vec{x}_\perp)$. For convenience, the superscript^w is dropped again in the following, and just noted that the analysis described here has to be applied to the weighted data $RM^w(\vec{x}_\perp)$.

In cases where the noise is a function of the position one might want to down-weight noisy regions. If $\sigma(\vec{x}_\perp)$ is the noise of the RM map at position \vec{x}_\perp , a reasonable choice of a weighting function would be $h(\vec{x}_\perp) = \sigma_0/\sigma(\vec{x}_\perp)$. If the noise map itself could have errors, the danger of over-weighting noisy pixels with underestimated noise can be avoided by thresholding: If σ_0 is a threshold below which the noise is regarded to be tolerable, one can use $h(\vec{x}_\perp) = 1/(1 + \sigma(\vec{x}_\perp)/\sigma_0)$. Another choice would be $h(\vec{x}_\perp) = \mathbf{1}_{\{\sigma(\vec{x}_\perp) < \sigma_0\}}$ which just cuts out regions which are recognised as too noisy. If no weighting applies, $h(\vec{x}_\perp) = 1$ everywhere.

The expectation of the observed RM correlations are

$$\langle C_{RM}^{\text{obs}}(\vec{r}_\perp) \rangle = \frac{a_0^2 n_{e0}^2}{A_\Omega} \int d^3x \int_{-\infty}^{\infty} dr_z f(\vec{x}) f(\vec{x} + \vec{r}) \langle \tilde{B}_z(\vec{x}) \tilde{B}_z(\vec{x} + \vec{r}) \rangle, \quad (3.6)$$

with $\vec{r} = (\vec{r}_\perp, r_z)$, and $\tilde{B}(\vec{x}) = \vec{B}(\vec{x})/g(\vec{x})$ is the rescaled magnetic field. If properly rescaled, the average strength of the field is independent of the position. In that case, the rescaled magnetic field autocorrelation tensor should also be independent of position:

$$M_{ij}(\vec{r}) = \langle \tilde{B}_i(\vec{x}) \tilde{B}_j(\vec{x} + \vec{r}) \rangle. \quad (3.7)$$

If the spatial variation of the window function is on much larger scales than the correlation length λ_B of the magnetic fields, then Eq. (3.6) can be approximated to be

$$\begin{aligned} C_{RM}(\vec{r}_\perp) &= \langle C_{RM}^{\text{obs}}(\vec{r}_\perp) \rangle = a_1 C_\perp(\vec{r}_\perp), \text{ with } a_1 = a_0^2 n_{e0}^2 L, \\ C_\perp(\vec{r}_\perp) &= \int_{-\infty}^{\infty} dr_z M_{zz}(\vec{r}), \text{ and } \vec{r} = (\vec{r}_\perp, r_z). \end{aligned} \quad (3.8)$$

where the characteristic depth of the Faraday screen $L = V_{[f]}/A_\Omega$ was introduced, where $V_{[f]} = \int d^3x f^2(\vec{x})$ is the probed effective volume. The normalised RM autocorrelation function C_\perp which differs from C_{RM} only by a geometry dependent factor a_1 is introduced for convenience.

In the following, the influence of the window function is ignored in the discussion, since for sufficiently large windows it only affects a_1 . Therefore, \vec{B} is written for \tilde{B} and one has to keep in mind that the measured field strength B_0 is estimated for a volume close to the reference location \vec{x}_{ref} . At other locations, the average magnetic energy density is given by $\varepsilon_B(\vec{x}) = g^2(\vec{x}) B_0^2$. This approach assumes implicitly that typical length scales are the same throughout the Faraday screen. For sufficiently extended screens, this assumption can be tested by comparing results from different and separately analysed regions of the RM map.

The magnetic autocorrelation tensor for homogeneous isotropic turbulence, as assumed throughout the rest of this chapter, can be written as

$$M_{ij}(\vec{r}) = M_N(r) \delta_{ij} + (M_L(r) - M_N(r)) \frac{r_i r_j}{r^2} + M_H(r) \epsilon_{ijk} r_k \quad (3.9)$$

(e.g. Subramanian 1999) where the longitudinal, normal, and helical autocorrelation functions, $M_L(r)$, $M_N(r)$, and $M_H(r)$, respectively, only depend on the distance, not on the direction. The condition $\vec{\nabla} \cdot \vec{B} = 0$ leads to $\partial/\partial r_i M_{ij}(\vec{r}) = 0$ (here and below the sum convention is used). This allows to connect the non-helical correlation functions by

$$M_N(r) = \frac{1}{2r} \frac{d}{dr} (r^2 M_L(r)) \quad (3.10)$$

(Subramanian 1999). The zz -component of the magnetic autocorrelation tensor depends only on the longitudinal and normal correlations, and not on the helical part:

$$M_{zz}(\vec{r}) = M_L(r) \frac{r_z^2}{r^2} + M_N(r) \frac{r_\perp^2}{r^2} \text{ with } \vec{r} = (\vec{r}_\perp, r_z), \quad (3.11)$$

which implies that Faraday rotation is insensitive to magnetic helicity. It is also useful to introduce the magnetic autocorrelation function

$$w(\vec{r}) = \langle \vec{B}(\vec{x}) \cdot \vec{B}(\vec{x} + \vec{r}) \rangle = M_{ii}(\vec{r}), \quad (3.12)$$

which is the trace of the autocorrelation tensor, and depends only on r (in the case of a statistically isotropic magnetic field distribution, in the following called briefly *isotropic turbulence*):

$$w(\vec{r}) = w(r) = 2M_N(r) + M_L(r) = \frac{1}{r^2} \frac{d}{dr} (r^3 M_L(r)). \quad (3.13)$$

In the last step, Eq. (3.10) was used. Since the average magnetic energy density is given by $\langle \varepsilon_B \rangle = w(0)/(8\pi)$ the magnetic field strength can be determined by measuring the zero-point of $w(r)$. This can be done by Faraday rotation measurements: The RM autocorrelation can be written as

$$C_\perp(r_\perp) = \frac{1}{2} \int_{-\infty}^{\infty} dr_z w(\sqrt{r_\perp^2 + r_z^2}) = \int_{r_\perp}^{\infty} dr \frac{r w(r)}{\sqrt{r^2 - r_\perp^2}}. \quad (3.14)$$

and is therefore just a line-of-sight projection of the magnetic autocorrelations. Thus, the magnetic autocorrelations $w(r)$ can be derived from $C_\perp(r_\perp)$ by inverting an Abel integral equation:

$$w(r) = -\frac{2}{\pi r} \frac{d}{dr} \int_r^\infty dy \frac{y C_\perp(y)}{\sqrt{y^2 - r^2}} \quad (3.15)$$

$$= -\frac{2}{\pi} \int_r^\infty dy \frac{C'_\perp(y)}{\sqrt{y^2 - r^2}}, \quad (3.16)$$

where the prime denotes a derivative. For the second equation, it was used that $w(r)$ stays bounded for $r \rightarrow \infty$.

Now, an observational program to measure magnetic fields is obvious: From a high quality Faraday rotation map of a homogeneous, (hopefully) isotropic medium of known geometry and electron density (e.g. derived from X-ray maps) the RM autocorrelation has to be calculated (Eq. (3.8)). From this an Abel integration (Eq. (3.15) or (3.16)) leads to the magnetic autocorrelation function, which gives $\langle B^2 \rangle$ at its origin. Formally,

$$\langle B^2 \rangle = w(0) = -\frac{2}{\pi} \int_0^\infty dy \frac{C'_\perp(y)}{y}, \quad (3.17)$$

but this formulation is notoriously sensitive to noise. More stable methods are presented later.

The magnetic autocorrelation length λ_B can be calculated by integrating the correlation functions:

$$\begin{aligned}\lambda_B &= \int_{-\infty}^{\infty} dr \frac{\langle B(\vec{x} + r\vec{e}) \cdot B(\vec{x}) \rangle_{\vec{x}, \vec{e}}}{\langle B^2(\vec{x}) \rangle} \\ &= \int_{-\infty}^{\infty} dr \frac{w(r)}{w(0)} = 2 \frac{C_{\perp}(0)}{w(0)},\end{aligned}\quad (3.18)$$

where \vec{e} and \vec{e}_{\perp} are 3- and 2-dimensional unit vectors, respectively, over which the averaging takes place. For the derivation of the last expressions, Eq. (3.14) or (3.16) can be used. Even in globally homogeneous turbulence, there is always a preferred direction defined by the local magnetic field. One can ask for the correlation length along and perpendicular to this locally defined direction and gets $\lambda_{\parallel} = \frac{3}{2}\lambda_B$, and $\lambda_{\perp} = \frac{3}{4}\lambda_B$ so that $\lambda_B = \frac{1}{3}(\lambda_{\parallel} + 2\lambda_{\perp})$.

An observationally easily accessible length scale is the Faraday rotation autocorrelation length λ_{RM}

$$\begin{aligned}\lambda_{RM} &= \int_{-\infty}^{\infty} dr \frac{\langle RM(\vec{x} + r\vec{e}_{\perp}) RM(\vec{x}) \rangle_{\vec{x}, \vec{e}_{\perp}}}{\langle RM^2(\vec{x}) \rangle} \\ &= \int_{-\infty}^{\infty} dr_{\perp} \frac{C_{\perp}(r_{\perp})}{C_{\perp}(0)} = \pi \frac{\int_{-\infty}^{\infty} dr r w(r)}{\int_{-\infty}^{\infty} dr w(r)}\end{aligned}\quad (3.19)$$

From the comparison of Eq. (3.18) and (3.19), it is obvious that the RM correlation length-scale is not identical to the magnetic field autocorrelation length. As shown later, the RM correlation length is more strongly weighted towards the largest length-scales in the magnetic fluctuation spectrum than the magnetic correlation length. This is crucial, since in some cases these scales have been assumed to be identical, which could have led to systematic underestimates of magnetic field strengths.

3.3.2 Fourier Space Formulation

The following convention for the Fourier transformation of a n -dimensional function $F(\vec{x})$ is used:

$$\hat{F}(\vec{k}) = \int d^n x F(\vec{x}) e^{i\vec{k}\cdot\vec{x}} \quad (3.20)$$

$$F(\vec{x}) = \frac{1}{(2\pi)^n} \int d^n k \hat{F}(\vec{k}) e^{-i\vec{k}\cdot\vec{x}}. \quad (3.21)$$

Then the Fourier transformed isotropic magnetic autocorrelation tensor reads

$$\hat{M}_{ij}(\vec{k}) = \hat{M}_N(k) \left(\delta_{ij} - \frac{k_i k_j}{k^2} \right) - i\varepsilon_{ijm} \frac{k_m}{k} \hat{H}(k), \quad (3.22)$$

where it is directly used that $\vec{\nabla} \cdot \vec{B} = 0$ in the form $k_i \hat{M}_{ij}(\vec{k}) = 0$ to reduce the degrees of freedom to two components, a normal and helical part. The two corresponding spherically symmetric functions in k -space are given in terms of their real

space counterparts as:

$$\hat{M}_N(k) = \int d^3r M_N(r) e^{i\vec{k}\cdot\vec{r}} = 4\pi \int_0^\infty dr r^2 M_N(r) \frac{\sin(kr)}{kr} \quad (3.23)$$

$$\begin{aligned} \hat{H}(k) &= \frac{d}{dk} \hat{M}_H(k) = \frac{d}{dk} \int d^3r M_H(r) e^{i\vec{k}\cdot\vec{r}}, \\ &= \frac{4\pi}{k} \int_0^\infty dr r^2 M_H(r) \frac{kr \cos(kr) - \sin(kr)}{kr}. \end{aligned} \quad (3.24)$$

One can also introduce the Fourier transformed trace of the autocorrelation tensor $\hat{w}(\vec{k}) = \hat{M}_{ii}(\vec{k}) = 2\hat{M}_N(k)$. A comparison with the transformed zz -component of the autocorrelation tensor

$$\hat{M}_{zz}(\vec{k}) = \hat{M}_N(k) \left(1 - k_z^2/k^2\right) \quad (3.25)$$

reveals that in the $k_z = 0$ plane, these two functions are identical (up to a constant factor 2). Since the 2-d Fourier transformed normalised RM map is also identical to this, as a transformation of Eq. (3.8) shows, one can state

$$\hat{C}_\perp(\vec{k}_\perp) = \hat{M}_{zz}(\vec{k}_\perp, 0) = \frac{1}{2} \hat{w}(\vec{k}_\perp, 0). \quad (3.26)$$

This Fourier-space version of Eq. (3.14) says, that the 2-d transformed RM map reveals the $k_z = 0$ plane of $\hat{M}_{zz}(\vec{k})$, which in the isotropic case is all what is required to reconstruct the full magnetic autocorrelation $\hat{w}(k) = 2\hat{C}_\perp(k)$.

A power spectrum $P_{[F]}(\vec{k})$ of a function $F(\vec{x})$ is given by the absolute-square of its Fourier transformation $P_{[F]}(\vec{k}) = |\hat{F}(\vec{k})|^2$. The WKT states that the Fourier transformation of an autocorrelation function $C_{[F]}(\vec{r})$, estimated within a window with volume V_n (as in Eq. (3.4)), gives the (windowed) power spectrum of this function, and vice versa:

$$P_{[F]}(\vec{k}) = V_n \hat{C}_{[F]}(\vec{k}). \quad (3.27)$$

The WKT allows to write the Fourier transformed autocorrelation tensor as

$$\hat{M}_{ij}(\vec{k}) = \frac{1}{V} \langle \hat{B}_i(\vec{k}) \overline{\hat{B}_j(\vec{k})} \rangle, \quad (3.28)$$

where V denotes the volume of the window function, which is for practical work with RM maps often the probed effective volume $V = V_{[f]}$ as defined in Sect. 3.3.1.

Thus, the 3-d magnetic power spectrum (the Fourier transformed magnetic autocorrelation function $w(\vec{r})$) can be directly connected to the one-dimensional magnetic energy spectrum in the case of isotropic turbulence:

$$\varepsilon_B(k) dk = \frac{4\pi k^2}{(2\pi)^3} \frac{\hat{w}(k)}{8\pi} dk = \frac{k^2 \hat{w}(k)}{2(2\pi)^3} dk, \quad (3.29)$$

where $\hat{w}(\vec{k}) = \hat{w}(k)$ is due to isotropy. The WKT also connects the 2-dimensional Fourier transformed RM map with the Fourier transformed RM autocorrelation function:

$$\hat{C}_\perp(k_\perp) = \frac{\langle |R\hat{M}(k_\perp)|^2 \rangle}{a_1 A_\Omega}. \quad (3.30)$$

Thus, by comparing Eqs. (3.26), (3.29), and (3.30), one finds that the magnetic energy spectrum is most easily measured from a given observation by simply Fourier transforming the $RM(\vec{x}_\perp)$ map, and averaging this over rings in \vec{k}_\perp -space:

$$\varepsilon_B^{\text{obs}}(k) = \frac{k^2}{a_1 A_\Omega (2\pi)^4} \int_0^{2\pi} d\phi |R\hat{M}(\vec{k}_\perp)|^2 \quad (3.31)$$

where $\vec{k}_\perp = k(\cos\phi, \sin\phi)$. Eq. (3.31) gives a direct model independent observational route to measure the turbulent energy spectrum. The average magnetic energy density can be easily obtained from this via

$$\varepsilon_B^{\text{obs}} = \int_0^\infty dk \varepsilon_B^{\text{obs}}(k) = \int d^2k_\perp \frac{k_\perp |R\hat{M}(\vec{k}_\perp)|^2}{a_1 A_\Omega (2\pi)^4}, \quad (3.32)$$

where the last integration extends over the Fourier transformed RM map and can be done in practice by summing over pixels.

Also the correlation lengths can be expressed in terms of $\hat{w}(k)$:

$$\lambda_B = \pi \frac{\int_0^\infty dk k \hat{w}(k)}{\int_0^\infty dk k^2 \hat{w}(k)}, \quad (3.33)$$

$$\lambda_{RM} = 2 \frac{\int_0^\infty dk \hat{w}(k)}{\int_0^\infty dk k \hat{w}(k)}. \quad (3.34)$$

Thus, the RM correlation length has a much larger weight on the large-scale fluctuations than the magnetic correlation length has. Equating these two length-scales, as sometimes done in the literature, is at least questionable in the likely case of a broader turbulence spectrum. In typical situations (e.g. for a broad maximum of the magnetic power spectrum as often found in hydrodynamical turbulence), one expects $\lambda_B < \lambda_{RM}$.

The isotropic magnetic autocorrelation function can be expressed as

$$w(r) = \frac{4\pi}{(2\pi)^3} \int_0^\infty dk k^2 \hat{w}(k) \frac{\sin(kr)}{kr}. \quad (3.35)$$

Similarly, the RM autocorrelation function can be written as

$$C_\perp(r_\perp) = \frac{1}{4\pi} \int_0^\infty dk k \hat{w}(k) J_0(kr_\perp), \quad (3.36)$$

where $J_n(x)$ is the n -th Bessel function. In order to analyse the behaviour of the RM autocorrelations close to the origin, it is useful to rewrite the last equation as:

$$C_\perp(r_\perp) = \int_0^\infty dk \frac{k \hat{w}(k)}{4\pi} - \int_0^\infty dk \frac{k \hat{w}(k)}{4\pi} (1 - J_0(kr_\perp)). \quad (3.37)$$

The first term gives $C_\perp(0)$, and the second describes how $C_\perp(r_\perp)$ approaches zero for $r_\perp \rightarrow \infty$.

3.3.3 Testing the Model & Influences of Observational Artefacts

Now, all the necessary tools are introduced to test if the window function $f(\vec{x})$ was based on a sensible model for the average magnetic energy density profile $g^2(\vec{x})$ and the proper geometry of the radio source within the Faraday screen $z_s(\vec{x}_\perp)$ (see Eq. (3.5)). Models can eventually be excluded a-posteriori on the basis of

$$\chi^2(x_\perp) = \frac{RM(\vec{x}_\perp)^2}{\langle RM(\vec{x}_\perp)^2 \rangle}, \quad (3.38)$$

where for the expected RM dispersion

$$\langle RM(\vec{x}_\perp)^2 \rangle = \frac{1}{2} a_0^2 n_0^2 B_0^2 \lambda_B \int_{-\infty}^{\infty} dz f^2(\vec{x}) \quad (3.39)$$

has to be used. As shown before B_0 (e.g. by Eq. (3.17)), and λ_B (e.g. by Eq. (3.18)) can be derived for a given window function $f(\vec{x})$ using $C_{RM}^{\text{obs}}(\vec{r}_\perp)$. For a good choice of the window function, one gets

$$\chi_{\text{av}}^2 = \frac{1}{A_\Omega} \int dx_\perp^2 \chi^2(\vec{x}_\perp) \approx 1, \quad (3.40)$$

and larger values if the true and assumed models differ significantly. The model discriminating power lies also in the spatial distribution $\chi^2(x_\perp)$, and not only in its global average. If some large scale trends are apparent, e.g. that $\chi^2(x_\perp)$ is systematically higher in more central or more peripheral regions of the Faraday screen, then such a model for $f(\vec{x})$ should be disfavoured. This can be tested by averaging $\chi^2(x_\perp)$, e.g. in radial bins for a roughly spherical screen, as a relaxed galaxy cluster should be, and checking for apparent trends.

This method of model testing can be regarded as a refined Laing-Garrington effect (Laing 1988; Garrington et al. 1988): The more distant radio cocoon of a radio galaxy in a galaxy cluster is usually more depolarised than the nearer radio cocoon due to the statistically larger Faraday depth. This is observed whenever the observational resolution is not able to resolve the RM structures. Here, it is assumed that the observational resolution is sufficient to resolve the RM structures, so that a different depth of some part of the radio source observed, or a different average magnetic energy profile leads to a different statistical Faraday depth $\langle RM(\vec{x}_\perp)^2 \rangle$. Since this can be tested by suitable statistics, e.g. the simple χ^2 statistic proposed here, incorrect models can be identified.

It may be hard in an individual case to disentangle the effect of changing the total depth z_s of the used polarised radio source if it is embedded in the Faraday screen, and from the effect of changing B_0^{obs} , since these two parameters can be quite degenerate. However, there may be situations in which the geometry is sufficiently constrained because of additional knowledge of the source position, or statistical arguments can be used if a sufficiently large sample of similar systems were observed.

The isotropy which is an important assumption for the proposed analysis can be assessed by the inspection of the Fourier transformed RM maps. The assumption of isotropy is valid in the case of a spherically symmetric distribution of $|R\hat{M}(k)|^2$.

Observational artefacts might also influence the shape of the RM autocorrelation function and thus, the magnetic power spectrum. These artefacts are related to beam

smearing, to unavoidable observational noise and RM steps due to the $n\pi$ -ambiguity explained in Sect. 1.2.4. These artefacts are described in more detail in the following.

Beam Smearing: The finite size l_{beam} of a synthesised beam of a radio interferometer should smear out RM structures below the beam size, and therefore can lead to a smooth behaviour of the measured RM autocorrelation function at the origin, even if the true autocorrelation function has a cusp there. Substantial changes of the RM on the scale of the beam can lead to beam depolarisation, due to the differentially rotated polarisation vectors within the beam area (Conway & Strom 1985; Laing 1988; Garrington et al. 1988). Since beam depolarisation is in principle detectable by its frequency dependence, the presence of sub-beam structure can be noticed, even if not resolved (Tribble 1991; Melrose & Macquart 1998). The magnetic power spectrum derived from a beam smeared RM map should cut-off at large $k \sim \pi/l_{\text{beam}}$.

Noise: Instrumental noise can be correlated on several scales, since radio interferometers sample the sky in Fourier space, where each antenna pair baseline measures a different k_{\perp} -vector. It is difficult to understand to which extent noise on a telescope antenna baseline pair will produce correlated noise in the RM map, since several independent polarisation maps at different frequencies are combined in the map making process. Therefore only the case of spatially uncorrelated noise is discussed, as it may result from a pixel-by-pixel RM fitting routine. This adds to the RM autocorrelation function

$$C_{\text{noise}}^{\text{obs}}(\vec{x}_{\perp}, \vec{r}_{\perp}) = \sigma_{RM, \text{noise}}^2(\vec{x}_{\perp}) \delta^2(\vec{r}_{\perp}). \quad (3.41)$$

In Fourier space, this leads to a constant error for $\hat{w}(k)$

$$\hat{w}_{\text{noise}}(k) = 2 \langle \sigma_{RM, \text{noise}}^2 \rangle \quad (3.42)$$

and therefore to an artificial component in the magnetic power spectrum $\varepsilon_B^{\text{obs}}(k)$ increasing by k^2 .

If it turns out that for an RM map with an inhomogeneous noise map (if provided by an RM map construction software) the noise affects the small-scale power spectrum too severely, one can try to reduce this by down-weighting noisy regions with a suitable choice of the data weighting function $h(\vec{x}_{\perp})$ which was introduced in Sect. 3.3.1 for this purpose.

RM steps due to the $n\pi$ -ambiguity: An RM map is often derived by fitting the wavelength-square behaviour of the measured polarisation angles. Since the polarisation angle is only determined up to an ambiguity of $n\pi$ (where n is an integer), there is the risk of getting a fitted RM value which is off by $m \Delta RM$ from the true one, where m is an integer, and $\Delta RM = \pi (\lambda_{\text{min}}^2 - \lambda_{\text{max}}^2)^{-1}$ is a constant depending on the used wavelength range from λ_{min} to λ_{max} .

This can lead to artificial jumps in RM maps, which will affect the RM autocorrelation function and therefore any derived magnetic power spectrum. In order to get an idea of its influences, the possible error by an additional component in the derived RM map can be modelled by

$$RM^{\text{amb}}(\vec{x}_{\perp}) = \sum_i m_i \Delta RM \vec{1}_{\{\vec{x}_{\perp} \in \Omega_i\}}, \quad (3.43)$$

where Ω_i is the area of the i -th RM patch, and m_i is an integer, mostly +1 or -1. Assuming that different patches are uncorrelated, the measured RM autocorrelation

function is changed by an additional component, which should be asymptotically for small r_\perp

$$C_{RM}^{\text{amb}}(r_\perp) = \Delta RM^2 \eta_{\text{amb}} \left(1 - \frac{r_\perp}{l_{\text{amb}}}\right), \quad (3.44)$$

where η_{amb} is the area filling factor of the ambiguity patches in the RM map, and l_{amb} a typical patch diameter. Thus, the artificial power induced by the $n\pi$ -ambiguity mimics a turbulence energy spectrum with slope $s = 1$, which would have equal power on all scales. A steep magnetic power spectrum can therefore possibly be masked by such artefacts.

Fortunately, for a given observation the value of ΔRM is known and one can search an RM map for the occurrence of steps by ΔRM over a short distance (not necessarily one pixel) in order to detect such artefacts.

3.3.4 Assessing the Influence of the Window Function

A completely different problem is the assessment of the influence of the window function on the shape of the magnetic power spectrum and thus, on the measured magnetic energy spectrum. As stated above, the introduction of a finite window function has the effect to smear out the power spectrum and Eq. (3.26) becomes

$$\hat{C}_\perp^{\text{exp}}(\vec{k}_\perp) = \frac{1}{2} \int d^3q \hat{w}(q) \frac{q_\perp^2}{q^2} \frac{|\hat{f}(\vec{k}_\perp - \vec{q})|^2}{(2\pi)^3 V_{[f]}}. \quad (3.45)$$

The term $q_\perp^2/q^2 \leq 1$ in the expression above states some loss of magnetic power. Without this term, the expression would describe the redistribution of magnetic power within Fourier space, where in this case the magnetic energy would be conserved.

However, the expression can be employed as an estimator of the response of the observation to the magnetic power on a given scale p by setting $\hat{w}(q) = \delta(q - p)$ in the above equation. For an approximate treatment of a realistic window and a spherical data average, one can derive

$$\hat{w}_p^{\text{exp}}(k_\perp) = \frac{2p}{\pi} \int_{|k_\perp - q|}^{k_\perp + q} dq \frac{q \int_0^{2\pi} d\phi W_\perp(q(\cos \phi, \sin \phi))}{\sqrt{4q^2 p^2 - (q^2 + p^2 - k_\perp^2)^2}}. \quad (3.46)$$

Here the projected Fourier window was introduced

$$W_\perp(\vec{k}_\perp) = \frac{|\hat{f}_\perp(\vec{k}_\perp)|^2}{(2\pi)^2 A_{[f_\perp]}}, \quad (3.47)$$

where $A_{[f_\perp]} = \int d^2x_\perp f_\perp^2(\vec{x}_\perp)$ while defining the projected window function as $f_\perp(\vec{x}_\perp) = \int dz f^2(\vec{x}) V_{[f]}/A_\Omega$.

One can also require for the input power spectrum a field strength by setting $\hat{w}(q) = 2\pi^2 (B^2/p^2) \delta(q - p)$ in Eq. (3.45). The resulting power spectrum can be treated as an observed power spectrum and thus, a magnetic field strength B_{exp} can be derived by integration following Eq. (3.29). The comparison of B and B_{exp} for the different p -scales yields a further estimate for reliable ranges in k -space.

So far the response power spectrum was derived for an underlying magnetic spectrum located only on scales p . One could also add the particular response functions

such that the actual observed power spectrum $\hat{w}^{\text{obs}}(k)$ would be matched. Typical power spectra, e.g. for turbulence, show a power law behaviour over several orders of magnitude. Therefore, one would choose to weight the different response functions $\hat{w}_p^{\text{exp}}(k_\perp)$ derived using Eq. (3.46) by a power law while integrating over them

$$\hat{w}^{\text{exp}}(k) = w_0 \int_{p_{\min}}^{p_{\max}} dp \hat{w}_p^{\text{exp}}(k_\perp) \left(\frac{p}{k_0}\right)^{-\alpha-2}, \quad (3.48)$$

where w_0 represents a normalisation constant, k_0 a typical k -space length scale and p_{\min} and p_{\max} are upper and lower cutoffs for the integration over the response functions. Ideally, one would choose the normalisation constant $w_0 = c_0 B_0^2/k_0^3$, where c_0 is chosen such that $\int dk^3 \hat{w}^{\text{exp}}(k) = B_0^2$. One would vary the spectral index α of the power law, B_0 or w_0 and the lower cutoff of the integration p_{\min} in order to match the two functions, $\hat{w}^{\text{obs}}(k)$ and $\hat{w}^{\text{exp}}(k)$.

One has direct access to the average magnetic energy density ε_B by integrating Eq. (3.48) which results in the analytic expression

$$\varepsilon_B = \frac{w_0 k_0^3}{2(2\pi)^3 (\alpha - 1)} \left[\left(\frac{p_{\min}}{k_0}\right)^{1-\alpha} - \left(\frac{p_{\max}}{k_0}\right)^{1-\alpha} \right]. \quad (3.49)$$

Following the definition of the magnetic autocorrelation length λ_B (Eq. (3.33)), one can derive an expression for this length using the parameters determined in the analysis above

$$\lambda_B = \pi \frac{\alpha - 1}{\alpha} \frac{p_{\min}^{-\alpha} - p_{\max}^{-\alpha}}{p_{\min}^{1-\alpha} - p_{\max}^{1-\alpha}}. \quad (3.50)$$

In the calculation of the expected response $\hat{C}_\perp^{\text{exp}}(\vec{k}_\perp)$ and thus, $\hat{w}^{\text{exp}}(\vec{k}_\perp)$ to an underlying magnetic power spectrum $\hat{w}(k)$ seen through some window $W(\vec{k})$ as expressed by Eq. (3.46), it has not been considered that the mean RM is subtracted from the observed RM maps before the analysis is applied to them in order to remove contributions from foreground RM screens (e.g. our Galaxy). This is taken into account by noting that the RM value of a pixel at \vec{x}_\perp in the map will be changed only in the case of $\vec{x}_\perp \in \Omega$, which can be written as

$$RM(\vec{x}_\perp) \rightarrow RM^*(\vec{x}_\perp) = RM(\vec{x}_\perp) - \mathbb{1}_{\{\vec{x}_\perp \in \Omega\}} \int \frac{d^2 x'_\perp}{A_\Omega} RM(\vec{x}'_\perp). \quad (3.51)$$

Using the properties of the Fourier transform of a function with compact support, one can show that

$$\hat{C}_{RM^*}^{\text{exp}}(\vec{k}_\perp) = \hat{C}_{RM}^{\text{exp}}(\vec{k}_\perp) - \hat{C}_{RM}^{\text{exp}}(\vec{0}_\perp) |\Delta_\Omega(\vec{k}_\perp)|^2, \quad (3.52)$$

where

$$\Delta_\Omega(\vec{k}_\perp) = \frac{1}{A_\Omega} \int d^2 x_\perp \mathbb{1}_{\{\vec{x}_\perp \in \Omega\}} e^{i\vec{k}_\perp \cdot \vec{x}_\perp}, \quad (3.53)$$

and $\hat{C}_{RM}^{\text{exp}}(\vec{k}_\perp)$ is the expected, uncorrected response to $\hat{w}(k)$. The linearity of the problem ensures that this correction is valid for any input power spectra $\hat{w}(k)$ (as long as $\hat{C}_{RM}^{\text{exp}}(\vec{k}_\perp)$ is calculated from it) which could be a delta-function, a power law, or

could have any other shape. Similarly, one can write for the spherically averaged expected observed power spectrum

$$\hat{w}_*^{\text{exp}}(k) = \hat{w}^{\text{exp}}(k) - \hat{w}^{\text{exp}}(0) \frac{1}{2\pi} \int_0^{2\pi} d\phi |\Delta_\Omega(k(\cos \phi, \sin \phi))|^2, \quad (3.54)$$

where $\hat{w}^{\text{exp}}(k)$ is given by Eq. (3.46).

The subtraction of the mean RM does not only remove unwanted homogeneous foregrounds, it also ensures that $\hat{w}_*^{\text{exp}}(k)$ (or $\hat{C}_{RM*}^{\text{exp}}(\vec{k}_\perp)$) vanishes at the origin $\hat{w}_*^{\text{exp}}(0) = 0$ (similarly $\hat{C}_{RM*}^{\text{exp}}(\vec{0}_\perp) = 0$). For a correct behaviour of the responses at low k this correction is therefore crucial and will be taken into account in the following.

3.4 Application to Existing Rotation Measure Maps of Galaxy Clusters

Before the analysis was applied to the data any mean RM value was subtracted from the RM maps. This is necessary as mentioned above, since statistically isotropic fields are assumed and therefore, any RM foreground which would affect this analysis has to be removed. Furthermore, very noisy pixels and pixel areas exhibiting huge differences in the RM values on scales smaller than the beamsize were removed from the data to decrease the possible influences of observational artefacts.

The origin of the z -axis was placed in the cluster centre and was used as reference point \vec{x}_{ref} for the global distribution of electron density and magnetic energy. The latter was assumed to scale with the electron density such that $\langle \vec{B}^2(\vec{x}) \rangle^{1/2} / B_0 = (n_e(\vec{x}) / n_{e0})^{\alpha_B}$. Unless stated otherwise, the parameter α_B was chosen to be unity. For the electron density distribution a standard β -profile¹ was used.

3.4.1 3C75, 3C465 & Hydra A - the Data

The radio source 3C465 (or NGC 7720) is located in the Abell cluster 2634 of richness class I. The redshift of the object is 0.0302 (Wegner et al. 1999). A detailed X-ray study of this cluster was performed by Schindler & Prieto (1997) using ROSAT PSPC data. They derive for the density profile a core radius of 4.9 arcmin, a β of 0.79 and an electron density at the cluster centre of $n_{e0} = 0.0012 \text{ cm}^{-3}$. Their analysis revealed indications of a weak cooling flow in the cluster centre. The scenario of a weak cooling flow in Abell 2634 is also supported by White (2000) who analysed ASCA X-ray data.

The radio galaxy 3C75 which is in the centre of Abell 400 also of richness class I has a redshift of 0.02315 (de Vaucouleurs et al. 1991). The X-ray properties of the cluster have been studied by Reiprich & Böhringer (2002) using ROSAT PSPC data. They determine for the gas density profile a core radius of 3.9 arcmin, a β of 0.54 and an electron density at the cluster centre of $n_{e0} = 0.0016 \text{ cm}^{-3}$. There are no indications of a cooling flow in Abell 400 (White 2000).

The details of the radio data reduction of the RM maps for the two sources above can be found in Eilek & Owen (2002). The typical RM values observed for them ranging between -250 rad m^{-2} and 250 rad m^{-2} . The beamsize for the map of 3C75

¹defined as $n_e(r) = n_{e0}(1 + (r/r_c)^2)^{-\frac{3}{2}\beta}$, where r_c is called the core radius.

(Abell 400) is 3 arcsec which translates into 1.4 kpc and for 3C465 (Abell 2634) the beamsize is 3.8 arcsec which is equivalent to 2.3 kpc for the cosmology chosen. Furthermore, for both clusters it was assumed that the source plane is parallel to the observer plane since no indication for the Laing-Garrington effect was found.

Hydra A (or 3C218) is an extended extragalactic radio source located at a redshift of 0.0538 (de Vaucouleurs et al. 1991) in the cluster Abell 780 of richness class 0. However, hereafter it is referred to as Hydra A cluster. Detailed X-ray studies have been performed on it (e.g. Ikebe et al. 1997; Peres et al. 1998; David et al. 2001). For the derivation of the electron density profile parameter, the work by Mohr et al. (1999) done for ROSAT PSPC data was used while employing the deprojection of X-ray surface brightness profiles as described in the Appendix A of Pfrommer & Enßlin (2004). Since Hydra A is known to exhibit a strong cooling flow as observed in the X-ray studies, a double β -profile² is assumed and for the inner profile the following parameter were used $n_{e1}(0) = 0.056 \text{ cm}^{-3}$ and $r_{c1} = 0.53 \text{ arcmin}$, for the outer profile $n_{e2}(0) = 0.0063 \text{ cm}^{-3}$ and $r_{c2} = 2.7 \text{ arcmin}$ and a $\beta = 0.77$ was applied.

The details of the radio data reduction can be found in Taylor & Perley (1993) and the RM map is shown in Fig. 1.2. The beamsize of the map is 0.3 arcsec translating into 0.3 kpc. The source consists of two lobes, a northern and a southern one. Typical RM values in the north lobe are in the range between -1000 rad m^{-2} and $+3300 \text{ rad m}^{-2}$ whereas in the south lobe also values of down to $-12000 \text{ rad m}^{-2}$ were observed.

The analysis was concentrated on the north lobe of this source because the signal-to-noise ratio in the data of the south lobe does not seem sufficient enough for our purposes. Furthermore, the application of the data filter to remove big steps between data pixels leads to a splitting of the RM data in the south lobe into a lot of small spatially disconnected areas. Such a fragmented window function can heavily obscure any power spectrum measured.

For Hydra A, there is a clear depolarisation asymmetry of the two lobes observed as described by the Laing-Garrington effect. Taking this effect into account and following the analysis of Taylor & Perley (1993), first the coordinate system is rotated about an angle of 110 degrees such that the x -axis was parallel to the jet axis. Afterwards the source plane was rotated about the new y -axis by an inclination angle θ of 45 degree such that the north lobe would point towards the observer.

3.4.2 Real Space Analysis

After the mean RM subtraction and the noisy pixel filtering, the RM autocorrelation function $C_{RM}(r_{\perp})$ was determined using Eq. (3.4) choosing the described normalisation scheme. The resulting correlation function for Abell 2634, Abell 400 and Hydra A are exhibited in Fig. 3.1, where the correlation function of Hydra A was divided by 100 for better display. The integration of these functions employing Eq. (3.19) leads to the information on the RM correlation length λ_{RM} which was determined to be 7.9 kpc for Abell 2634, 5.3 kpc for Abell 400, and 1.9 kpc for Hydra A.

The determination of the magnetic autocorrelation function in real space $w(r)$ achieved by the deprojection of the RM autocorrelation is numerically difficult due to the term in the denominator $\sqrt{y^2 - r^2}$ of Eq. (3.15) and Eq. (3.16) which represents

²defined as $n_e(r) = [n_{e1}^2(0)(1 + (r/r_{c1})^2)^{-3\beta} + n_{e2}^2(0)(1 + (r/r_{c2})^2)^{-3\beta}]^{1/2}$.

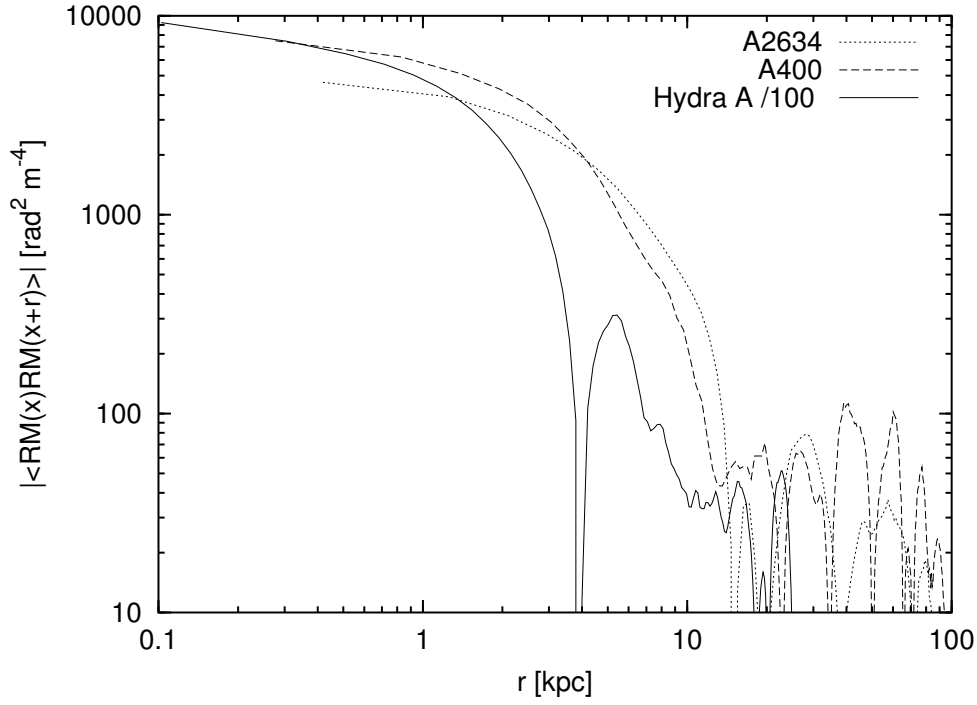


Figure 3.1: RM autocorrelation function $|C_{RM}(r_{\perp})|$ of Abell 400, Abell 2634 and Hydra A obtained using Eq. (3.4). Note that the correlation function for Hydra A was divided by 100 for representing purposes.

an integrable singularity and can in principle be avoided by a well selected coordinate transformation.

However, the numerical calculation, especially the determination of the value for $r = 0$ of the magnetic autocorrelation function $w(r)$ is difficult because an extrapolation to $r = 0$ of the function $w(r)$ being itself subject to extrapolation and data binning is involved. Therefore, the determination of the point $w(r = 0)$ is not accurate and one should be careful with the interpretation of the values derived by this method. The behaviour of the magnetic autocorrelation around $r = 0$ is exhibited in Fig. 3.2 for the case of Abell 2634, where the magnetic field autocorrelation functions $w(r)$ derived by employing various methods are shown. One can see that the steeper the initial slope of the function the less precise it becomes to determine $w(r = 0)$ since slight deviations in the slope can lead to very different results.

One should keep this in mind when calculating the value of the magnetic field autocorrelation length λ_B which was determined to be 6.0 kpc for Abell 2634, 3.9 kpc for Abell 400 and 1.4 kpc for Hydra A using Eq. (3.18), where for the value of $w(r = 0) = B_0^2$ the extrapolation of Eq. (3.15) to $r = 0$ was used. Thus, the field strengths were determined to be of about $4 \mu\text{G}$ for Abell 2634, of about $9 \mu\text{G}$ for Abell 400 and of about $12 \mu\text{G}$ for Hydra A in the real space analysis.

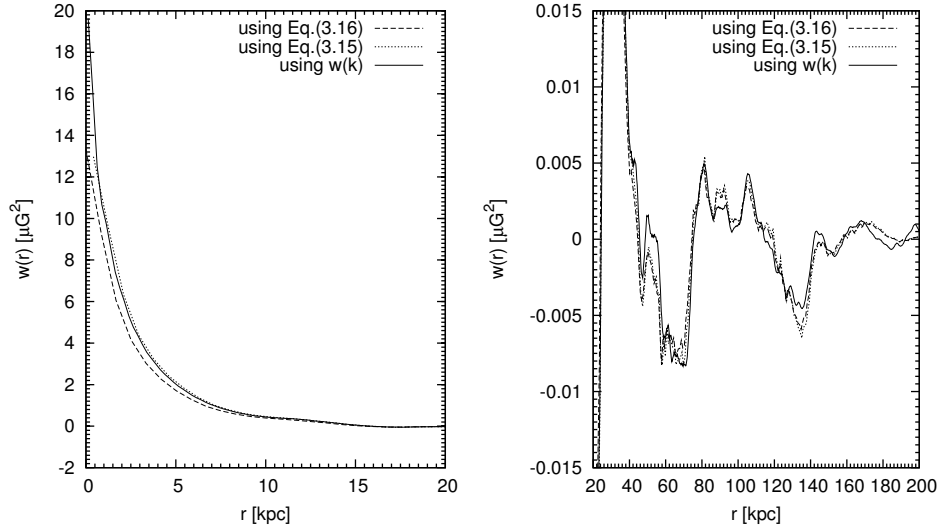


Figure 3.2: The magnetic autocorrelation function $w(r)$ for Abell 2634 calculated using Eq. (3.15), (3.16) and (3.35). One can clearly see that the value of $w(r = 0)$ can deviate by a factor of two but for larger r all methods yield almost the same results.

3.4.3 Fourier Space Analysis

For the calculations in Fourier space a 2-dimensional Fast Fourier Transform (FFT) algorithm was employed while setting all blanked values in the original RM map to zero. The RM autocorrelation function $\hat{C}_\perp(k_\perp)$ was then obtained by summing over rings in k -space. Since the magnetic field autocorrelation function $\hat{w}(k)$ is related to the RM autocorrelation function in Fourier space simply by multiplying the RM correlation function $\hat{C}_\perp(k_\perp)$ by two (Eq. (3.26)), there is no numerical difficulty involved deriving this function and thus, the results for the magnetic field quantities are more precise than those obtained applying the real space analysis.

The integration of the power spectrum $\hat{w}^{\text{obs}}(k)$ following Eq. (3.34) and Eq. (3.33) yields the correlation lengths. Thus, the RM autocorrelation length λ_{RM} was calculated to be 8.0 kpc for Abell 2634, 5.3 kpc for Abell 400 and 2.0 for Hydra A. The magnetic field correlation length λ_B was determined to be 4.0 kpc for Abell 2634, 2.3 kpc for Abell 400 and 0.5 kpc for Hydra A in the Fourier analysis.

No numerical problem is involved in the determination of the value of the magnetic autocorrelation function $w(r)$ for $r = 0$ if one uses Eq. (3.35) resulting in magnetic field strengths of about $5 \mu\text{G}$ for Abell 2634, of about $11 \mu\text{G}$ for Abell 400 and of about $23 \mu\text{G}$ for Hydra A.

The application of Eq. (3.35) to the data translates the magnetic autocorrelation function in Fourier space to real space. The comparison of the so derived function with the deprojected functions $w(r)$ in real space is exhibited in Fig. 3.2 for the case of Abell 2634. One can clearly see that at the origin there are deviations by a factor of two due to the uncertainties connected to the extrapolation used in the real space approach. At higher separations r all three functions shown do not differ significantly from each other. It is remarkable that except at the origin all three independent approaches are in such good agreement which demonstrates reliable numerics.

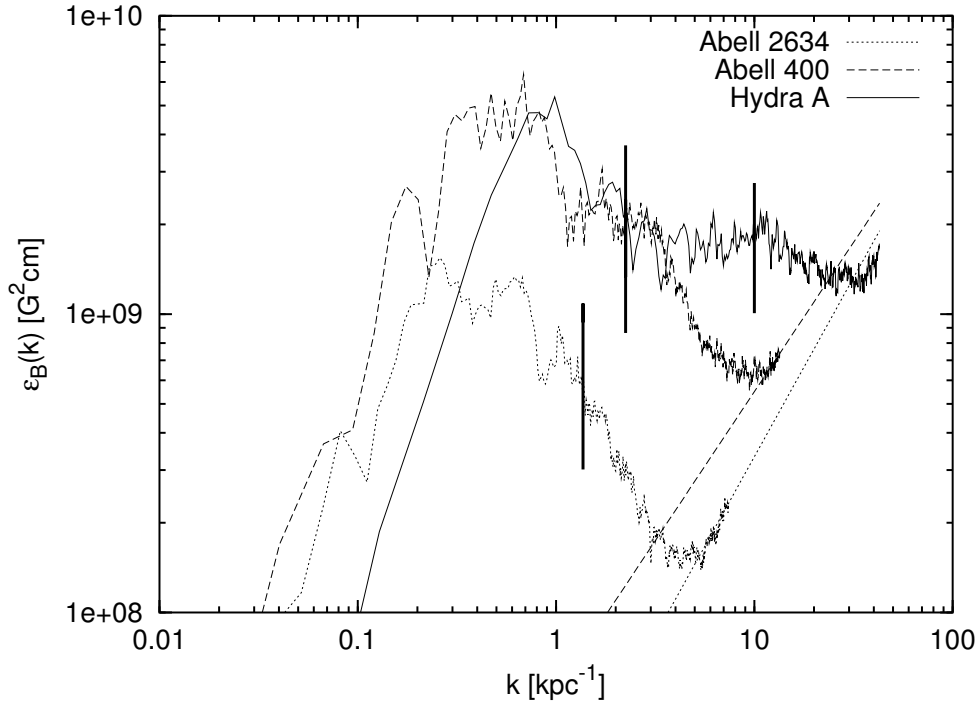


Figure 3.3: Magnetic energy spectrum $\varepsilon_B^{\text{obs}}(k)$ derived for Abell 400, Abell 2634 and Hydra A. The Fourier transformed beamsizes ($k_{\text{beam}} = \pi/l_{\text{beam}}$) are represented by the thick vertical lines. The other straight lines describe the slope (dashed line represents $\varepsilon_B \propto k$ and the dotted represents $\varepsilon_B \propto k^{1.2}$) of the increase in the energy density for the largest k .

The knowledge of the 3-dimensional power spectrum $\hat{w}(k)$ also allows calculating the magnetic energy spectrum $\varepsilon_B^{\text{obs}}(k)$ by employing equation (3.29). The results for the three clusters are shown in Fig. 3.3. The magnetic energy spectra are suppressed at small k by the limited window size and the subtraction of the mean RM (small k in Fourier space translate into large r in real space). A response analysis as suggested above is performed in Sect. 3.4.4 in order to understand this influence in more detail.

Another feature of these energy spectra is the increasing energy density at the largest k -vectors in Fourier space and thus, small r in real space. They can be explained by noise on small scales.

It seems reasonable to introduce an upper cutoff for the integration of the magnetic energy spectra in Eq. (3.29). In Fig. 3.3, the equivalent beamsize in Fourier space $k_{\text{beam}} = \pi/l_{\text{beam}}$ (where l_{beam} is the beamsize in real space defined as FWHM) is represented by a vertical line for each cluster which is 1.4 kpc^{-1} for Abell 2634, 2.2 kpc^{-1} for Abell 400 and 10.0 kpc^{-1} for Hydra A. One can clearly see that the noise induced increase of the energy density lies on k -scales beyond k_{beam} . Therefore, a suitable upper cutoff for any integration of the magnetic energy spectrum seems to be k_{beam} .

The influence of the upper k -cutoff in the integration can be seen in Fig. 3.4 which

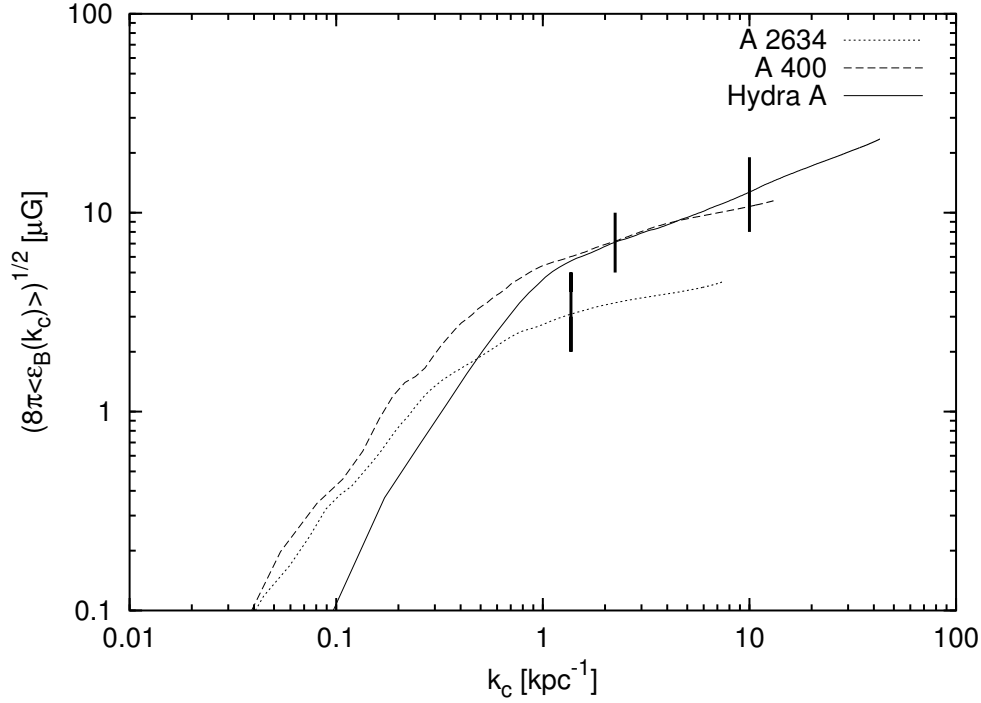


Figure 3.4: Magnetic field strength B dependent on the upper k -cutoff in the integration of Eq. (3.29). The equivalent beamsizes k_{beam} are represented as vertical lines.

displays the magnetic field strength $B = \sqrt{8\pi\langle\varepsilon_B\rangle}$ estimated from

$$\varepsilon_B(k < k_c) = \int_0^{k_c} dk \varepsilon_B(k). \quad (3.55)$$

3.4.4 Test the model and assess the influence of the window function

The various possibilities to test the window function and to assess its influences on the results outlined in Sects. 3.3.3 and 3.3.4 were also applied to the data. The χ^2 -function was derived by radially averaging the $\chi^2(\vec{x}_\perp)$ distribution resulting from Eq. (3.38), where for the magnetic autocorrelation length λ_B the value derived in the Fourier analysis was used since this approach seems to be more accurate. The resulting radially binned distributions are shown in Fig. 3.5 determined for the three clusters. There is no apparent spatial large scale trend visible for Abell 400 and Abell 2634 which indicates a reasonable model for the window function. In the case of Hydra A, there appears to be a trend of higher values for $\chi^2(x_\perp)$ towards larger r , comparable to small scale trends seen in the $\chi^2(x_\perp)$ distribution of Abell 2634 and Abell 400.

Furthermore, the $\chi^2(\vec{x}_\perp)$ distribution was integrated following Eq. (3.40) and χ_{av}^2 was calculated to be 1.0 for Abell 2634, 1.2 for Abell 400 and 1.6 for Hydra A. A refinement of the model describing parameter does not seem to be required for Abell 2634 and Abell 400.

Since the value for χ_{av}^2 of 1.6 for Hydra A is deviating from 1, the geometry of the source was varied, i.e. the inclination angle θ between source and observer plane was

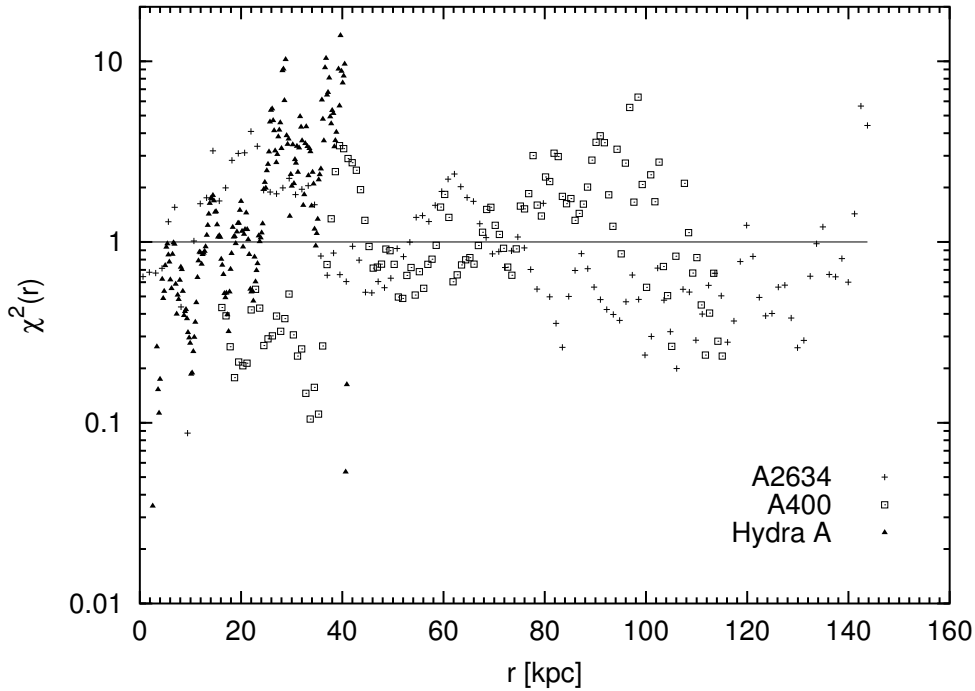


Figure 3.5: Testing the window function by calculating the $\chi^2(x_\perp)$ distribution for all three clusters.

varied from 30 degree up to 60 degree resulting in field strength ranging from $17 \mu\text{G}$ to $33 \mu\text{G}$ and values for χ_{av}^2 of 1.4 to 1.8, respectively. These values were derived by integrating over the full accessible unrestricted (without cutoffs) k -space.

Furthermore, the scaling parameter α_B in the scaling relation of the electron density to the magnetic energy density was varied. A value for α_B of 0.5 is still in the limit of reasonable values (see Sect. 1.3.2). Furthermore, such a scaling parameter of $\alpha_B = 0.5$ means that the magnetic energy $\varepsilon_B(x) \propto n_e(\vec{x})$ and thus, the magnetic field would be proportional to the thermal energy of the cluster gas assuming approximately isothermal conditions. However, in this case ($\alpha_B = 0.5$), one obtains for χ_{av}^2 a value of 1.2 and the magnetic field strength is reduced to $17 \mu\text{G}$ by integrating over the full accessible k -space.

One can not be sure that the cause of the trend in the $\chi^2(x_\perp)$ distribution is due to a geometry other than assumed because it could also be explained by a fluctuation similar to the one seen in the $\chi^2(x_\perp)$ distributions of Abell 2634 and Abell 400. There is no reason to change the initial assumption for the geometry of Hydra A. However, one should keep in mind that the central field strength given could be slightly overestimated for Hydra A but it is not clear to what extent if at all.

A good test for the validity of the isotropy assumption is the inspection of the Fourier transformed RM data $|\hat{RM}(k)|^2$ as shown in Fig. 3.6 for Abell 400 and Hydra A. The FFT data look similar for Abell 2634. In this figure half of the Fourier plane is shown since the other half is symmetric to the one exhibited. No apparent anisotropy is present in this figure.

It was mentioned already that the magnetic energy spectrum $\varepsilon_B^{\text{obs}}(k)$ in Fig. 3.3 is

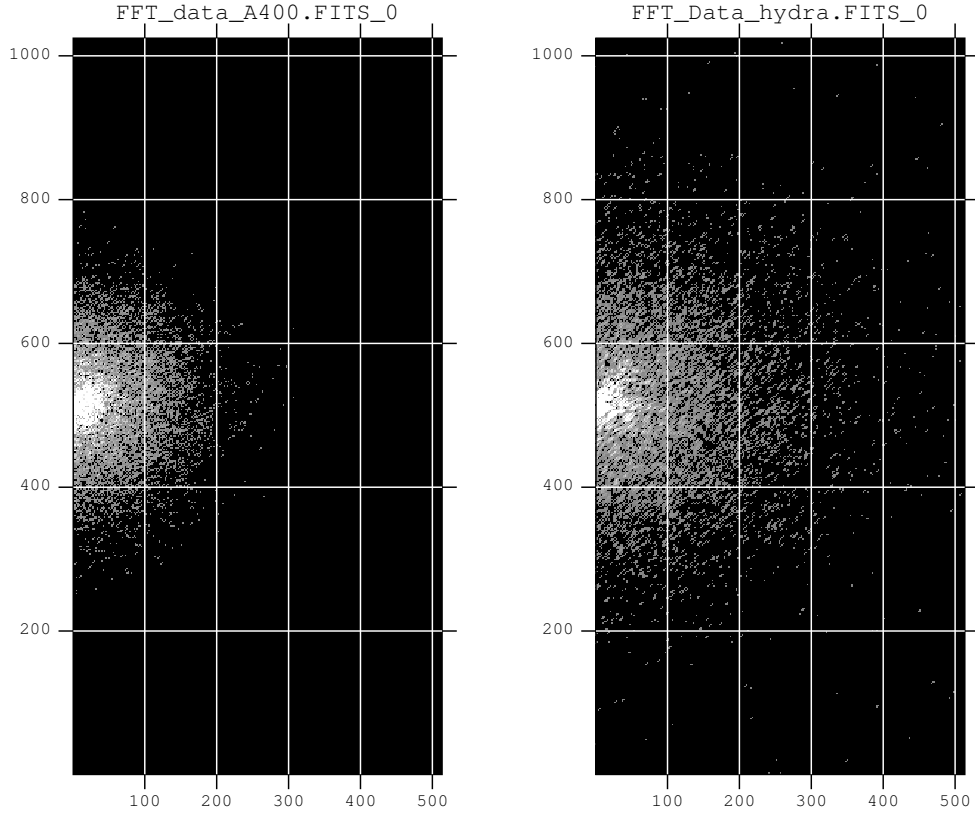


Figure 3.6: The power $|\langle \hat{RM}(k) \rangle|^2$ of the Fourier transformed RM map of Abell 400 on the left side and Hydra A on the right side. The image for Abell 2634 looks similar. Only half of the Fourier plane is exhibited the other half is point symmetric to the one shown

suppressed by the limited window size for small k -vectors in Fourier space. Therefore, a response analysis is necessary in order to understand the influence of the window on the shape of the magnetic energy spectrum. For this purpose, the projected window function was Fourier transformed by employing a FFT algorithm and inserted into Eq. (3.46). Then the response functions $\hat{w}^{\text{exp}}(k)$ obtained were compared to the observed power spectrum $\hat{w}^{\text{obs}}(k)$ as shown in Fig. 3.7 for the case of Abell 2634, where for the normalisation a magnetic field strength B of $5 \mu\text{G}$ was chosen. The corresponding figures look very similar for Abell 400 and Hydra A.

From Fig. 3.7, one can clearly see that the response to delta function like input power spectra on small p scales in Fourier space (i.e. large r in real space) is a smeared out function as one would expect. The response for larger p becomes more strongly peaked suggesting that at k -scales larger than 0.3 kpc^{-1} for Abell 2634 the influence of the window function becomes negligible. From similar plots for the other two clusters under consideration, scales of about 0.4 kpc^{-1} for Abell 400 and 1.0 kpc^{-1} for Hydra A are found. Thus, one would use this value as a lower cutoff k_{min} for the determination of the magnetic field strength.

From the response power spectra $\hat{w}_p(k_{\perp})$ calculated for different p requiring a

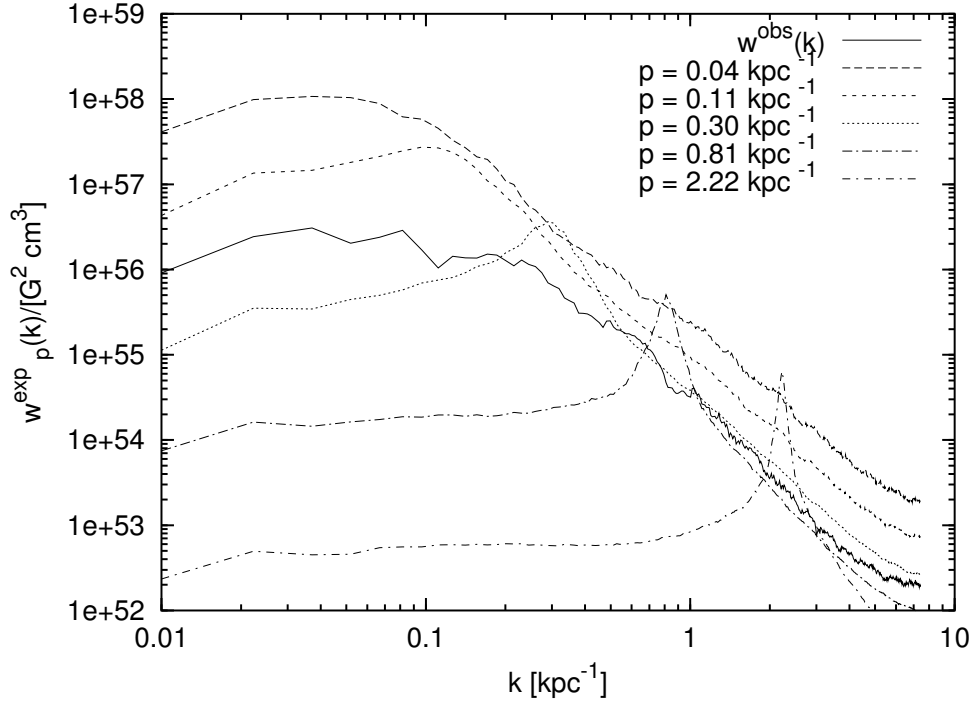


Figure 3.7: Responses at various scales p to the window function of Abell 2634 assuming a $B = 5\mu\text{G}$ in comparison to the observed magnetic autocorrelation function $\hat{w}(k)$.

magnetic field strength B , one can derive a magnetic field strength B_{exp} by integration. In Fig. 3.8, the comparison between these two field strengths is plotted for the different p -scales. It can be seen that for the smallest p 's the deviation between expected field strength and actual observed one is significantly but for larger p they are almost equal suggesting that on these scales the influence of the window is negligible. Taking Fig. 3.8 into account, the values determined above as lower cutoff k_{min} can be confirmed.

Another possibility to assess the influence of the window on the power spectra is to match the added response functions and the actual observed power spectra $\hat{w}^{\text{obs}}(k)$. This was done by applying Eq. (3.48) to a set of response functions generated for closely spaced p -scales. The resulting function $\hat{w}^{\text{exp}}(k)$ was matched to the actual observed power spectrum $\hat{w}^{\text{obs}}(k)$ for each of the three clusters by varying B_0 , the spectral index α of the power law in Eq. (3.48) to match the slope of the functions and p_{min} as lower cutoff to fit the function at its turnover for small k -scales. The resulting functions are shown in Fig. 3.9 in comparison to the respective observed power spectra. The shape of the power spectra was matched for Abell 2634 for a spectral index of $\alpha = 1.6$, for Abell 400 for an $\alpha = 1.8$ and for Hydra A for an $\alpha = 2.0$ whereas a lower k -cutoff of 0.09 kpc^{-1} was used for Abell 2634, 0.08 kpc^{-1} for Abell 400 and 0.3 kpc^{-1} for Hydra A.

The spectral index α can also be used to plot the respective power law as represented by the straight lines in Fig. 3.9. The slopes of these lines clearly deviate

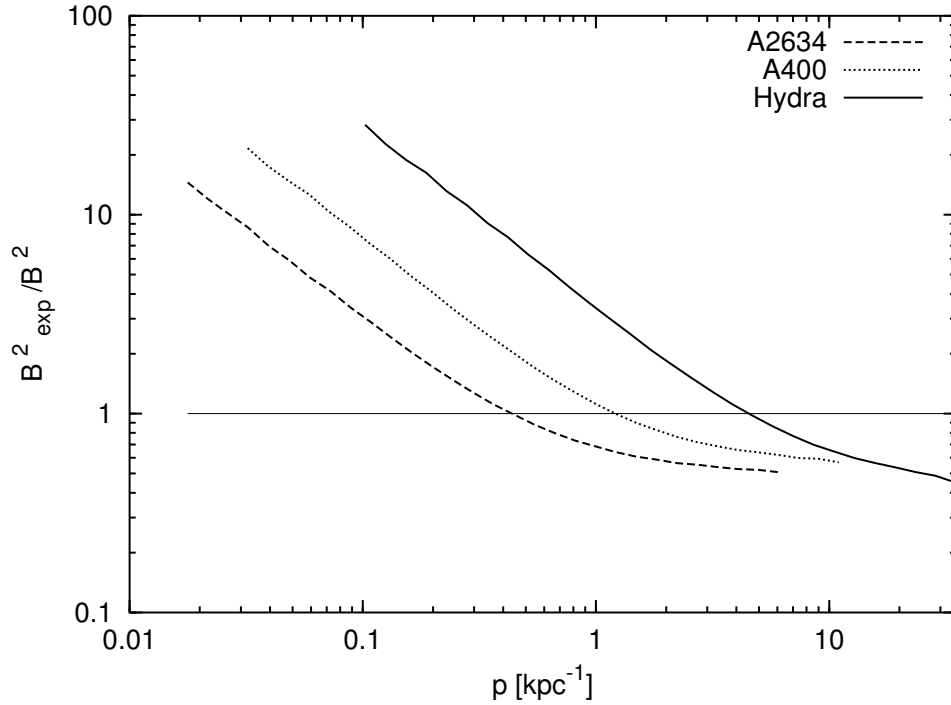


Figure 3.8: Comparison between the expected magnetic field strength B to the measured one B_{exp} for the particular p -scales for the three clusters.

from the respective observed power spectra suggesting that one cannot estimate differential parameters like spectral indices directly from Fourier transformed RM maps. More sophisticated approaches should be developed. However, the approach allows to exclude flatter spectral slopes than $\alpha = 1.3$ still leaving a Kolmogorov spectrum ($\alpha = 5/3$) as a possible description. For attempts to measure the magnetic power spectrum from cluster simulations and radio maps see Dolag et al. (2002) and Govoni et al. (2002) respectively³.

3.5 Results

A summary of the values for RM autocorrelation length λ_{RM} , magnetic field autocorrelation length λ_B and the central magnetic field strength B_0 for the magnetised cluster gas in Abell 2634, Abell 400 and Hydra A, derived in Fourier space and real space is given in Tab. 3.1. The RM autocorrelation length λ_{RM} determined in both spaces is almost equal which demonstrates reliable numerics. Furthermore, it is found that the RM autocorrelation length λ_{RM} is larger than the magnetic autocorrelation length λ_B . The deviation of the magnetic field quantities between both spaces is caused by the numerically complicated deprojection of the magnetic autocorrelation function $w(r)$ in real space. Thus, the results in Fourier space are more reliable and should be considered for any interpretation and discussion.

³The conventions describing the spectra may differ in these articles from the one used here.

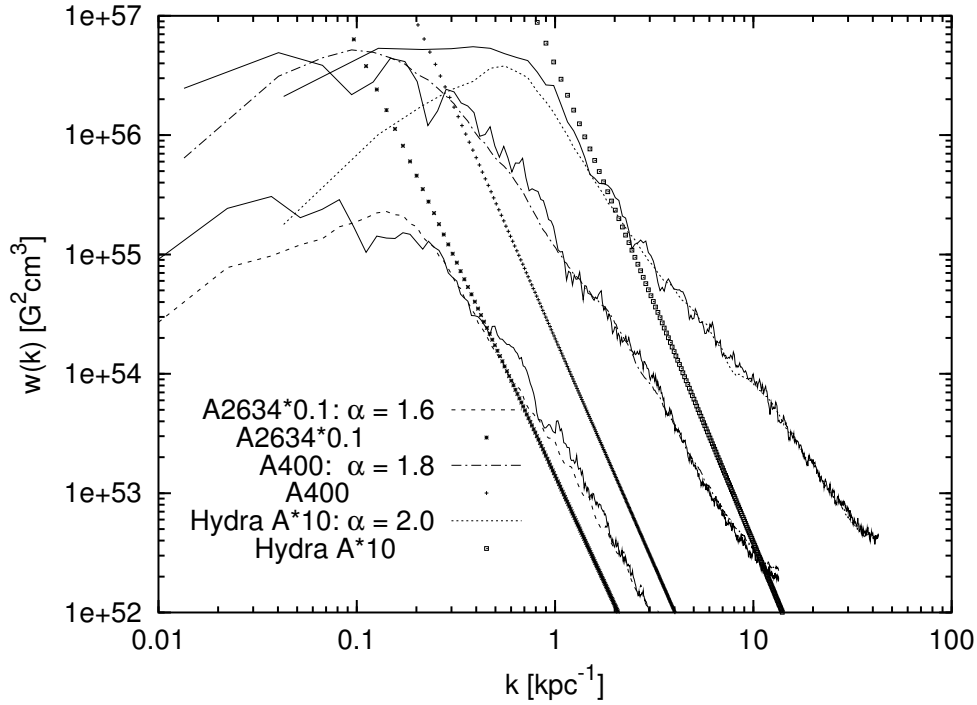


Figure 3.9: Closely p -spaced response functions were integrated by employing Eq. (3.48) and the resulting $\hat{w}^{\text{exp}}(k)$ are exhibited in comparison to the observed power spectrum $\hat{w}^{\text{obs}}(k)$ shown as solid lines. The spectral index α used for Abell 2634 is 1.6, for Abell 400 is 1.8 and for Hydra A is 2.0. The straight lines represent the power law assuming the spectral index determined from the response analysis. Note that the data for Abell 2634 are multiplied by 0.1 and the data for Hydra A by 10 for representing purposes.

In Sect. 3.4.4, many possible influences on the power spectra were discussed. It was verified that for intermediate k -ranges extending over at least one order of magnitude the power spectra are not governed by the window or the resolution of the RM maps and thus, represent most likely the magnetic field properties of the cluster gas. Thus, one can derive field quantities such as magnetic field strength B_0 and autocorrelation length λ_B from this intermediate k -range.

The suitable cutoffs for the integration of the power spectra in order to derive the magnetic field strength and autocorrelation length were determined in Sec. 3.4.4. Using for Abell 2634 a lower cutoff k_{min} of 0.3 kpc^{-1} and an upper cutoff of 1.4 kpc^{-1} results in a magnetic field strength of $3 \mu\text{G}$. Integrating the power spectrum of Abell 400 in the range from 0.4 kpc^{-1} to 2.2 kpc^{-1} yields a field strength of $6 \mu\text{G}$. The same was done for the Hydra A cluster in the range from 1 kpc^{-1} to 10 kpc^{-1} which resulted in a field strength of $13 \mu\text{G}$. The determination of the magnetic field autocorrelation length λ_B by integration over the power spectra in limited k -space yields 4.9 kpc for Abell 2634, 3.6 kpc for Abell 400 and 0.9 kpc for Hydra A.

In the course of the response analysis in order to estimate the influence of the window on the power spectra, the integrated response power spectra $\hat{w}^{\text{exp}}(k)$ was matched

cluster	α_B	Real Space			non-restricted Fourier Space		
		λ_{RM} [kpc]	λ_B [kpc]	B_0 [μ G]	λ_{RM} [kpc]	λ_B [kpc]	B_0 [μ G]
Abell 400	1.0	5.2	3.9	8	5.3	2.3	12
Abell 2634	1.0	7.9	6.0	4	8.0	4.0	5
Hydra A	1.0	1.9	1.4	13	2.0	0.5	23
Abell 400	0.5	5.2	3.9	7	5.3	2.3	10
Abell 2634	0.5	7.9	6.0	3	8.0	4.0	4
Hydra A	0.5	1.9	1.4	10	2.0	0.5	17
cluster	α_B	restricted Fourier Space					
		λ_B [kpc]	B_0 [μ G]				
Abell 400	1.0	3.6	6				
Abell 2634	1.0	4.9	3				
Hydra A	1.0	0.9	13				
Abell 400	0.5	3.4	6				
Abell 2634	0.5	4.9	3				
Hydra A	0.5	0.9	18				

Table 3.1: Values for the autocorrelation length scales λ_B and λ_{RM} and the magnetic field strength B_0 at the cluster centre obtained in real space analysis, in Fourier space analysis and in restricted Fourier Space analysis are given for the different clusters under consideration. The values are calculated for two different scaling parameters α_B . Note that for position other than the cluster centre the average magnetic energy is given by $\langle \vec{B}^2(\vec{x}) \rangle^{1/2} = B_0 (n_e(\vec{x})/n_{e0})^{\alpha_B}$.

with the actual 3-dimensional observed power spectra $\hat{w}^{\text{obs}}(k)$ and the spectral index α , c_0 and the lower cutoff p_{\min} in Eq. (3.48) were determined. Using these values for the parameters in Eq. (3.49), the direct integration in the limits of p_{\min} and $p_{\max} = k_{\text{beam}}$ of the power spectra obtained by the response analysis results in magnetic field strengths of about 3 μ G for Abell 2634, of about 6 μ G for Abell 400 and of about 11 μ G for Hydra A. These field strengths are in good agreement with the results obtained by the restricted Fourier space integration of the observed 3-dimensional power spectra.

However, the values for λ_B were determined for the same p_{\min} and $p_{\max} = k_{\text{beam}}$ applying Eq. (3.50). The resulting value is 13 kpc for Abell 2634, 17 kpc for Abell 400 and 4 kpc for Hydra A. They deviate by a factor of 4 to 5 from the magnetic field autocorrelation length λ_B determined from the restricted Fourier space integration. The reason for this behaviour could be found in the sensitivity to the lower cutoff p_{\min} and the power law index α . It was already mentioned that the method might not be suitable at that stage to determine differential parameters such as a power law index α . A more detailed discussion is necessary in order to understand this behaviour.

However, the values of the magnetic field strength B_0 for Abell 400 and Abell 2634 of about 6 μ G and 3 μ G, respectively, are larger compared to the initial analysis performed by Eilek & Owen (2002) for the case of a magnetic sheet with a thickness of 10-20 kpc. They discuss a variety of magnetic field models and it is referred to Tab. 2 of their paper for detailed numbers and description.

For the Hydra A cluster, Taylor & Perley (1993) conclude in their analysis that

there is a random magnetic field component of about $30 \mu\text{G}$ with a correlation length of 4 kpc. The deviation by a factor of 3 of the field strength from the value revealed by the presented analysis might be explained by the usage of an improved electron density profile for the analysis which also takes the cooling flow into account. The value for the central magnetic field strength B_0 might also be lower due to the conservative approach of restricting the k -space integration range. Another explanation for the difference could be sought in the exclusion of the south lobe from the calculation above. Including the south lobe in the analysis leads to higher central field strengths but given the influence of the very complicated window function in the case of the south lobe, it is not clear to what extent the real power spectrum is resembled.

The estimation of the dynamical importance of the magnetic fields derived for the cluster gas can be done by comparing the thermal pressure ($p_{th} = 2n_e(0)kT_{core}$) with the magnetic pressure ($p_B = B_0^2/(8\pi)$). One can calculate p_B/p_{th} which yields 0.08 for the case of Abell 2634 (assuming a $T_{core} = 1.2 \text{ keV}$ (Schindler & Prieto 1997)), $p_B/p_{th} = 0.19$ for Abell 400 ($T_{core} = 1.5 \text{ keV}$ (Eilek & Owen 2002)) and $p_B/p_{th} = 0.01$ for Hydra A ($T_{core} = 2.7 \text{ keV}$ (David et al. 2001)). It is astonishing that the value of p_B/p_{th} is smaller for Hydra A, which is a cooling flow cluster, than for the non-cooling flow cluster Abell 400 and Abell 2634. The values of $p_B/p_{th} = 0.1...0.2$ for the latter two clusters give an indication that for those clusters the magnetic field is of some weak dynamical importance for the cluster gas.

3.6 Conclusions

A new analysis of Faraday rotation maps was developed in order to estimate magnetic field strength and autocorrelation length and to determine the magnetic power spectra of the magnetised intra-cluster gas. This analysis relies on the assumption that the magnetic fields are statistically isotropically distributed throughout the Faraday screen. A window function was introduced through which any virtually statistically homogeneous magnetic field can be thought to be observed. This window function describes the geometry of the source and the global properties of the intra-cluster gas such as the electron density, known from X-ray measurements, and the global average magnetic field distribution, which is assumed to scale with the electron density. Furthermore, two possible approaches in real and Fourier space were developed and tests were outlined for the evaluation of any influence especially arising from the observational nature of the data such as limited source size, resolution and pixel noise on the results obtained. However, the analysis allows to measure average magnetic energies but it is not sensitive to the particular realisation of the magnetic field structure.

This approach was applied to observational data and reliable results were derived not only for magnetic field strengths and autocorrelation lengths but also strength and quality of any results obtained by applying this new analysis to any observational data was assessed. In order to understand the possible impacts on the results, the Faraday rotation maps of three extragalactic extended radio sources were reanalysed, i.e. 3C75 in the cluster Abell 400, 3C465 in Abell 2634, which were kindly provided by Frazer Owen and Jean Eilek, and Hydra A in Abell 780, which was kindly provided by Greg Taylor. The analysis was performed in real and Fourier space for these three Faraday rotation maps. While discussing the difficulties involved in the application to the data,

it was realised that the calculations in Fourier space are more reliable.

The isotropy assumption was tested for and no indication of anisotropy was found. Furthermore a χ^2 -test was performed in order to assess the model adopted for the geometry of the sampling volume incorporating the global electron density and the average magnetic energy distribution. In the case of Abell 2634 and Abell 400, no indication was found that the model used may be incorrect. However, in the case of Hydra A indications were found that the window function needs refinement but the indications were not strong enough in order to enforce this refinement.

It was realised that the magnetic energy spectra $\varepsilon_B(k)$ of the three clusters investigated are dominated on the largest k -scales (i.e. smallest r -scales) by noise. Therefore, it seemed natural to introduce a higher k -cutoff k_{\max} for any integration in k -space necessary to derive magnetic field quantities such as field strength and autocorrelation length. Being conservative, as a higher k -cutoff the equivalent beamsize in Fourier space $k_{\max} = \pi/l_{beam}$ was used which is equal to 1.4 kpc^{-1} for Abell 2634, 2.2 kpc^{-1} for Abell 400 and 10 kpc^{-1} for Hydra A. This will have the effect of losing some power which is redistributed due to the window from smaller to these larger k -scales.

On the smallest k -scales, i.e. the largest r -scales, power is suppressed because of the limited size of the window. For the assessment of the influence of this suppression on the power spectra, a response analysis as described in Sec. 3.3.3 was applied to the observational windows. The response of the window to delta like input power spectra on small p -scales is a wide, smeared out function whereas the response on larger p -scales is a peaked function. This observation motivated the introduction of a lower k -cutoff k_{\min} in any integration in k -space. This value was determined to be 0.3 kpc^{-1} for Abell 2634, 0.4 kpc^{-1} for Abell 400 and 1.0 kpc^{-1} for Hydra A. However, the magnetic field strengths derived are not sensitive to this lower cutoff due to the small k power suppression.

It was verified that the intermediate k -ranges between k_{\min} and k_{\max} extending over at least one order of magnitude can be used to determine actual magnetic field properties of the intra-cluster gas.

Integrating over the response power spectra on particular p -scales enables to match the so determined power spectra and the actually observed power spectra in order to have an independent estimate for magnetic field strengths and spectral slopes. For the three clusters under consideration, spectral indices α for the slopes of the power spectra were determined to be in the range from 1.6 to 2.0. Therefore it would be possible that the magnetic field in these clusters have a Kolmogorov power spectrum exhibiting $\alpha = 5/3$. However at present, one can not exclude steeper spectra but flatter spectra exhibiting slopes smaller than $\alpha = 1.3$ would have been recognised by the analysis. Although, it was realised that this analysis is not suitable for the determination of differential parameters such as the spectral slopes of power spectra directly from Fourier transformed RM maps, the determination of integrated quantities such as the magnetic field strength appears feasible.

Taking all these arguments into account values for the RM autocorrelation length λ_{RM} , the magnetic field autocorrelation length λ_B and the central average magnetic field strength B_0 were determined by integration of the magnetic energy spectrum in the limits between k_{\min} and k_{\max} . An overview of these numbers is given in Tab. 3.1 where these values are compared to those derived in real space and non-restricted

Fourier space.

The magnetic field autocorrelation length λ_B was determined for the restricted Fourier space integration to be 4.9 kpc for Abell 2634, 3.6 kpc for Abell 400 and 0.9 kpc for Hydra A. In comparison with the RM autocorrelation length λ_{RM} calculated to be 8.0 kpc for Abell 2634, 5.3 kpc for Abell 400 and 2.0 kpc for Hydra A, it can be said that these two characteristic length scales differ from those often assumed in previous work.

The magnetic field strength in the cluster centre B_0 was calculated for the same limited k -space and was determined to be 3 μG for Abell 2634, 6 μG for Abell 400 and 13 μG for Hydra A. Given the assumption of isotropy and a scaling parameter $\alpha_B = 1.0$, these are conservative values. The resulting magnetic pressures suggest some small but non negligible pressure support for a dynamical influence in the case of Abell 2634 and Abell 400 since the value of p_B/p_{th} is 0.08 and 0.19, respectively.

However, the approach so far is not able to separate the influence of noise on the maps from the astrophysically interesting signal of intra-cluster magnetic fields. Investigations aiming to detect (see Chapter 2) and to minimise such spurious signals are presented in the next Chapter 4.

Chapter 4

Pacman - A new RM Map Making Algorithm

The statistical analysis of RM measurements in terms of correlation functions and equivalently power spectra requires that the RM 's are unambiguously determined as discussed in the last chapter. Thus, any ambiguous RM can lead to misinterpretation of the data investigated. This ambiguity results from the observational fact that the polarisation angles are only determined up to additions of $\pm n\pi$. In this chapter, a new map making algorithm - called *Pacman* - is described. Instead of solving the $n\pi$ -ambiguity for each data point independently, the proposed algorithm solves the $n\pi$ -ambiguity for a high signal-to-noise region and uses this information to assist computations in adjacent low signal-to-noise areas.

This work is submitted to *Mon. Not. Roy. Astron. Soc.* as two papers (Dolag et al. 2004; Vogt et al. 2004). My part in this work was the contribution to the development of the algorithm, the data handling, the statistical characterisation and tests of the various RM maps and describing the algorithm in the two scientific publications. *Pacman* was implemented by Klaus Dolag.

4.1 Introduction

For the calculation of rotation measures (RM) and intrinsic polarisation angles (φ^0) using the relationship $\varphi = RM \lambda^2 + \varphi^0$ (see Eq. (1.42)), a least squares fit is normally applied to the polarisation angle data. Since the measured polarisation angle φ is constrained only to values between 0 and π leaving the freedom of additions of $\pm n\pi$, where n is an integer, the determination of RM and φ^0 is ambiguous, causing the so called $n\pi$ -ambiguity. Therefore, a least squares fit has to be applied to all possible $n\pi$ -combinations of the polarisation angle data at each data point of the polarised radio source while searching for the $n\pi$ -combination for which χ^2 is minimal.

In principle, χ^2 can be decreased to infinitely small numbers by increasing RM substantially. Vallée & Kronberg (1975) and Haves (1975) suggested to avoid this problem by introducing an artificial upper limit for $|RM| \leq RM_{\max}$. Since this is a biased approach, Ruzmaikin & Sokoloff (1979) proposed to assume that no $n\pi$ -ambiguity exists between the measurements of two closely spaced wavelengths taken from a whole wavelength data set. The standard error of the polarisation measurements

is then used to constrain the possible $n\pi$ -combinations for the least squares fit for the subsequent observed frequencies. To these methods is referred as the “standard fit” algorithms, as they are currently the most widely used methods. However, these methods might still give multiple acceptable solutions for data with low signal-to-noise, requiring the solution to be flagged and all the information carried by these data is lost. Furthermore, it still can happen that the algorithm chooses a wrong RM and imprints spurious artefacts on the RM and the φ^0 maps.

Recently, a completely different approach was proposed by Sarala & Jain (2001) which takes the circular nature of the polarisation angle into account. The authors apply a maximum likelihood method to spectral polarisation data. Although this approach is not biased towards any RM value, it is rather designed for a large number of observed wavelengths. Similarly, de Bruyn (1996) and Brentjens & de Bruyn (2004) propose an RM -synthesis via wide-band low-frequency polarimetry. However, typically the observations are only performed at three or four wavelengths especially for extended (diffuse) radio sources.

For a new approach for the unambiguous determination of RM and φ^0 , it is assumed that if regions exhibit small polarisation angle gradients between neighbouring pixels in all observed frequencies simultaneously, then these pixels can be considered as connected. Note, that the gradient is calculated modulo π , which implies that polarisation angles of 0 and π are regarded as having the same orientation and thus, the cyclic nature of polarisation angles is reflected. Information about one pixel can be used for neighbouring ones and especially the solution to the $n\pi$ -ambiguity should be the same.

In cases of small gradients, assuming continuity in polarisation angles allows to assign an absolute polarisation angle for each pixel with respect to a reference pixel within each observed frequency. This assignment process has to be done for each spatially independent patch of polarisation data separately, such as each side of a double-lobed radio source. The reference pixel is defined to have a unique absolute polarisation angle and the algorithm will start from this pixel to assign absolute polarisation angles with respect to the reference pixel while going from one pixel to its neighbours. Figuratively, the algorithm eats its way through the set of available data pixel. It might become clear now why the algorithm was named *Pacman*¹ (Polarisation Angle Correcting rotation Measure ANALysis).

Pacman reduces the number of least squares fits in order to solve for the $n\pi$ -ambiguity. Preferably, the reference point is chosen to have a high signal-to-noise ratio so that in many areas, it is sufficient to solve the $n\pi$ -ambiguity only for a small number of neighbouring pixels simultaneously and to use this solution for all spatially connected pixels. Pixels with low signal-to-noise will profit from their neighbouring pixels allowing a reliable determination of the RM and φ^0 .

Faraday rotation measure maps are analysed in order to get insight into the properties of the RM producing magnetic fields such as field strengths and correlation lengths. Artefacts in RM maps which result from $n\pi$ -ambiguities can lead to misinterpretation of the data. In Chapter 3, a method was proposed to calculate magnetic power spectra from RM maps and to estimate magnetic field properties. It was realised

¹The computer code for *Pacman* is publicly available at <http://dipastro.pd.astro.it/~cosmo/Pacman>

that map making artefacts and small scale pixel noise have a noticeable influence on the shape of the magnetic power spectra on large Fourier scales – small real space scales. Thus, for the application of these kind of statistical methods it is desirable to produce unambiguous RM maps with as little noise as possible. This and similar applications are motivations for designing *Pacman* and to quantify its performance.

In order to detect and to estimate the correlated noise level in RM and φ^0 maps, a gradient vector product statistic V was proposed in Chapter 2. It compares RM gradients and intrinsic polarisation angle gradients and aims to detect correlated fluctuations on small scales, since RM and φ^0 are both derived from the same set of polarisation angle maps.

In Sect. 4.2, the idea and the implementation of the *Pacman* algorithm is described in detail. In Sect. 4.3, *Pacman* is tested on artificially generated RM maps and its ability to solve the $n\pi$ -ambiguity properly is demonstrated.

In Sect. 4.5, this algorithm is applied to polarisation observation data sets of two extended polarised radio sources located in the Abell 2255 (Govoni et al. 2002) cluster and the Hydra cluster (Taylor & Perley 1993). Using these polarisation data, the stability of the *Pacman* algorithm is demonstrated and the resulting RM maps are compared to RM maps obtained by a standard fit algorithm.

The importance of the unambiguous determination of RM 's for a statistical analysis is demonstrated by applying the statistical approach developed in Chapter 3 to the RM maps in order to derive the power spectra and strength of the magnetic fields in the intra-cluster medium. The influence of error treatment in the analysis is also discussed. The philosophy of this statistical analysis and the calculation of the power spectra is briefly outlined in Sect. 4.4.3 whereas the results of the application to the RM maps are presented in Sect. 4.5.

In addition, the *gradient vector product statistic* V is applied as proposed in Chapter 2 in order to detect map making artefacts and correlated noise. The concept of this statistic is briefly explained in Sect. 4.4.1 and in Sect. 4.5, it is applied to the data. After the discussion of the results, the conclusions and lessons learned from the data during the course of this work are given in Sect. 4.6.

Throughout the rest of the chapter, a Hubble constant of $H_0 = 70 \text{ km s}^{-1} \text{ Mpc}^{-1}$, $\Omega_m = 0.3$ and $\Omega_\Lambda = 0.7$ in a flat universe is assumed.

4.2 The new *Pacman* algorithm

4.2.1 The Idea

As described in the introduction, the Faraday rotation measure RM_{ij} at each point with map pixel coordinate (ij) of the source, is usually calculated by applying a least squares fit to measured polarisation angles $\varphi_{ij}(k)$ observed at frequency $k \in 1 \dots f$ such that

$$\varphi_{ij}(k) = RM_{ij} \lambda_k^2 + \varphi_{ij}^0, \quad (4.1)$$

where φ_{ij}^0 is the intrinsic polarisation angle at the polarised source.

Since every measured polarisation angle is observationally constrained only to a value between 0 and π , one has to replace $\varphi_{ij}(k)$ in the equation above by $\tilde{\varphi}_{ij}(k) = \varphi_{ij}(k) \pm n_{ij}(k) \pi$, where $n_{ij}(k)$ is an integer, leading to the so called $n\pi$ -ambiguity.

Taking this into account, a least squares fit to calculate RM_{ij} and φ_{ij}^0 at each pixel has to be applied by allowing all possible combinations of $n_{ij}(k)\pi$ while determining the $n_{ij}(k)$ for which the χ_{ij}^2 is minimal. The presence of observational noise might cause a standard least squares fit, as suggested by Vallée & Kronberg (1975), Haves (1975) or Ruzmaikin & Sokoloff (1979), to choose a spurious RM value especially for areas of low signal-to-noise.

The idea of *Pacman* is to reduce the number of pixels for which the $n\pi$ -ambiguity has to be individually solved. This is done by splitting the solution of the $n\pi$ -problem into two problems, a local and a global one,

$$n_{ij}(k) = \tilde{n}_{ij}(k) + n(k), \quad (4.2)$$

where $\tilde{n}_{ij}(k)$ is the local solution, linking polarisation angles of neighbouring pixels within a frequency map, and $n(k)$ is the global solution to the problem, linking polarisation angles of the different frequencies. The local part $\tilde{n}_{ij}(k)$ is determined by construction of absolute polarisation angle maps for each frequency with respect to a high signal-to-noise reference pixel being defined to possess a unique polarisation angle. The term absolute polarisation angle is to be understood as a value determined relative to the reference pixel by adding $\pm n\pi$ to the measured polarisation angles in order to remove jumps of the order of π in the measured polarisation angle map of each observed frequency. The global $n\pi$ ambiguity is solved for a high signal-to-noise area surrounding the reference pixel resulting in $n(k)$. This is then also the solution of the global $n\pi$ -problem for all spatially connected points which are assigned absolute polarisation angles with respect to this reference area.

The splitting of the problem in a local and a global one is possible if the real polarisation angle $\bar{\varphi}_{ij}(k)$ ($\bar{\varphi}_{ij}(k) = RM_{ij} \lambda_k^2 + \varphi_{ij}^0$) is a smooth quantity which does not change more than $\pm\pi/2$ between neighbouring pixels. In Sect. 4.2.2, it is described how *Pacman* ensures that only pixels fulfilling this condition are used.

The source might consist of several spatially independent areas of polarisation, to which hereafter is referred to as patches. The $n\pi$ -ambiguity has to be solved for each of these patches separately, requiring separate reference pixels to be defined for the construction of absolute polarisation angles.

The advantage of *Pacman* is that the global $n\pi$ -ambiguity is solved only for pixels having the highest signal-to-noise ratios. Therefore, noisier pixels which are situated at the margin of the source profit from an already defined global solution $n(k)$ to the $n\pi$ -ambiguity, making a reliable determination of RM_{ij} and the intrinsic polarisation angle φ_{ij}^0 for these pixels possible.

4.2.2 The Basic Algorithm

The algorithm starts with reading the maps of polarisation angles and of its errors, processes them, and when finished, it saves the different calculated maps. A flow chart of the *Pacman* algorithm is exhibited in Fig. 4.1, which shows schematically the procedure the algorithm follows in order to determine the solution to the $n\pi$ -ambiguity and to calculate the various maps.

After loading the various polarisation data for the different frequencies, the algorithm calculates a quality measure map. Different actions are involved in the processing of the data. One of the processes is building a patch which involves the construction

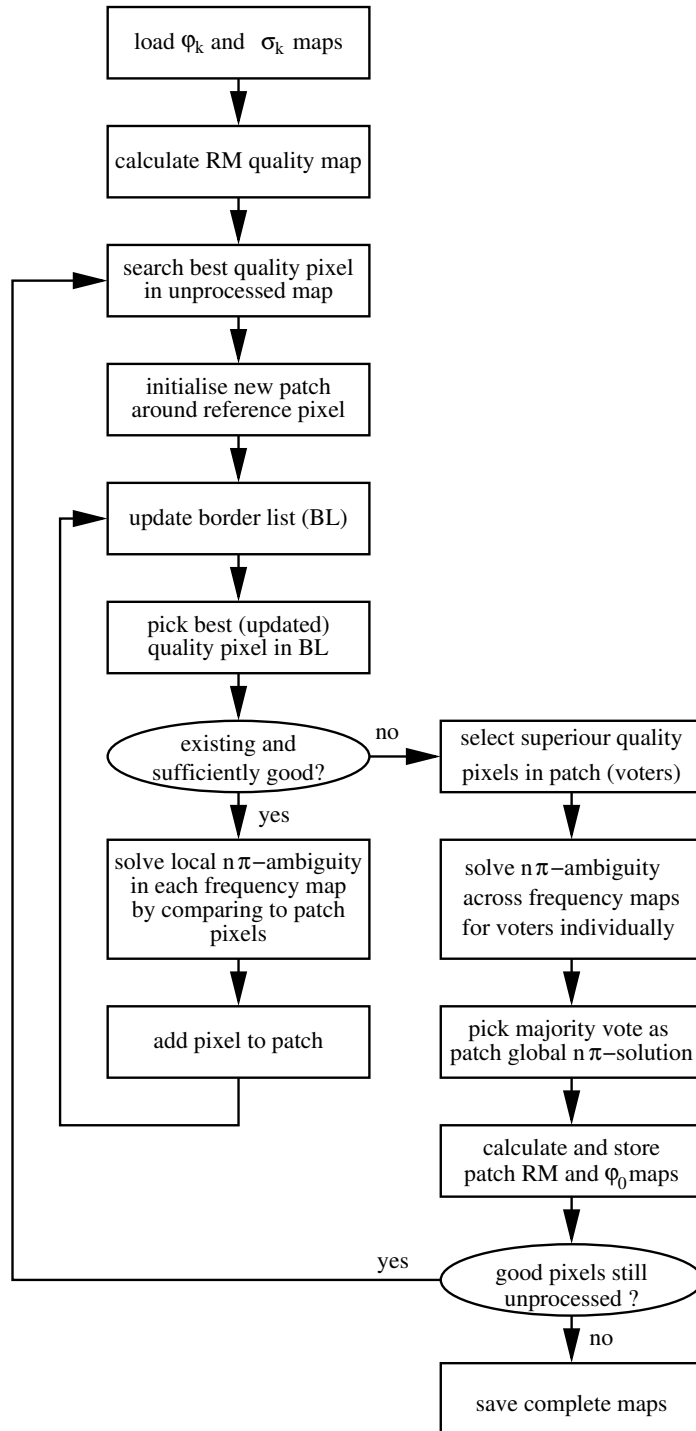


Figure 4.1: A flow chart representing the individual steps involved in the calculation of RM and φ^0 maps as performed by the algorithm *Pacman*.

of absolute polarisation angle maps. First, the reference pixel for a patch of polarisation is determined from the quality measure map. This step is followed by solving the local $n\pi$ -ambiguity in each frequency map for pixels being spatially connected to the defined patch reference pixel and having small gradients in polarisation angle to the neighbouring pixels at all frequencies. This process is mainly governed and stopped by quality requirements.

When the patch building process is stopped then the algorithm solves the global $n\pi$ -ambiguity across the frequency maps individually for a selected set of superior quality pixels (voters) within the patch. The majority of votes is used as the global patch $n\pi$ -solution and the resulting RM and φ^0 values are stored. If there are still unprocessed high quality pixel left, the algorithm starts again to build a new patch. Otherwise *Pacman* finishes and saves the resulting complete maps.

The values for RM and φ^0 are calculated following a weighted least squares fit expressed by

$$RM_{ij} = \frac{\overline{S_{ij}} \overline{\lambda^2 \varphi_{ij}} - \overline{\lambda^2} \overline{\varphi_{ij}}}{\overline{S_{ij}} \overline{\lambda^4} - \overline{\lambda^2}^2} \quad (4.3)$$

$$\varphi_{ij}^0 = \frac{\overline{\varphi_{ij}} \overline{\lambda^4} - \overline{\lambda^2} \overline{\lambda^2 \varphi_{ij}}}{\overline{S_{ij}} \overline{\lambda^4} - \overline{\lambda^2}^2} \quad (4.4)$$

where $\overline{S_{ij}} = \sum_{k=1}^f 1/\sigma_{kij}^2$, $\overline{\varphi_{ij}} = \sum_{k=1}^f \varphi_{ij}(k)/\sigma_{kij}^2$, $\overline{\lambda^2} = \sum_{k=1}^f \lambda_k^2/\sigma_{kij}^2$, $\overline{\lambda^2 \varphi_{ij}} = \sum_{k=1}^f \lambda_k^2 \varphi_{ij}(k)/\sigma_{kij}^2$ and $\overline{\lambda^4} = \sum_{k=1}^f \lambda_k^4/\sigma_{kij}^2$ (see Eq. (1.55) and Eq. (1.56)). In these relations, σ_{kij} is the standard error of the polarisation angle $\varphi_{ij}(k)$ at the pixel coordinate (ij) at the k th wavelength λ_k .

Since the performance of the algorithm is mainly governed by quality requirements, some quality measure is needed in order to rank the map pixels. One good candidate is the expected uncertainty σ_{ij}^{RM} of any RM value obtained in an error weighted least squares fit which is calculated by

$$\sigma_{ij}^{RM} = \sqrt{\frac{\overline{S_{ij}}}{\overline{S_{ij}} \overline{\lambda^4} - \overline{\lambda^2}^2}}, \quad (4.5)$$

where the terms are defined as above.

The uncertainty σ_{ij}^{RM} of the RM value is used to assign each pixel an initial quality $q_{ij} = \sigma_{ij}^{RM}$ since σ_{ij}^{RM} accounts for the statistic used to determine the RM maps. Hence, small values of q_{ij} indicate high quality pixels. The quality is then used to determine the way *Pacman* goes through the data which will be preferably from high to low quality data pixels.

For the construction of absolute polarisation angle maps for each frequency, *Pacman* starts at the best quality pixel having the smallest value q_{ij} , which is defined to be the reference pixel. For this first point, the measured polarisation angle $\varphi_{ij}(k)$ is defined to possess a unique polarisation angle value $\overline{\varphi}_{ij}(k) = \varphi_{ij}(k)$ for each observed frequency. It is important to note that the reference pixel is the same for all frequencies.

Then, *Pacman* compiles what is called the border list (BL). It contains pixels being direct neighbours to points which have been already assigned an absolute polarisation

angle. In the following, the set of adjacent pixels $(i \pm 1, j \pm 1)$ to the pixel (ij) will be referred to as direct neighbours $(i'j')$. Beginning with the direct neighbours of the reference pixels, the border list is continuously updated during the progression of the algorithm. A pixel can be rejected from the border list if the standard error $\sigma_{k_{ij}}$ of the polarisation angle for any frequency at this pixel exceeds a certain limit σ_k^{\max} which is set at the beginning of the calculation. However, this requirement can be relaxed (see Sect. 4.2.7).

Having defined the reference pixel, *Pacman* assigns absolute polarisation angles to pixels within the border list always starting with the pixel having the best quality, i.e. the lowest q_{ij} value. For this pixel, the algorithm solves the local $n\pi$ -ambiguity with respect to $\tilde{n}_{ij}(k) \in \mathbf{Z}$ by minimising the expression

$$\sigma_{ij}^{\Delta} = \sum_{\{i'j'\} \in D_{ij}} [(\varphi_{ij}(k) \pm \tilde{n}_{ij}(k)\pi) - \bar{\varphi}_{i'j'}(k)]^2, \quad (4.6)$$

where D_{ij} is the set of all direct neighbours $(i'j')$ to the pixel (ij) which have already been assigned an absolute polarisation angle. The resulting $\tilde{n}_{ij}(k)$ value determines the absolute polarisation angle $\bar{\varphi}_{ij}(k) = \varphi_{ij}(k) \pm \tilde{n}_{ij}(k)\pi$ which has the smallest difference to the already defined absolute polarisation angles of adjacent pixels $\bar{\varphi}_{i'j'}(k)$. For each pixel, this is done at each frequency $k \in 1 \dots f$ independently but simultaneously. Thus, *Pacman* goes the same way through the data in each frequency. Note that one can introduce a value σ_{\max}^{Δ} which causes *Pacman* to reject the pixel if σ_{ij}^{Δ} exceeds σ_{\max}^{Δ} (see Sect. 4.2.6). Additionally the border list is updated to include direct neighbours to the recently processed pixel (ij) which have not yet been assigned an absolute polarisation angle.

Pacman repeats this process for the best remaining pixel in the border list which has the lowest q_{ij} and so on, until the whole patch consists of spatially connected pixels with assigned absolute polarisation angles and no acceptable neighbouring pixels remain in the border list.

At this stage, *Pacman* solves the global $n\pi$ -ambiguity $n(k)$ by applying a standard least squares fit to a set of best constrained pixels within the patch (i.e. the surrounding area of the reference pixel). *Pacman* solves for each of these best constrained pixels the global $n\pi$ -ambiguity independently by either using the method of Haves (1975); Vallée & Kronberg (1975) or of Ruzmaikin & Sokoloff (1979) minimising the χ^2 for all possible combinations of $n\pi$. It searches then for the solution $n(k)$, which has been derived for the majority of pixels. This democratically determined solution $n(k)$ is used to perform a least squares fit of the other pixels defined within this patch. Note that in an extreme case, only the reference pixel could be used to solve the global $n\pi$ -ambiguity.

If there are still good quality pixels left in the map which were not connected to the first patch of good quality data, the algorithm begins a new patch of absolute polarisation angles, starting again with the best remaining pixel with smallest q_{ij} . A new patch of absolute polarisation angles is constructed. As a result, the source will be divided in a set of spatially independent polarisation patches, and the global $n\pi$ -ambiguity is solved once for each patch separately. A q_{ij}^{thresh} can be introduced to prevent *Pacman* from starting new patches if the pixels remaining have quality values above that threshold value whose value is chosen in the beginning.

4.2.3 Improving Quality

The solution of the local $n\pi$ -ambiguity for pixel (ij) becomes more reliable as more direct neighbours of these pixels have their absolute polarisation angle $\bar{\varphi}_{i'j'}$ defined. This is taken into account by modifying the quality q_{ij} of the pixels added to the border list to

$$1/q_{ij} = 1/\sigma_{ij}^{RM} + \frac{\alpha}{n_{D_{ij}}^\beta} \left(\sum_{i'j' \in D_{ij}} 1/\sigma_{i'j'}^{RM} \right), \quad (4.7)$$

where $n_{D_{ij}}$ is the number of already defined neighbours $(i'j')$, and α and β are free parameters. This ensures that pixels having more already defined neighbours are considered before others although the original data point might have a smaller signal quality, i.e a higher q_{ij} . Values between 0 and 1 for the free parameter β are reasonable and yield good results. An $\alpha = \beta = 1$ was used and it was observed that *Pacman* goes through the acceptable data points of the polarisation patches in a uniform manner.

4.2.4 Restricting Gradients

The algorithm might be faced with a situation where a high quality pixel can be influenced by a very poor quality pixel, for example when the polarised radio source consists of two radio lobes each having a good signal-to-noise ratio which are connected by a bridge containing only low quality pixels. The *Pacman* algorithm would start by defining absolute polarisation angles from one of the two lobes, eventually reaching the bridge of low signal-to-noise and entering the second lobe from there. In such cases, it might happen that within the area of low quality data pixels a distinct determination of absolute polarisation angles by solving the local $n\pi$ -ambiguity using Eq. (4.5) is no longer possible. The entire second lobe would then suffer, and wrong solutions would be introduced.

In order to avoid such situations, the algorithm is restricted to accept in the border list only neighbours which have a lower quality than the one under consideration. This forces the algorithm to go always from high to low quality pixels, leading to an artificial splitting of connected regions in the map into different patches.

However, such a strict rule would lead to heavy fragmentation and is not preferable. Therefore, a parameter g is introduced to relax this strict limitation such that a new pixel is only accepted in the border list when the relation

$$q_{i'j'} > g * q_{ij} \quad (4.8)$$

is fulfilled. This relation is always accounted for when adding a new pixel to the border list. It is found that g between 1.1 and 1.5 is a good choice.

4.2.5 Topological Defects

The algorithm can also be faced with situations which is called hereafter topological defects. These defects can be understood by supposing a ring-like polarised structure for which all polarisation angles point towards the centre of the ring. Starting at any point of the ring to define absolute polarisation angles and following the ring structure, a jump will appear on the border of the first to the last defined absolute polarisation

angles after having performed a full circle. Scheuer et al. (1977) describe this problem which they encountered by their analysis of polarisation data.

In the observational data, topological defects are often more complex structured. The artificial jump introduced will cause difficulties in the solution of the local $n\pi$ -ambiguity because this procedure relies on already defined absolute polarisation angles of neighbouring pixels. When confronted with this situation, the algorithm divides the list of direct neighbours into sublists possessing similar polarisation angles. The sublist containing the most pixels is then used to assign the absolute polarisation angle by solving the local $n\pi$ -ambiguity for the pixel under consideration.

The locations of the polarisation angle steps of topological defects are somewhat artificial since they depend on the actual path of the algorithm through the data. Since the algorithm processes all frequencies simultaneously, the steps of topological defects are at the same positions within all frequency maps, and therefore do not cause any further problems. However, if *Pacman* encounters a jump in the polarisation angle to all possible neighbour sublists in any of the frequencies under consideration, *Pacman* will reject this pixel and this pixel will not be considered for this patch but queued back for consideration for the next patches to be constructed. However, these topological defects are rare events, but it is necessary to take them into account for the solution of the local $n\pi$ -ambiguity.

4.2.6 Spurious Points

The intrinsic polarisation angle distribution might show strong gradients extending over a few pixels. This could lead to situations, where the algorithm can not solve the local $n\pi$ -ambiguity at all frequencies simultaneously. Therefore, *Pacman* refuses to assign an absolute value $\bar{\varphi}_{ij}$ to pixels when Eq. (4.6) yields a value σ_{ij}^{Δ} above a certain threshold σ_{\max}^{Δ} , which can be set at the beginning of the calculation.

The pixels in the regions where this might occur most often have a low signal-to-noise ratio. Such situations always occur at strongly depolarised areas, leading to blanked regions in the *RM* distribution.

4.2.7 Multi-Frequency Fits

The aim of any *RM* derivation algorithm should be to calculate *RM*s for an area as large as possible using as much information as is available. On the other hand, for radio observations the total radio intensity decreases with increasing frequency. This can lead to the problem that the area of acceptable polarisation data at a high frequency is much smaller than at a lower frequency. This is especially true for (diffuse) extended radio sources. Furthermore, the limit of allowed standard errors σ_k^{\max} of the polarisation angle might be exceeded for only one frequency leaving the values for the other frequencies still in the acceptable range.

Pacman can take this into account and performs the *RM* fit by omitting the polarisation angles at frequencies which do not meet the quality requirements. In order to do that, *Pacman* uses the standard errors $\sigma_{k_{ij}}$ of polarisation angles to define independently for each frequency, areas in which the *RM* map is permitted to be produced. An additional parameter $k_{\min} \leq f$ is introduced which describes the minimum number of frequencies allowing the freedom to use any combination of the minimum of

frequencies.

In cases of $k_{\min} < f$, *Pacman* will start to determine the solution to global and local $n\pi$ -ambiguity only for the pixels fulfilling the quality requirements at all f frequencies. After finishing that, the algorithm proceeds to include pixels satisfying the quality criteria in less than f frequencies. For these pixels, the same patch building procedure as described in Sect. 4.2.2 applies with some modification in order to prevent the final maps from heavy fragmentation. The best quality pixel among the remaining pixel is picked but before starting a new patch, *Pacman* tests if the pixel under consideration adjoins a patch which has already been processed before. If the pixel adjoins such a patch, *Pacman* tries to solve the local $n\pi$ -ambiguity following Eq. (4.6) and applies the patch solution of the global $n\pi$ -ambiguity to the pixel. If the pixel is neither adjoined to an already processed patch nor the local $n\pi$ -ambiguity solvable (i.e. σ_{ij}^{Δ} exceeds σ_{\max}^{Δ}) then a new patch is initialised by this pixel.

Another possibility is to force *Pacman* to use certain frequencies in all circumstances. Thus, if the quality requirements are not fulfilled for these particular frequencies, there will be no *RM* value determined for the pixel under consideration. This has the advantage that one can use relatively close frequencies as a basis and then include other frequencies at points when a reliable polarisation signal is detected. The advantage of this technique is discussed in Sect. 4.5.

4.2.8 Additional Information

Apart from the resulting *RM* and φ^0 maps, *Pacman* provides sets of additional information about the data in order to estimate the reliability of the results. A patch map which contains all patches used is one example. Such a map is very useful, especially if one requires a minimal number of pixels in a patch in order to accept any calculated *RM* values from a particular patch. A map which includes rejected and thus flagged pixels, can also be obtained. Probably more important are the final χ^2 - and σ^{RM} -maps which are also provided by *Pacman*. This information allows one to understand the reliability of the *RM* maps obtained and can be used for further evaluation and analysis of the *RM* maps.

4.3 Testing the Algorithm

In order to demonstrate the ability of *Pacman* to solve the $n\pi$ -ambiguity, artificially generated maps were used. To generate them, it is started from a polarisation data set from Abell 2255 (Govoni et al. 2002), which was kindly provided by Federica Govoni. The *RM* and φ_0 maps were calculated from this data set and it was assumed that these two maps consist of exact values. Then polarisation maps were generated at four different frequencies which would exactly result from the *RM* and φ_0 maps. As error maps, Gaussian deviates were generated for each frequency which were multiplied by the original error maps provided by Federica Govoni. The so generated error maps were added to the generated frequency maps in order to provide realistic mock observations.

Pacman and the standard fit algorithm were used to calculate the corresponding 'observed' *RM* and φ_0 maps which then were compared pixel-by-pixel to the initial

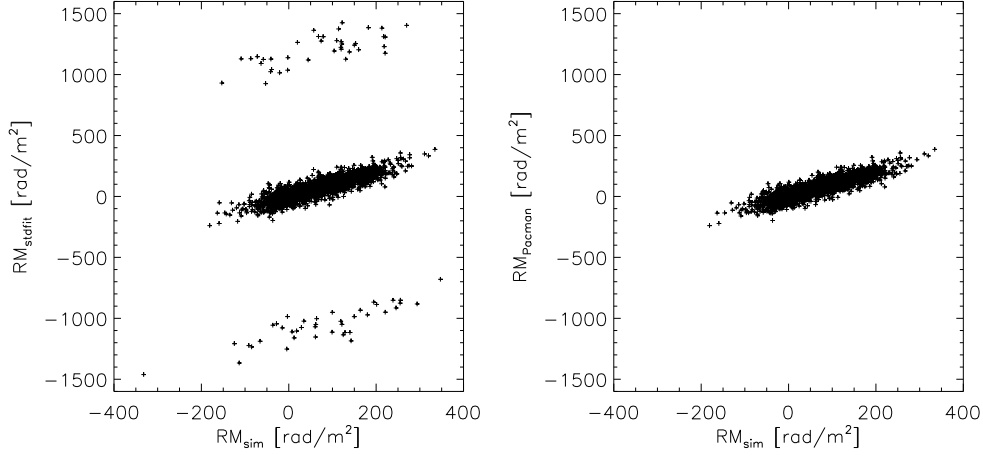


Figure 4.2: Comparison between the simulated RM_{sim} values for an artificially generated set of polarisation angle maps of four frequencies and values derived by *Pacman* RM_{pacman} and the standard fit algorithm RM_{stdfit} . The scatter is due to noise which was added to the polarisation angle maps. Note the wrong solutions of the $n\pi$ -ambiguity results which were calculated by the standard fit indicated by the points around ± 1000 rad m⁻².

exact maps. The result of this comparison is shown in Fig. 4.2. On the right panel, the comparison between the RM_{pacman} values of the *Pacman* map and the values RM_{sim} of the initial map is shown. The scatter in the data is due to the noise which was added to the frequency maps. On the left panel of Fig. 4.2, the pixel by pixel comparison between the values of the standard fit RM_{stdfit} map and the initial RM_{sim} map is shown. Again the scatter is due to the added noise. However, one can clearly see the points at ± 1000 rad m⁻² which deviate from the initial data and are due to the wrongly solved $n\pi$ -ambiguity in the case of the standard fit. Thus, this test demonstrates that the *Pacman* algorithm yields reliable results to the $n\pi$ -ambiguity.

4.4 Statistical Characterisation of Improved RM Maps

4.4.1 Gradient Vector Product Statistic

In Chapter 2, a *gradient vector product statistic* V was introduced to reveal correlated noise in the data. Observed RM and φ^0 maps will always have some correlated fluctuations on small scales, since they are both calculated from the same set of polarisation angle maps, leading to correlated fluctuation in both maps. The noise correlation between φ^0 and RM errors is an anti-correlation of linear shape and can be detected by comparing the gradients of these quantities. A suitable quantity to detect correlated noise between φ^0 and RM is therefore

$$V = \frac{\int d^2x \vec{\nabla} RM(\vec{x}) \cdot \vec{\nabla} \varphi^0(\vec{x})}{\int d^2x |\vec{\nabla} RM(\vec{x})| |\vec{\nabla} \varphi^0(\vec{x})|}, \quad (4.9)$$

where $\vec{\nabla}RM(\vec{x})$ and $\vec{\nabla}\varphi^0(\vec{x})$ are the gradients of RM and φ^0 . A map pair, which was constructed from a set of independent random polarisation angle maps $\varphi(k)$, will give a $V \geq -1$. A map pair without any correlated noise will give a $V \approx 0$. Hence, the statistic V is suitable to detect especially correlated small scale pixel noise.

The denominator in Eq. (4.9) is the normalisation and enables the comparison of V for RM maps of different sources, since V is proportional to the fraction of gradients which are artefacts. Since, the comparison of the quality between maps calculated for the same source using the two different algorithms is desired, it is useful to introduce the unnormalised quantity

$$\tilde{V} = \int d^2x \vec{\nabla}RM(\vec{x}) \cdot \vec{\nabla}\varphi^0(\vec{x}). \quad (4.10)$$

The quantity \tilde{V} gives the absolute measure of correlation between the gradient alignments of RM and φ^0 . The smaller this value is the smaller is the total level of correlated noise in the maps.

4.4.2 Error Under or Over Estimation

One problem, one is faced with is the possibility that the measurement errors are under or overestimated. Such a hypothesis can be tested by performing a reduced χ^2_ν test which is considered to be a measure for the goodness of each least squares fit and calculates as follows

$$\chi^2_{\nu ij} = \frac{1}{\nu} \sum_{k=1}^f \frac{[\varphi_{\text{obs}ij}(k) - (RM_{ij} \lambda_k^2 + \varphi_{ij}^0)]^2}{\sigma_{kij}^2} = \frac{s_{ij}^2}{\langle \sigma_{kij} \rangle_k}, \quad (4.11)$$

where $\nu = f - n_c$ is the number of degrees of freedom and f is the number of frequencies used and n_c is the number of model parameters (here $n_c = 2$). The parameter s^2 is the variance of the fit and $\langle \sigma_{kij} \rangle_k$ is the weighted average of the individual variances:

$$\langle \sigma_{kij} \rangle_k = \left[\frac{1}{f} \sum_{k=1}^f \frac{1}{\sigma_{kij}^2} \right]^{-1} \quad (4.12)$$

If one believes in the assumption of Gaussian noise, that the data are not corrupted and that the linear fit is an appropriate model then any statistical deviation from unity of the map average $\bar{\chi}_\nu^2$ of this value indicates an under or over error estimation. For a $\bar{\chi}_\nu^2 > 1$, the errors have been underestimated and for a $\bar{\chi}_\nu^2 < 1$, they have been overestimated.

Unfortunately this analysis does not reveal in its simple form at which frequency the errors might be under or overestimated. However, one can test for the influence of single frequencies by leaving out the appropriate frequency for the calculation of the RM map and comparing the resulting $\chi^2_{\nu ij}$ values with the original one.

It is advisable to evaluate the reduced $\chi^2_{\nu ij}$ -maps in order to locate regions of too high or too low values for χ^2_ν by eye.

4.4.3 Magnetic Power Spectra

The *Pacman* algorithm is especially useful for the determination of RM maps of extended radio sources. RM maps of extended radio sources are frequently analysed in terms of correlation length and the RM producing magnetic field strength. One analysis relying on statistical methods in order to derive magnetic field power spectra was developed in Chapter 3. It was realised that the method is sensitive to map making artefacts and pixel noise, which can lead to misinterpretation of the data at hand. Therefore this method is a good opportunity to study the influences of noise and artifacts on the resulting power spectra.

The observational nature of the data is taken into account by introducing a window function, which can be interpreted as the sampling volume. Especially, a noise reducing data weighting scheme can be introduced to account for observational noise. One reasonable choice of weighting is to introduce a factor $\sigma_0^{RM}/\sigma_{ij}^{RM}$, which is called simple window weighting in the following. Another possible weighting scheme is a thresholding scheme described by $1/(1 + \sigma_0^{RM}/\sigma_{ij}^{RM})$, which means that the noise below a certain threshold σ_0^{RM} is acceptable and areas of higher noise are down-weighted.

Note, that magnetic power spectra, which are calculated using the approach explained above, are used as a valuable estimator for magnetic field strengths and correlation lengths. However, since the spectra are shaped by and are very sensitive to small scale noise and map making artefacts, they are used here to quantify the influence of noise and artefacts rather than as an estimator for characteristic properties of the RM producing magnetic fields.

4.5 Application to Data

For the calculation of what is called further on the standard fit RM maps, the least squares method was used as suggested by Vallée & Kronberg (1975) and Haves (1975). Also for the individual RM fits, this method was adopted. As an upper limit for the RM values $|RM|_{ij} = RM^{\max} \pm 3\sigma_{ij}^{RM}$ was used, where σ_{ij}^{RM} was calculated following Eq. (4.5). The least-squares fit for the individual data points were always performed as error weighted fits as described by Eq. (4.3) and (4.4), if not stated otherwise. For the *Pacman* calculations, $\alpha = \beta = 1$ was used for the free parameters in Eq. (4.7).

However, the method suggested by Ruzmaikin & Sokoloff (1979) was also used as standard fit algorithm. The results did not change substantially.

4.5.1 Abell 2255E

The Abell cluster 2255, which has a redshift of 0.0806 (Struble & Rood 1999), has been studied by Burns et al. (1995) and Feretti et al. (1997). The polarised radio source B1713+641, which is called hereafter A2255E, has a two sided radio lobe structure and is not directly located in the cluster centre. Polarisation observations were performed using the Very Large Array (VLA) at 4535, 4885, 8085, and 8465 MHz. The data reduction was done with standard AIPS (Astronomical Imaging Processing Software) routines (Govoni et al., in prep.). The polarisation angle maps and their standard error

maps for the four frequencies were kindly provided by Federica Govoni. A preliminary analysis of an RM map of this source in order to determine the properties of the magnetic field in the intra-cluster gas in Abell 2255 is presented in Govoni et al. (2002).

Using the polarisation angle data, an RM map employing the standard fit algorithm was calculated, where the maximal allowed error in polarisation angle was chosen to be $\sigma_k^{\max} = 25^\circ$. The resulting RM map is shown in the upper left panel of Fig. 4.3. The overlaid contour indicates the area which would be covered if polarisation angle errors were limited by $\sigma_k^{\max} = 10^\circ$. For these calculations, it was assumed that $RM^{\max} = 1500 \text{ rad m}^{-2}$.

As can be seen from this map, typical RM values range between -100 rad m^{-2} and $+210 \text{ rad m}^{-2}$. Since this cluster is not known to inhabit a cooling core in its centre (Feretti et al. 1997), these are expected values. However, the occurrence of RM values around 1000 rad m^{-2} , which can be seen as grey areas in the standard fit map of A2255E, might indicate that for these areas the $n\pi$ -ambiguity was not properly solved. One reason for this suspicion is found in the rapid change of RM values occurring between 1 or 2 pixel from 100 to 1000 rad m^{-2} . All these jumps have a ΔRM of about 1000 rad m^{-2} indicating $n\pi$ -ambiguities between 4 GHz and 8 GHz which can be theoretically calculated from $\Delta RM = \pi/(\lambda_2^2 - \lambda_1^2)$. Another important point to note is that parts of the grey areas lie well within the $\sigma_k^{\max} = 10^\circ$ contour, and hence, contribute to the results of any statistical analysis of such a parametrised RM map.

Therefore, the polarisation data of this source provide a good possibility to demonstrate the robustness and the reliability of the proposed algorithm. The RM map calculated by *Pacman* is shown in the middle left panel. The same numbers for the corresponding parameters were used; $\sigma_k^{\max} = 25^\circ$, $RM^{\max} = 1500 \text{ rad m}^{-2}$.

An initial comparison by eye reveals that the method used in the standard fit procedure produces spurious RM 's in noisy regions (manifested as grey areas in the upper left panel of Fig. 4.3) as previously mentioned while the RM map calculated by *Pacman* shows no such grey areas. The apparent jumps of about 1000 rad m^{-2} observed in the standard fit map have disappeared in the *Pacman* map. Note, that in principle by realising that these steps are due to $n\pi$ -ambiguities, one could re-run the standard fit algorithm with a lower RM_{\max} and this wrong solutions would disappear. However, by doing this a very strong bias is introduced since there might also be large RM values which are real. This bias can be easily relaxed by using *Pacman*.

A pixel-by-pixel comparison is shown in Fig. 4.4. In this figure the RM_{stdfit} values obtained for pixels using a standard fit are plotted on the y -axis against the RM_{Pacman} values obtained at the same corresponding pixel locations using the *Pacman* algorithm on the x -axis. The black points represent the error weighted standard fit whereas the red points represent the non-error weighted standard fit. Note that *Pacman* applied only an error weighted least-squares fit to the data. From this scatter plot, one can clearly see that both methods yield the same RM values for most of the points which is expected from the visual comparison of both maps. However, the points for RM_{stdfit} values at around $\pm 1000 \text{ rad m}^{-2}$ are due to the wrong solution of the $n\pi$ -ambiguity found by the standard fit algorithm.

For the demonstration of the effect of $n\pi$ -ambiguity artefacts and pixel noise on statistical analysis, the cluster magnetic field power spectra were determined by employing the approach which was briefly described in Sect. 4.4.3. For detailed dis-

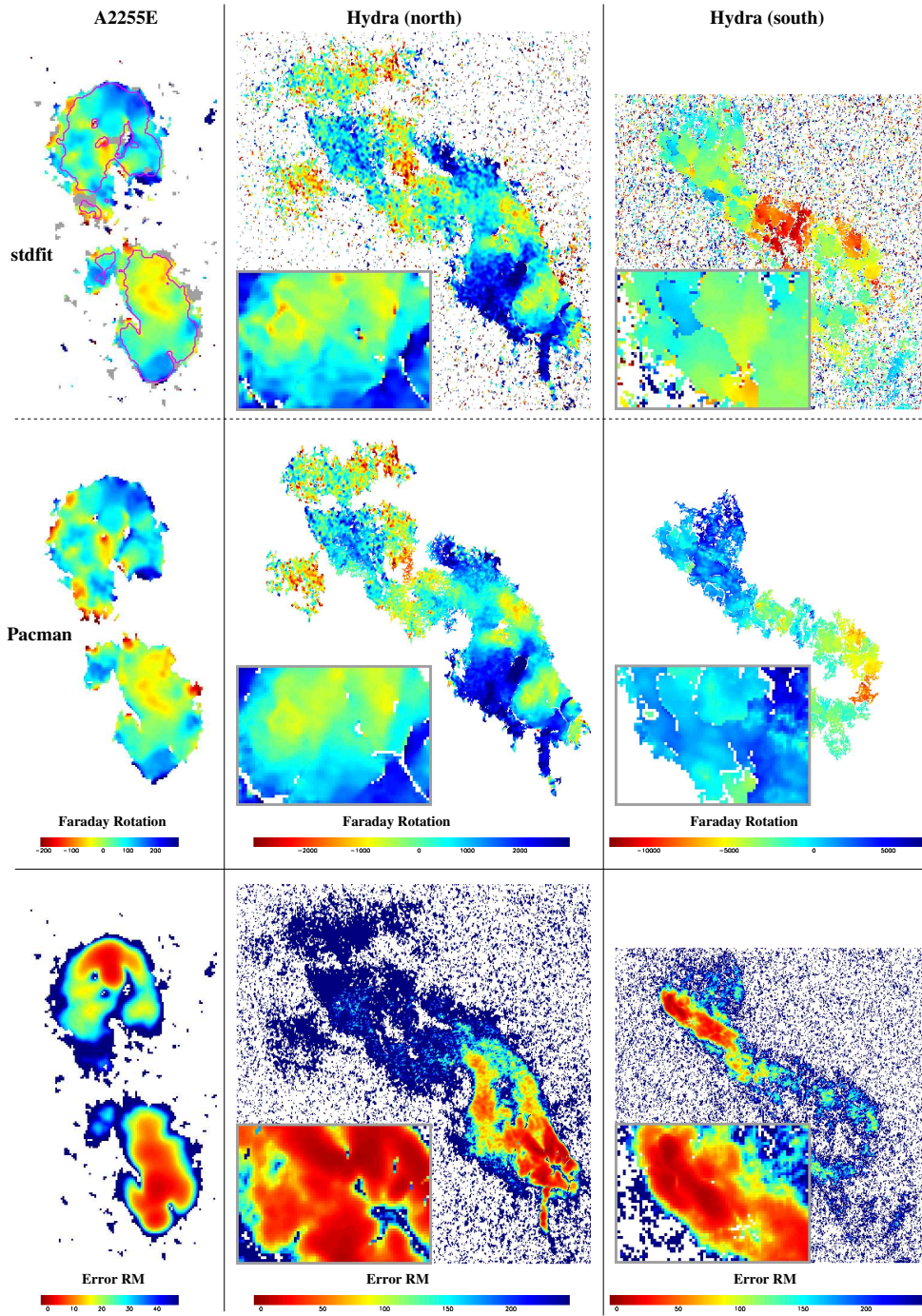


Figure 4.3: Comparison of the standard fit RM maps (upper panels) and the *Pacman* RM maps (middle panels) for A2255E (left column), the north (middle column) and the south lobe (right column) of Hydra A. RM values not represented by the colour bar are coloured in grey. Panels at the bottom exhibit the respective σ^{RM} -maps. For the standard fit RM map of A2255E a $\sigma_k^{\max} = 25^\circ$ and $k_{\min} = f = 4$ was used, contours indicate the area covered by a standard fit RM map with $\sigma_k^{\max} = 10^\circ$. The parameters used for the *Pacman* RM map of A2255E are $\sigma_k^{\max} = 25^\circ$, $\sigma_{\max}^\Delta = 25^\circ$, $g = 1.2$ and $k_{\min} = f = 4$; for the standard fit RM maps of Hydra A are $\sigma_k^{\max} = 25^\circ$ and $k_{\min} = f = 4$ (at 8 GHz); for the *Pacman* RM map of Hydra (north) are $\sigma_k^{\max} = 30^\circ$, $k_{\min} = 4$, $f = 5$, $\sigma_{\max}^\Delta = 25^\circ$ and $g = 1.5$; for the *Pacman* RM map of Hydra (south) are $\sigma_k^{\max} = 35^\circ$, $k_{\min} = f = 5$, $\sigma_{\max}^\Delta = 35^\circ$ and $g = 2.0$.

cussion and description of the application of the method to data, see Chapter 3. In the calculation, it was assumed that the source plane is parallel to the observer plane. Please note, that the application of an RM data filter in order to remove bad data or data which might suffer from a wrong solution to the $n\pi$ -ambiguity as described in Chapter 3 is not necessary here and not desirable. This is on the one hand due to the use of an error weighting scheme in the window function to suppress bad data and on the other hand due to the wish to study the influence of noise and map making artefacts on the power spectra.

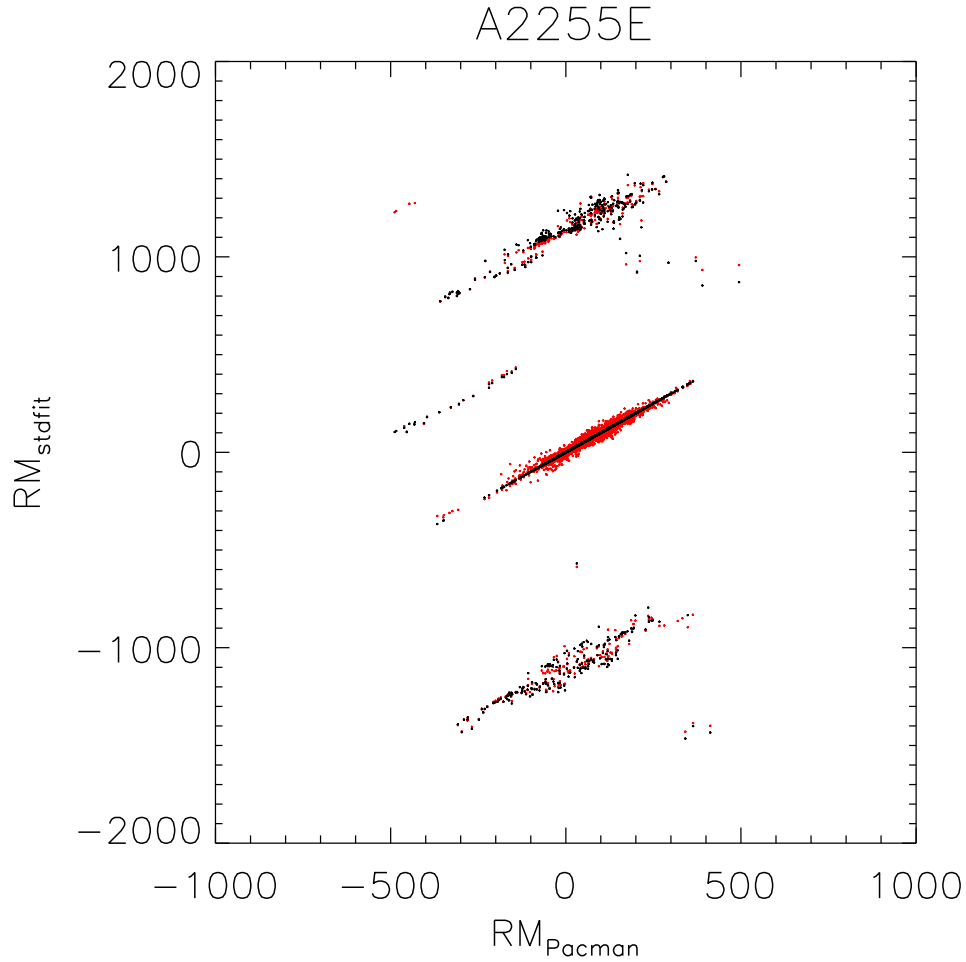


Figure 4.4: A pixel-by-pixel scatter plot of RM_{stdfit} values obtained using the standard fit on the y -axis versus the RM_{Pacman} values calculated from the polarisation data of A2255E by employing the new algorithm *Pacman*. Black points represent results from an error weighted standard least-squares fit and red points from a non-error weighted standard fit. The points for RM_{stdfit} values of around $\pm 1000 \text{ rad m}^{-2}$ are artefacts of a wrong solution of the $n\pi$ -ambiguity.

The RM area used for the calculation of any power spectrum is the RM area which would be covered by the *Pacman* algorithm while using the same set of param-

ter σ_k^{\max} , RM^{\max} . This ensures that pixels on the border or noisy regions of the image not associated with the source – as seen in the standard fit RM map of A2255E in the upper left panel of Fig. 4.3 – are not considered for the analysis. (The same philosophy also applies for the discussion of the Hydra data in Sect. 4.5.2 and Sect. 4.5.3).

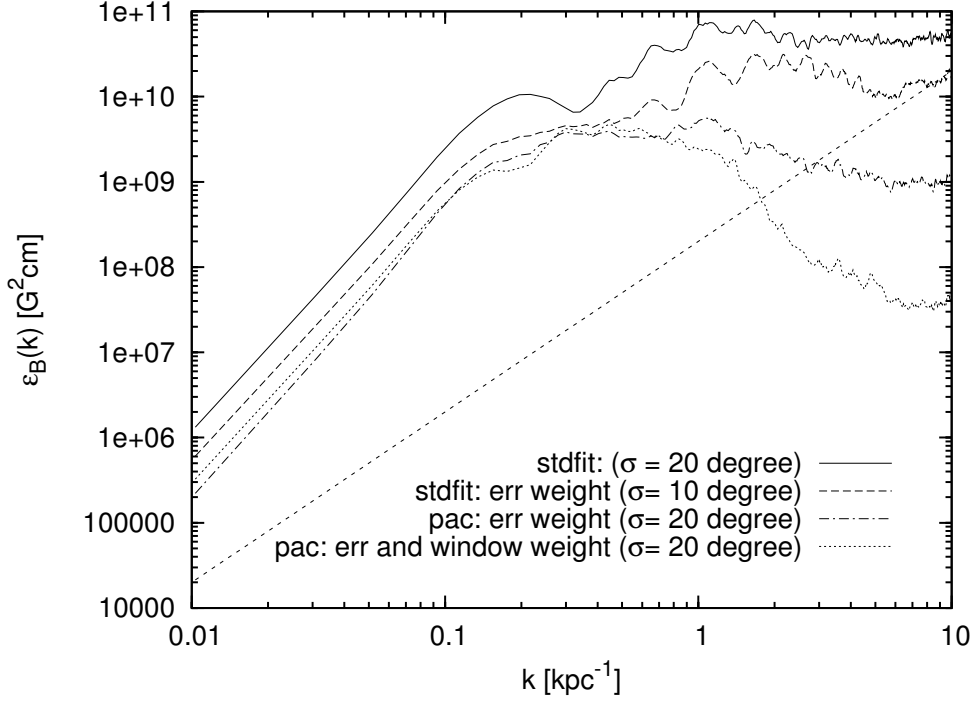


Figure 4.5: Various power spectra for the cluster Abell 2255 determined from different RM map making scenarios are shown. The solid line represents a power spectrum calculated from a standard fit RM map with $\sigma_k^{\max} = 20^\circ$ where no error weighting was applied. The dashed power spectrum was obtained from a standard fit RM map with $\sigma_k^{\max} = 10^\circ$ where error weighting was applied to the standard fit. The dashed-dotted power spectrum was determined from a *Pacman* RM map with $\sigma_k^{\max} = 20^\circ$ and error weighting was applied to the RM fits. The dotted line represents a power spectrum calculated from a *Pacman* RM map as above, but additionally a simple window weighting was applied for the determination of the power spectra. For comparison, the power spectra of pure white noise is plotted as a straight dashed line.

The power spectra calculated for various map making scenarios are shown in Fig. 4.5. The solid and dashed lines represent power spectra calculated from standard fit RM maps. The solid line was calculated from an RM map which was obtained by using $\sigma_k^{\max} = 20^\circ$ where no error weighting was applied to the standard fit. The possible window weighting as introduced in Sect. 4.4.3 was also not applied. This scenario is therefore considered as a worst case. The dashed line was calculated from an RM map employing an error weighted standard fit while only allowing errors in the polarisation angle of $\sigma_k^{\max} = 10^\circ$. Again no window weighting was applied. From the comparison of these two power spectra alone, one can see that the large k -scales – and thus, small real space scales – are sensitive to pixel-noise. Therefore, the applica-

tion of an error weighted least square fit in the RM calculation leads to a reduction of noise in the power spectra. Note that in these two power spectra, the influence of the $n\pi$ -artefacts are still present even in the error weighted standard fit RM map.

The two remaining power spectra in Fig. 4.5 allow to investigate the influence of the $n\pi$ -artefacts. The dashed-dotted line represents the power spectra as calculated from a *Pacman* RM map allowing $\sigma_k^{\max} = 20^\circ$ performing an error weighted fit. Again, no window weighting was applied to this calculation. One can clearly see that there is one order of magnitude difference between the error weighted standard fit power spectra and the *Pacman* one at large k -values. Since also higher noise levels σ_k^{\max} are allowed for the polarisation angles, this drop can only be explained by the removal of the $n\pi$ -artefacts in the *Pacman* map. That there is still a lot of noise in the map on small real space scales (large k 's), which governs the power spectra on these scales, can be seen from the dotted power spectrum, which was determined as above while applying a simple window weighting in the calculation. There is an additional difference of about one order of magnitude between the two power spectra at large k -scales determined for the two *Pacman* scenarios.

For comparison the power spectrum of pure white noise is plotted as straight dashed line in Fig. 4.5. It can be shown analytically, that white noise as observed through an arbitrary window results in a spectrum of $\varepsilon_B(k) \propto k^2$.

As another independent statistical test, the *gradient vector alignment statistic* \tilde{V} was applied to the RM and φ^0 maps calculated by the *Pacman* and the standard fit algorithm. The gradients of RM and φ^0 were calculated using the scheme as described in Sect. 2.3. For the two RM maps shown in Fig. 4.3, a ratio of $\tilde{V}_{\text{stdfit}}/\tilde{V}_{\text{pacman}} = 20$ was found, which indicates a significant improvement mostly resulting from removing the $n\pi$ -artefacts by the *Pacman* algorithm. The calculation of the normalised quantity V yields $V_{\text{stdfit}} = -0.75$ and $V_{\text{pacman}} = -0.87$. Smoothing the *Pacman* RM map slightly leads to a drastic decrease of the quantities \tilde{V} and V . This indicates that the statistic is still governed by small scale noise. This can be understood by looking at the RM maps of Abell 2255E in Fig. 4.3. The extreme RM values are situated at the margin of the source which is, however, also the noisiest region of the source. Calculating the normalised quantity for the high signal-to-noise region yields $V_{\text{pacman}} = -0.47$.

4.5.2 Hydra North

The polarised radio source Hydra A, which is in the centre of the Abell cluster 780, also known as the Hydra A cluster, is located at a redshift of 0.0538 (de Vaucouleurs et al. 1991). The source Hydra A shows an extended, two-sided radio lobe. Detailed X-ray studies have been performed on this cluster (e.g. Ikebe et al. 1997; Peres et al. 1998; David et al. 2001). They revealed a strong cooling core in the cluster centre. The Faraday rotation structure was observed and analysed by Taylor & Perley (1993). They reported RM values ranging between $-1\,000 \text{ rad m}^{-2}$ and $+3\,300 \text{ rad m}^{-2}$ in the north lobe and values down to $-12\,000 \text{ rad m}^{-2}$ in the south lobe.

Polarisation angle maps and their error maps for frequencies at 7 815, 8 051, 8 165, 8 885 and 14 915 MHz resulting from observation with the Very Large Array were kindly provided by Greg Taylor. A detailed description of the radio data reduction can be found in Taylor et al. (1990) and Taylor & Perley (1993).

This section concentrates on the north lobe of Hydra A whereas the south lobe is

separately discussed in Sect. 4.5.3. The south lobe is more depolarised, leading to a lower signal-to-noise than in the north lobe. The north lobe is a good example of how to treat noise in the data, while the south lobe gives a good opportunity to discuss the limitations and the strength of the algorithm *Pacman*.

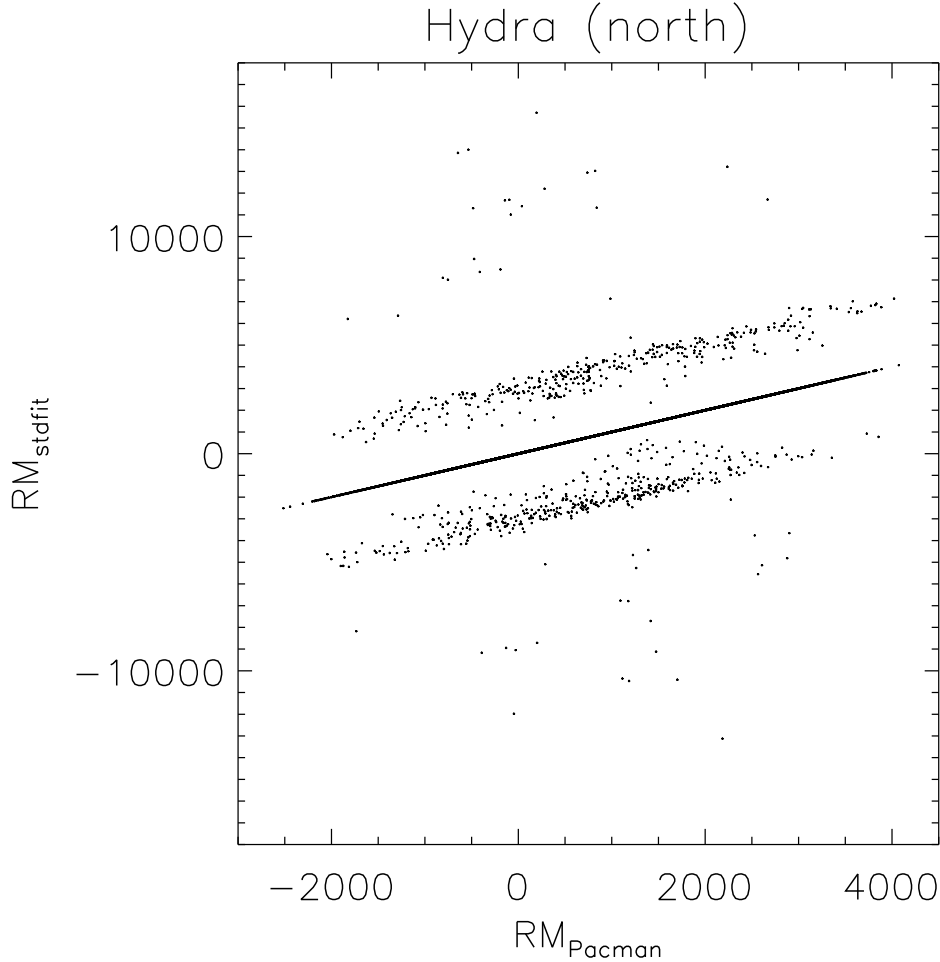


Figure 4.6: A pixel-by-pixel comparison for the Hydra north lobe of RM_{stdfit} values obtained using the standard fit plotted on the y -axis versus the RM_{Pacman} values calculated by employing the new algorithm *Pacman*. The scattered points at ± 3000 - 4000 rad m^{-2} and ± 10000 rad m^{-2} are a result of spurious solutions to the $n\pi$ -ambiguity obtained by the standard fit algorithm. For the calculation of the RM maps, all five frequencies were used.

Using the polarisation data for the four frequencies at around 8 GHz, the standard fit RM map was calculated which is shown in the upper middle panel of Fig. 4.3. The maximal allowed error in polarisation angle was chosen to be $\sigma_k^{\text{max}} = 25^\circ$ and $RM^{\text{max}} = 15000$ rad m^{-2} . A *Pacman* RM map is shown in the middle of the middle panel in Fig. 4.3 below the standard fit map. This map was calculated using the four frequencies at around 8 GHz with a $\sigma_{k=8\text{GHz}}^{\text{max}} = 30^\circ$ and additionally where possible

the fifth frequency at 15 GHz was used with a $\sigma_{k=15GHz}^{\max} = 35^\circ$. RM^{\max} was chosen to be $15\,000 \text{ rad m}^{-2}$. From a visual comparison of the two maps, one can conclude that the standard fit map looks more structured on smaller scales and less smooth than the *Pacman* map. This structure on small scales might be misinterpreted as small scale structure of the *RM* producing magnetic field. Note that the difference in the *RM* maps is mainly due to the usage of the fifth frequency for the *Pacman* map demonstrating that all information available should be used for the calculation of *RM* maps in order to avoid misinterpretation of the data.

Since the four frequencies around 8 GHz are close together, a wrong solution of the $n\pi$ -ambiguity would manifest itself by differences of about $\Delta RM = 10\,000 \text{ rad m}^{-2}$. Such jumps are not observed in the main patches of the standard fit *RM* map shown in Fig. 4.3. However, including the information contained in the polarisation angle map of the 5th frequency at 15 GHz, which is desirable as explained above, one introduces the possibility of $n\pi$ -ambiguities resulting in $\Delta RM = 3\,000..4\,000 \text{ rad m}^{-2}$. Therefore, a scatter plot of a pixel-by-pixel comparison between a standard fit and a *Pacman* map, calculated both using the additional available information on the fifth frequency, is shown in Fig. 4.6. The scattered points are spurious solutions found by the standard fit algorithm. One can clearly see that they develop at $\pm 3000\text{-}4000 \text{ rad m}^{-2}$ and less pronounced at $\pm 10\,000 \text{ rad m}^{-2}$.

In order to study the influence of the noise on small scales, power spectra were calculated from *RM* maps obtained using different parameter sets for the *Pacman* and the standard fit algorithm. As for Abell 2255E, all calculations of power spectra were done for *RM* areas which would be covered by the *Pacman* fit if the same parameters were used. Again this leads to exclusion of pixels in the standard fit *RM* map which are not associated with the source.

There is a clear depolarisation asymmetry of the two lobes of Hydra A observed as described by the Laing–Garrington effect (Taylor & Perley 1993; Lane et al. 2004). Therefore, it is assumed that for the calculation of any power spectra for the Hydra source, the source plane is tilted by an inclination angle of 45° where the north lobe points towards the observer and the south lobe away from the observer.

For a first comparison, the power spectra for two *RM* maps similar to the one shown in Fig. 4.3 were calculated. They were obtained using the four frequencies at 8 GHz for the standard fit algorithm and using additionally the fifth frequency when possible for the *Pacman* algorithm. The other parameters were chosen to be $\sigma_k^{\max} = 35^\circ$ and $RM^{\max} = 15\,000 \text{ rad m}^{-2}$. For these two *RM* maps, the power spectra were determined by applying firstly no window weighting at all and secondly threshold window weighting as described in the end of Sect. 4.4.3. The threshold was chosen to be $\sigma_0^{RM} = 75 \text{ rad m}^{-2}$ which represents the high signal-to-noise region. The respective spectra are exhibited in Fig. 4.7.

For the power spectra, $n\pi$ -artefacts should play only a minor role in the calculation of the power spectra as explained above. Therefore, any differences arising in these spectra are caused by the varying treatment of noise in the map making process or in the analysis. Comparing the power spectra without window weighting, the one obtained from the *Pacman* *RM* map lies below the one from the standard fit *RM* map. The difference is of the order of half a magnitude for large k 's – small real space scales. The standard fit power spectrum seems to increase with larger k but the *Pacman* one seems to decrease over a greater range in k . The reason for this difference is the

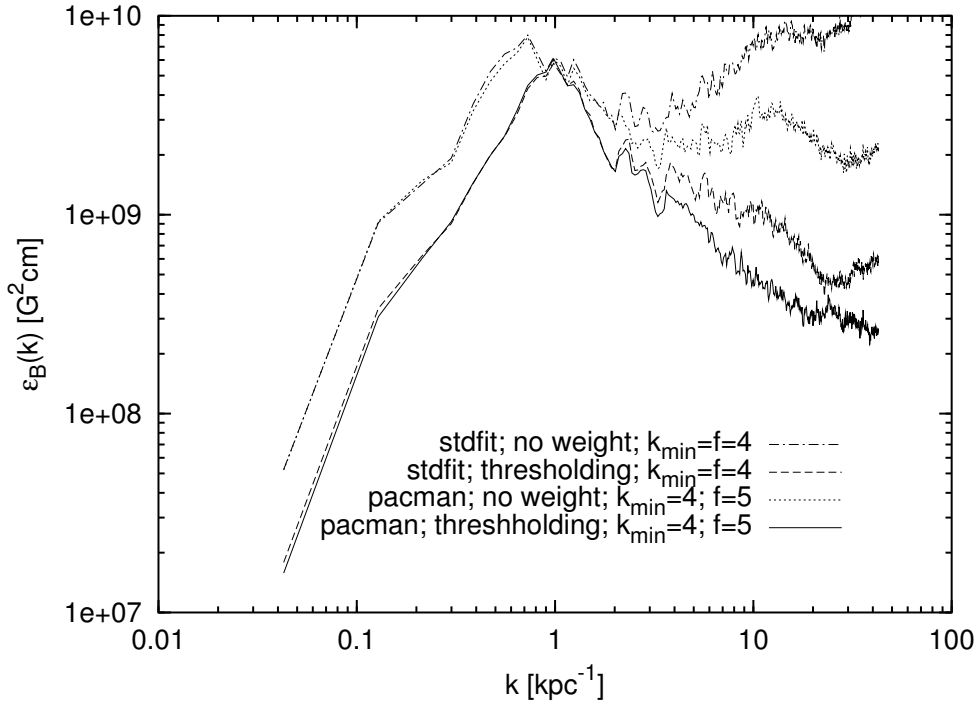


Figure 4.7: Various power spectra calculated for the RM maps for the north lobe of Hydra A are shown. The dashed dotted line and the dotted line represent the power spectra calculated from the standard fit RM map and the *Pacman* RM map, respectively, while no window weighting was applied. A threshold window weighting assuming a $\sigma_0^{RM} = 75 \text{ rad m}^{-2}$ yield the dashed line power spectrum for the standard fit map and the solid line for the *Pacman* map. The standard fit maps were calculated from the four frequencies at 8 GHz whereas the *Pacman* maps were determined using additionally the fifth frequency when possible. For both algorithms, $\sigma_k^{\text{max}} = 35^\circ$ was used. The influence of the small-scale pixel noise on the power spectra can clearly be seen in this figure at large k -values.

same one which was responsible for the different smoothness in the two RM maps shown in Fig. 4.3, namely that only four frequencies were used for the standard fit RM map. Even introducing a window weighting scheme, which down-weights noisy region, cannot account entirely for that difference as can be seen from the comparison of the window weighted power spectra. This is especially true because the small-scale spatial structures are found even in the high signal-to-noise regions when using only four frequencies for the RM map calculation. This demonstrates again how important it is to include all available information in the map making process.

In order to study the influence of the maximal allowed measurement error in the polarisation angle σ_k^{max} , power spectra were calculated for a series of *Pacman* RM maps obtained for σ_k^{max} ranging from 5° to 35° . The RM maps were derived using all five frequencies $k_{\text{min}} = 5$, not allowing any points to be considered for which only four frequencies fulfil $\sigma_{k_{ij}} < \sigma_k^{\text{max}}$. Again an $RM^{\text{max}} = 15000 \text{ rad m}^{-2}$ was used. The resulting power spectra using a threshold window weighting ($\sigma_0^{RM} = 50 \text{ rad m}^{-2}$) are

exhibited in Fig. 4.8. One can see that they are stable and do not differ substantially from each other even though the noise level increases slightly when increasing the σ_k^{\max} . This demonstrates the robustness of the *Pacman* algorithm.

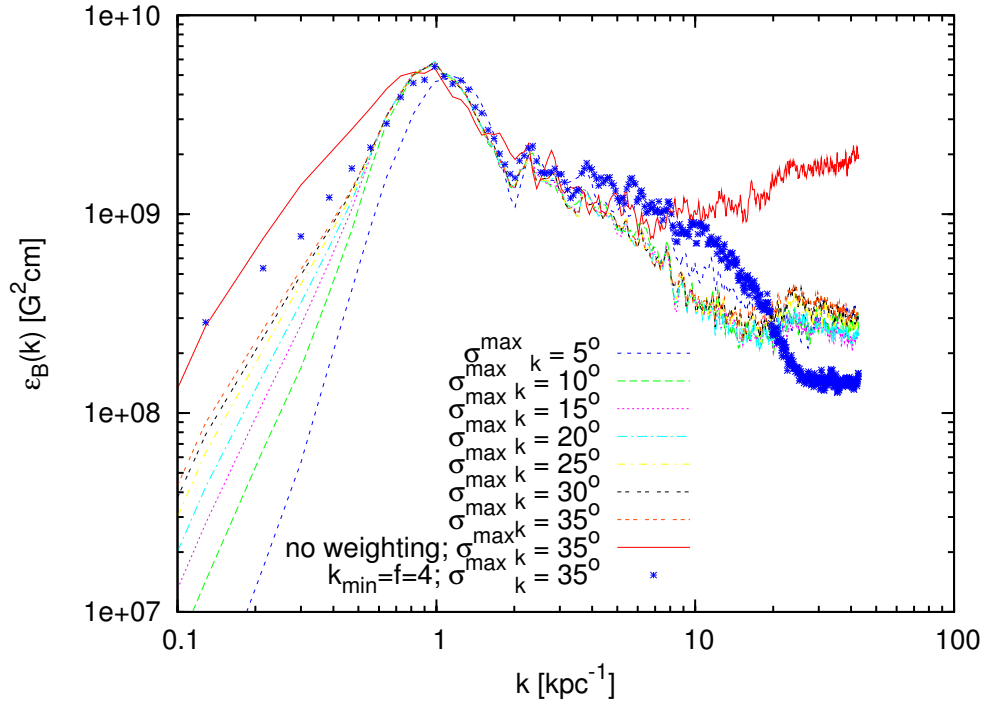


Figure 4.8: Power spectra for the north lobe of Hydra A calculated from a series of *Pacman* *RM* maps are shown. The various coloured dashed and dotted lines show power spectra from *RM* maps calculated for σ_k^{\max} ranging from 5° to 35° using all five frequencies $k_{\min} = 5$. The spectra were determined applying threshold window weighting ($\sigma_0^{RM} = 50 \text{ rad m}^{-2}$). For comparison the solid red line power spectrum, which is the largest spectrum at $k > 10 \text{ kpc}^{-1}$, is not window weighted for $\sigma_k^{\max} = 35^\circ$. The power spectrum represented by the blue stars was derived from a *Pacman* *RM* map obtained using the four frequencies at 8 GHz and a $\sigma_k^{\max} = 35^\circ$.

For comparison, two more power spectra are plotted in Fig. 4.8. For the solid red line spectrum, no window weighting was applied to an *RM* map which was calculated as above having $\sigma_k^{\max} = 35^\circ$. One can clearly see that the spectrum is governed by noise on large k -scales – small real space scales. Thus, some form of window weighting in the calculation of the power spectra seems to be necessary in order to suppress a large amount of noise.

Another aspect arises in the noise treatment if one considers the power spectra represented by the blue stars which was calculated using a threshold window weighting ($\sigma_0 = 50 \text{ rad m}^{-2}$). This power spectrum represents the analysis for an *RM* map obtained using only the four frequencies at 8 GHz while $\sigma_k^{\max} = 35^\circ$. It is striking that the noise level on large k -scales (on small real space scales) is lower than for the *RM* maps obtained for the five frequencies, one would expect it to be the other way round. Apparently the fifth frequency has a lot of weight in the determination of σ_{ij}^{RM}

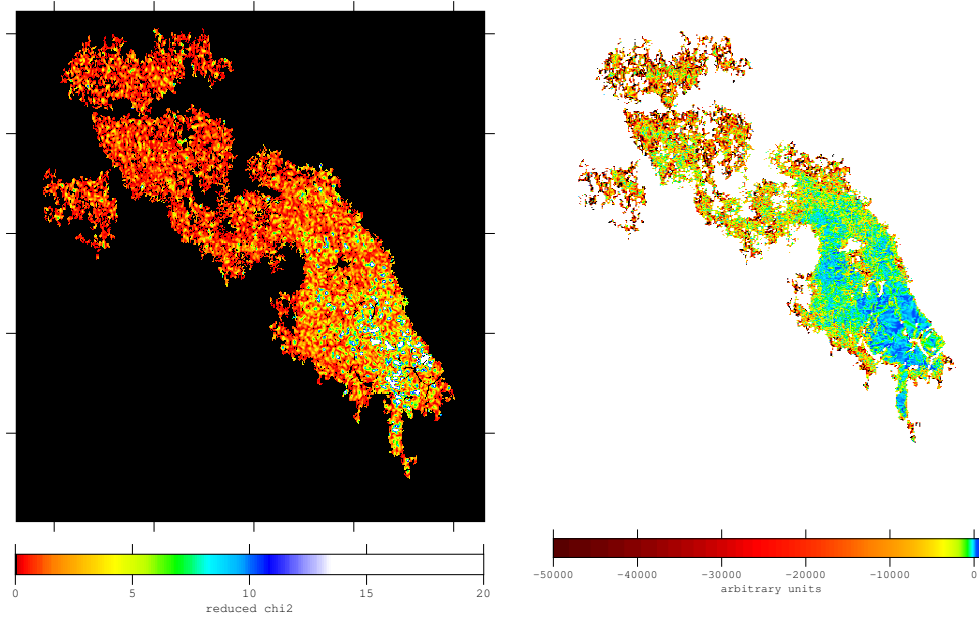


Figure 4.9: On the left panel, a $\chi_{\nu_{ij}}^2$ map is shown. The yellow and green regions have values larger than unity indicating underestimation of errors. Note that for these regions for the RM fit five frequencies were used whereas in the outer parts of the source only four frequencies were used. A \tilde{V} map for the north lobe of Hydra A is exhibited on the right panel. The extreme negative values (red and black) correspond to strong anti-correlation of RM and φ^0 fluctuations, which are produced by noise in the observed maps. However, the green and blue coloured regions have values around zero and are therefore high signal-to-noise regions (compare with the σ^{RM} map in the lower middle panel of Fig. 4.3).

(see Eq. (4.3)) since this frequency is almost twice as large as the other four. If the measurement errors of the polarisation angles are underestimated this can lead to an underestimation of the uncertainty σ_{ij}^{RM} in the final RM value due to Gaussian error propagation.

One can test the hypothesis of underestimation of errors by performing a reduced χ_{ν}^2 test as described in Sect. 4.4.2. The reduced $\chi_{\nu_{ij}}^2$ map for the *Pacman* RM map of Hydra North derived by using a multi-frequency fit (see middle upper panel of Fig. 4.3) is exhibited in the left panel of Fig. 4.9. The red values are close to unity. However the yellow and blue regions in this map are values larger than unity indicating that the errors are underestimated in these regions. Note that in these regions there is also the fifth frequency used for the RM fit which might indicate that the errors for this frequency are underestimated by a larger factor than for the other four frequencies.

The *gradient vector product statistic* \tilde{V} was also applied to the RM and φ^0 maps obtained by using the RM maps as shown in the middle panel of Fig. 4.3 and the respective φ^0 maps. The calculation yields for the ratio $\tilde{V}_{\text{stdfit}}/\tilde{V}_{\text{pacman}} = 1.2$. This corresponds to a slight decrease of correlated noise in the *Pacman* maps. The calculation of the normalised quantity results in $V_{\text{stdfit}} = -0.85$ for the standard fit and $V_{\text{pacman}} = -0.83$ for the *Pacman* maps. This is expected since the low signal-to-noise

areas of the north lobe of Hydra A will govern this gradient statistic and for both RM maps these areas look very similar. In order to visualise this, a \tilde{V} map was calculated which is exhibited on the right panel of Fig. 4.9. The extreme negative values observed for the low signal-to-noise regions (red regions) indicate strong anti-correlation and thus, anti-correlated fluctuations of RM and φ^0 in these regions. For the high signal-to-noise regions (blue and green) moderate values varying around zero are observed. Note the striking morphological similarity of the RM error (σ^{RM}) map in the lower middle panel of Fig. 4.3 and of the \tilde{V} map as shown in Fig. 4.9. These two independent approaches to measure the RM maps accuracy give a basically identical picture. These approaches are complementary since they use independent information. The RM error map is calculated solely from σ_k maps, which are based on the absolute polarisation errors, whereas the \tilde{V} map is based solely on the RM derived from the polarisation angle $\varphi(k)$ maps.

However, note that the results for magnetic field strengths and correlation lengths presented in Chapter 3 are not changed substantially. This is owing to the fact that in Chapter 3 only the power on scales which were larger than the resolution element (beam) was considered for the calculation of the magnetic field properties. Therefore the small scale noise was not considered for this calculation and thus, no change in the results given is expected. The central magnetic field strength for this cluster as derived during the course of this work is about $10 \mu\text{G}$ and the field correlation length is about 1 kpc being consistent with the results presented in Chapter 3.

4.5.3 The Quest for Hydra South

As already mentioned, the southern part of the Hydra source has to be addressed separately, as it differs from the northern part in many respects. One of them is that the depolarisation is higher in the south lobe which especially complicates the analysis of this part.

An RM map obtained employing the standard fit algorithm using the four frequencies at 8 GHz is shown in the upper right panel of Fig. 4.3. This RM map exhibits many jumps in the RM distribution which seems to be split in lots of small patches having similar RM 's. Furthermore, RM 's of $-12\,000 \text{ rad m}^{-2}$ are detected (indicated as red regions in the map). If one includes the fifth frequency at 15 GHz in the standard fit algorithm, the appearance of the RM map does not change significantly, and most importantly, the extreme values of about $-12\,000 \text{ rad m}^{-2}$ do not vanish.

The application of the *Pacman* algorithm with conservative settings for the parameters σ_k^{max} , $\sigma_{\text{max}}^{\Delta}$ and g , leads to a splitting of the RM distribution into many small, spatially disconnected patches. Such a map does look like a standard fit RM map and there are still the RM jumps and the extreme RM values present. However, if one lowers the restrictions for the construction of patches, the *Pacman* algorithm starts to connect patches to the patch with the best quality data available in the south lobe using its information on the global solution of the $n\pi$ -ambiguity. An RM map obtained pushing *Pacman* to such limits is exhibited in the middle right panel of Fig. 4.3. Note that the best quality area is covered by the bright blue regions and a zoom-in for this region is also exhibited in the small box to the lower left of the source. In the lowest right panel of Fig. 4.3, a σ^{RM} -map is shown indicating the high quality regions by the red colour.

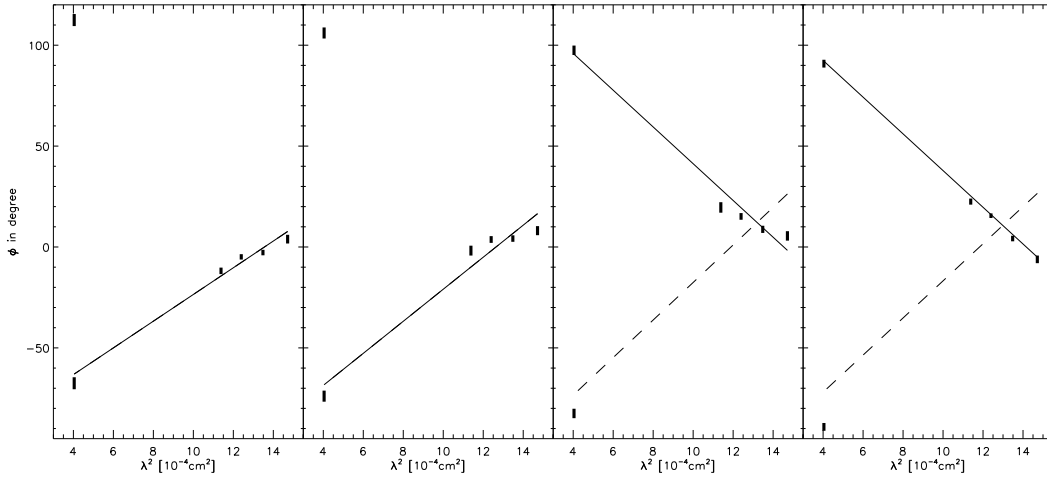


Figure 4.10: An example for individual RM fits across an RM jump observed in the RM maps of the south lobe of Hydra A. The solid line indicates the standard fit solution and the dashed one represents the *Pacman* solution. The error bars in these plots indicate the polarisation errors which were multiplied by 3. Note that this is an extreme example, where *Pacman* chooses a solution to the individual fits in noisy regions which has not necessarily the minimal χ^2 value by construction. However, the global statistical tests applied to the whole RM map of Hydra South indicate that the *Pacman* map has less artefacts in comparison to the standard fit RM map. Note, that for this particular local example it is not trivial to decide which algorithm is giving the right solution.

The RM distribution in this *Pacman* map exhibits clearly fewer jumps than the standard fit map although the jumps do not vanish entirely. Another feature that almost vanishes in the *Pacman* map are the extreme RM 's of about $-12\,000\text{ rad m}^{-2}$. The RM distribution of the *Pacman* map seems to be smoother than the one of the standard fit map. However, if the individual RM fits for points, which deviate in their RM values depending on the algorithm used, are compared in a $\varphi(k)$ - λ_k^2 -diagram, the standard fit seems to be the one which would have to be preferred since it does fit better to the data at hand. *Pacman* has some resistance to pick this smallest χ^2 solution if it does not make sense in the context of neighbouring pixel information. As an example, individual RM fits which are observed across the RM jumps are plotted in Fig. 4.10. However as shown above, one has to consider that the measurement errors might be underestimated which gives much tighter constraints on the fit than it would otherwise be.

In order to investigate these maps further, the threshold weighted ($\sigma_0^{RM} = 50\text{ rad m}^{-2}$) and the simple weighted power spectra were also calculated from the *Pacman* and the standard fit RM maps of the south lobe and were compared to the one from the north lobe. The RM maps used for the comparison were all calculated employing $\sigma_k^{\max} = 35^\circ$ and $k_{\min} = f = 5$. The various power spectra are shown in Fig. 4.11. One can clearly see that the power spectra calculated for the south lobe lie well above the power spectra from the north lobe, which is represented as filled circles.

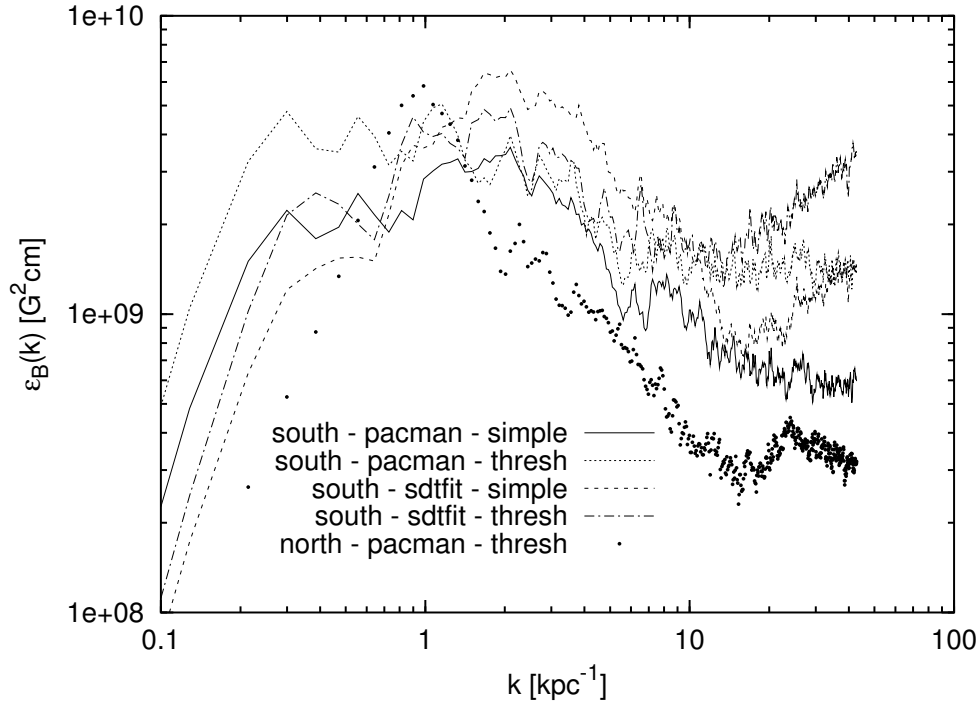


Figure 4.11: Various power spectra for the RM maps of the south lobe of the Hydra source are compared with the power spectrum of the north lobe calculated from the *Pacman* RM map ($k_{\min} = 5$, $\sigma_k^{\max} = 35^\circ$) employing a threshold weighting with $\sigma_0^{RM} = 50 \text{ rad m}^{-2}$ represented as filled circles.

Concentrating on the comparison of the simple window weighted power spectra of the south lobe in Fig. 4.11 (the solid line is from *Pacman* RM map and the dashed line is from standard fit RM map) to the one of the north lobe, one finds that the power spectrum calculated from the *Pacman* RM map is closer to the one from the north lobe than the power spectrum derived from the standard fit RM map. This indicates that the *Pacman* RM map might be the right solution to the RM determination problem for this part of the source. However, this difference vanishes if a different window weighting scheme is applied to the calculation of the power spectrum. This can be seen by comparing the threshold window weighted power spectra (dotted line for the power spectra of the *Pacman* RM map and dashed dotted line for the power spectra from the standard fit RM map) in Fig. 4.11. Since the choice of the window weighting scheme seems to have also an influence on the result the situation is still inconclusive.

An indication for the right solution of the $n\pi$ -ambiguity problem may be found in the application of the *gradient vector product statistic* \tilde{V} to the *Pacman* maps and the standard fit maps of the south lobe (as shown in Fig. 4.3). The calculations yield a ratio $\tilde{V}_{\text{stdfit}}/\tilde{V}_{\text{pacman}} = 12$. This is a difference of one order of magnitude and represents a substantial decrease in correlated noise in the *Pacman* maps. The calculation of the normalised quantity yields $V_{\text{stdfit}} = -0.69$ for the standard fit maps and $V_{\text{pacman}} = -0.47$ for the *Pacman* maps. This result strongly indicates that the *Pacman* map should be the preferred one.

The final answer to the question about the right solution of the RM distribution problem for the south lobe of Hydra A has to be postponed until observations of even higher sensitivity, higher spatial resolutions and preferably also at different frequencies are available.

4.6 Lessons & Conclusions

A new algorithm for the calculation of Faraday rotation maps from multi-frequency polarisation data sets was presented. Unlike other methods, this algorithm uses global information and connects information about individual neighbouring pixels with one another. It assumes that if regions exhibit small polarisation angle gradients between neighbouring pixels in all observed frequencies simultaneously, then these pixels can be considered as connected, and information about one pixel can be used for neighbouring ones, and especially, the solution to the $n\pi$ -ambiguity should be the same. It is stressed here, that this is a very weak assumption, and – like all other criteria used within the *Pacman* algorithm – only depends on the polarisation data at hand and the signal-to-noise ratio of the observations.

The *Pacman* algorithm is especially useful for the calculation of RM and φ^0 maps of extended radio sources and its robustness was demonstrated. Global algorithms as implemented in *Pacman* are preferable for the calculation of RM maps and needed if reliable RM values are desired from low signal-to-noise regions of the source.

The *Pacman* algorithm reduces $n\pi$ -artefacts in noisy regions and makes the unambiguous determination of RM and φ^0 in these regions possible. *Pacman* allows to use all available information obtained by the observation. Any statistical analysis of the RM maps will profit from these improvements.

In the course of this work, the following lessons were learned:

1. It is important to use all available information obtained by the observation. It seems especially desirable to have a good frequency coverage. The result is a smoother, less noisy map.
2. For the individual least-squares fits of the RM , it is advisable to use an error weighting scheme in order to reduce the noise.
3. Global algorithms are preferable, if reliable RM values are needed from low signal-to-noise regions at the edge of the source.
4. Sometimes it is necessary to test many values of the parameters RM^{\max} , σ_k^{\max} and σ_{\max}^{Δ} , which govern the *Pacman* algorithm, in order to investigate the influence on the resulting RM maps.
5. One has to keep in mind that whichever RM map seems to be most believable, it might still contain artefacts. One should do a careful analysis by looking on individual RM pixel fits but one also should consider the global RM distribution. The *gradient vector product statistic* \tilde{V} was presented as a useful tool to estimate the level of reduction of cross-correlated noise in the calculated RM and φ^0 maps.

6. For the calculation of power spectra it is always preferable to use a window weighting scheme which has to be carefully selected.
7. Finally, under or overestimation of the measurement errors of polarisation angles (which will propagate through all calculations due to error propagation) could influence the final results. A reduced χ^2_ν test was performed in order to test if the errors are over or under estimated.

One can conclude that the calculation of *RM* maps is a very difficult task requiring a critical view to the data and a careful noise analysis. However, *Pacman* offers a good opportunity to calculate reliable *RM* maps and to understand the data and its limitations better. Furthermore, improved *RM* maps and the according error analysis for Hydra North and A2255E were presented in this chapter.

Chapter 5

A Bayesian View on Faraday Rotation Maps – Seeing the Magnetic Power Spectra in Galaxy Clusters

In the last chapter, a method was introduced in order to calculate reliable Faraday rotation maps from multi-frequency polarisation data sets suppressing map making artefacts. In order to use the full potential of these high quality RM maps, an accurate power spectrum estimator based on Bayesian maximum likelihood methods is developed and successfully applied in this chapter.

This work is submitted as Vogt & Enßlin to *Astron. & Astrophys.*

5.1 Introduction

In Chapter 3, a method in order to determine the magnetic power spectra by Fourier transforming RM maps was proposed. Based on these considerations, this method was applied to observational data and the magnetic power spectrum of three clusters (Abell 400, Abell 2634 and Hydra A) was determined from RM maps of radio sources located in these clusters. Furthermore, field strengths of $\sim 12 \mu\text{G}$ were determined for the cooling flow cluster Hydra A, $3 \mu\text{G}$ and $6 \mu\text{G}$ for the non-cooling flow clusters Abell 2634 and Abell 400, respectively. This analysis revealed spectral slopes of the power spectra with spectral indices $-2.0 \dots -1.6$. However, it was realised that using the proposed analysis, it is difficult to reliably determine differential quantities such as spectral indices due to the complicated shapes of the used emission regions which lead to a redistribution of magnetic power within the spectra.

Recently, Murgia et al. (2004) proposed a numerical method in order to determine the magnetic power spectrum in clusters. They infer the magnetic field strength and structure by comparing simulations of RM maps as caused by multi-scale magnetic fields with the observed polarisation properties of extended cluster radio sources such as radio galaxies and haloes. They argue that field strengths derived in the literature using analytical expressions have been overestimated the field strengths by a factor of

~ 2 .

In order to determine a power spectrum from observational data, maximum likelihood estimators are widely used in astronomy. These methods and algorithms have been greatly improved especially by the Cosmic Microwave Background (CMB) analysis which is facing the problem of determining the power spectrum from large CMB maps. Kolatt (1998) proposed to use such an estimator to determine the power spectrum of a primordial magnetic field from the distribution of RM measurements of distant radio galaxies.

Based on the initial idea of Kolatt (1998), the methods developed by the CMB community (especially Bond et al. 1998) and the understanding of the magnetic power spectrum of cluster gas (Enßlin & Vogt 2003), a Bayesian maximum likelihood approach is derived to calculate the magnetic power spectrum of cluster gas given observed Faraday rotation maps of extended extragalactic radio sources. The power spectrum enables to determine also characteristic field length scales and strengths. After testing the method on artificial generated RM maps with known power spectra, the analysis is applied to a Faraday rotation map of Hydra A North. The data were kindly provided by Greg Taylor. In addition, this method allows to determine the uncertainties of the measurement and, thus, one is able to give errors on the calculated quantities. Based on these calculations, statements for the nature of turbulence for the magnetised gas are derived.

In Sect. 5.2, a method employing a maximum likelihood estimator as suggested by Bond et al. (1998) in order to determine the magnetic power spectrum from RM maps is introduced. Special requirements for the analysis of RM maps with such a method are discussed. In Sect. 5.3, the maximum likelihood estimator is applied to generated RM maps with known power spectra in order to test the algorithm. In Sect. 5.4, the application of the method to data of Hydra A is described. In Sect. 5.5, the derived power spectra are presented and the results are discussed. In the last Sect. 5.6, conclusions are drawn.

Throughout the rest of this chapter, a Hubble constant of $H_0 = 70 \text{ km s}^{-1} \text{ Mpc}^{-1}$, $\Omega_m = 0.3$ and $\Omega_\Lambda = 0.7$ in a flat universe are assumed. All equations follow the notation of Chapter 3.

5.2 Maximum Likelihood Analysis

5.2.1 The Covariance Matrix C_{RM}

One of the most common used methods of Bayesian statistic is the maximum likelihood method. The likelihood function for a model characterised by p parameters a_p is equivalent to the probability of the data Δ given a particular set of a_p and can be expressed in the case of (near) Gaussian statistic of Δ as

$$\mathcal{L}_\Delta(a_p) = \frac{1}{(2\pi)^{n/2} |C|^{1/2}} \cdot \exp\left(-\frac{1}{2} \Delta^T C^{-1} \Delta\right), \quad (5.1)$$

where $|C|$ indicates the determinant of a matrix, $\Delta_i = RM_i$ are the actual observed data, n indicates the number of observationally independent points and $C = C(a_p)$ is the covariance matrix. This covariance matrix can be defined as

$$C_{ij}(a_p) = \langle \Delta_i^{obs} \Delta_j^{obs} \rangle = \langle RM_i^{obs} RM_j^{obs} \rangle, \quad (5.2)$$

where the brackets $\langle \rangle$ denote the expectation value and, thus, $C_{ij}(a_p)$ describes the expectation based on the proposed model characterised by a particular set of a_p 's. Now, the likelihood function $\mathcal{L}_{\Delta}(a_p)$ has to be maximised for the parameters a_p . Note, that although the magnetic fields might be non-Gaussian, the RM should be close to Gaussian due to the central limit theorem. Observationally, RM distributions are known to be close to Gaussian (e.g. Taylor & Perley 1993; Feretti et al. 1999a,b; Taylor et al. 2001).

Ideally, the covariance matrix is the sum of a signal and a noise matrix term which results if the errors are uncorrelated to true values. Writing $RM^{obs} = RM^{true} + \delta RM$ results in

$$\begin{aligned} C_{ij}(a_p) &= \langle RM_i^{true} RM_j^{true} \rangle + \langle \delta RM_i \delta RM_j \rangle \\ &= C_{RM}(\vec{x}_{\perp i}, \vec{x}_{\perp j}) + \langle \delta RM_i \delta RM_j \rangle \end{aligned} \quad (5.3)$$

where $\vec{x}_{\perp i}$ is the displacement of point i from the z -axis and $\langle \delta RM_i \delta RM_j \rangle$ indicates the expectation for the uncertainty in the measurement. Unfortunately, while in the discussion of the power spectrum measurements of CMB experiments the noise term is extremely carefully studied, for the discussion here this is not the case and goes beyond the scope of this work. Thus, this term will be neglected throughout the rest of this chapter. However, Johnson et al. (1995) discuss uncertainties involved in the data reduction process in order to gain a model for $\langle \delta RM_i \delta RM_j \rangle$.

Since one is interested in the magnetic power spectrum, one has to find an expression for the covariance matrix $C_{ij}(a_p) = C_{RM}(\vec{x}_{\perp i}, \vec{x}_{\perp j})$ which can be identified as the RM autocorrelation $\langle RM(\vec{x}_{\perp i}) RM(\vec{x}_{\perp j}) \rangle$. This has then to be related to the magnetic power spectra.

The observable in any Faraday experiment is the rotation measure RM . For a line of sight parallel to the z -axis and displaced by \vec{x}_{\perp} from it, the RM arising from polarised emission passing from the source $z_s(\vec{x}_{\perp})$ through a magnetised medium to the observer located at infinity is expressed by

$$RM(\vec{x}_{\perp}) = a_0 \int_{z_s(\vec{x}_{\perp})}^{\infty} dz n_e(\vec{x}) B_z(\vec{x}), \quad (5.4)$$

where $a_0 = e^3/(2\pi m_e^2 c^4)$, $\vec{x} = (\vec{x}_{\perp}, z)$, $n_e(\vec{x})$ is the electron density and $B_z(\vec{x})$ is the magnetic field component along the line of sight.

In the following, it is assumed that the magnetic fields in galaxy clusters are isotropically distributed throughout the Faraday screen. If one samples such a field distribution over a large enough volume they can be treated as statistically homogeneous and statistically isotropic. Therefore, any statistical average over a field quantity will not be influenced by the geometry or the exact location of the volume sampled. Following Sect. 3.3, one can define the elements of the RM covariance matrix using the RM autocorrelation function $C_{RM}(\vec{x}_{\perp i}, \vec{x}_{\perp j}) = \langle RM(\vec{x}_{\perp i}) RM(\vec{x}_{\perp j}) \rangle$ and introduce a window function $f(\vec{x})$ which describes the properties of the sampling volume

$$C_{RM}(\vec{x}_{\perp}, \vec{x}'_{\perp}) = \tilde{a}_0^2 \int_{z_s}^{\infty} dz \int_{z'_s}^{\infty} dz' f(\vec{x}) f(\vec{x}') \langle B_z(\vec{x}_{\perp}, z) B_z(\vec{x}'_{\perp}, z') \rangle, \quad (5.5)$$

where $\tilde{a}_0 = a_0 n_{e0}$, the central electron density is n_{e0} and the window function is defined by

$$f(\vec{x}) = \mathbf{1}_{\{\vec{x}_{\perp} \in \Omega\}} \mathbf{1}_{\{z \geq z_s(\vec{x}_{\perp})\}} g(\vec{x}) n_e(\vec{x}) / n_{e0}, \quad (5.6)$$

where $\mathbf{1}_{\{condition\}}$ is equal to unity if the condition is true and zero if not and Ω defines the region for which RM 's were actually measured. The electron density distribution $n_e(\vec{x})$ is chosen with respect to a reference point \vec{x}_{ref} (usually the cluster centre) such that $n_{e0} = n_e(\vec{x}_{ref})$, e.g. the central density, and $B_0 = \langle \vec{B}^2(\vec{x}_{ref}) \rangle^{1/2}$. The dimensionless average magnetic field profile $g(\vec{x}) = \langle \vec{B}^2(\vec{x}) \rangle^{1/2} / B_0$ is assumed to scale with the density profile such that $g(\vec{x}) = (n_e(\vec{x}) / n_{e0})^{\alpha_B}$.

Setting $\vec{x}' = \vec{x} + \vec{r}$ and assuming that the correlation length of the magnetic field is much smaller than characteristic changes in the electron density distribution, one can separate the two integrals in Eq. (5.5). Furthermore, one can introduce the magnetic field autocorrelation tensor $M_{ij} = \langle B_i(\vec{x}) \cdot B_j(\vec{x} + \vec{r}) \rangle$ (see e.g. Subramanian 1999; Enßlin & Vogt 2003). Taking this into account, the RM autocorrelation function can be described by

$$C_{RM}(\vec{x}_\perp, \vec{x}_\perp + \vec{r}_\perp) = \tilde{a}_0^2 \int_{z_s}^{\infty} dz f(\vec{x}) f(\vec{x} + \vec{r}) \int_{(z'_s - z) \rightarrow -\infty}^{\infty} dr_z M_{zz}(\vec{r}) \quad (5.7)$$

Here, the approximation $(z'_s - z) \rightarrow -\infty$ is valid for Faraday screens which are much thicker than the magnetic autocorrelation length. This will turn out to be the case in the application at hand.

The Fourier transformed zz -component of the autocorrelation tensor $M_{zz}(\vec{k})$ can be expressed by the Fourier transformed scalar magnetic autocorrelation function $w(k) = \sum_i M_{ii}(k)$ and a k dependent term (see Eq. (3.25)) leading to

$$M_{zz}(\vec{r}) = \frac{1}{2\pi^3} \int_{-\infty}^{\infty} d^3k \frac{w(k)}{2} \left(1 - \frac{k_z^2}{k^2} \right) e^{-i\vec{k}\vec{r}} \quad (5.8)$$

Furthermore, the one dimensional magnetic energy power spectrum $\varepsilon_B(k)$ can be expressed in terms of the magnetic autocorrelation function $w(k)$ such that

$$\varepsilon_B(k) dk = \frac{k^2 w(k)}{2(2\pi)^3} dk. \quad (5.9)$$

As stated in Chapter 3, the $k_z = 0$ - plane of $M_{zz}(\vec{k})$ is all that is required to reconstruct the magnetic autocorrelation function $w(k)$. Thus, inserting Eq. (5.8) into Eq. (5.7) and using Eq. (5.9) leads to

$$C_{RM}(\vec{x}_\perp, \vec{x}_\perp + \vec{r}_\perp) = 4\pi^2 \tilde{a}_0^2 \int_{z_s}^{\infty} dz f(\vec{x}) f(\vec{x} + \vec{r}) \times \int_{-\infty}^{\infty} dk \varepsilon_B(k) \frac{J_0(kr_\perp)}{k}, \quad (5.10)$$

where $J_0(kr_\perp)$ is the 0th Bessel function. This equation gives an expression for the RM -autocorrelation function in terms of the magnetic power spectra of the Faraday producing medium.

Since the magnetic power spectrum is the interesting function, one can parametrise $\varepsilon_B(k) = \sum_p \varepsilon_{B_p} \mathbf{1}_{\{k \in [k_p, k_{p+1}]\}}$, where ε_{B_p} is constant in the interval $[k_p, k_{p+1}]$, leading to

$$C_{RM}(\varepsilon_{B_p}) = 4\pi^2 \tilde{a}_0^2 \int_{z_s}^{\infty} dz f(\vec{x}) f(\vec{x} + \vec{r}) \sum_p \varepsilon_{B_p} \int_{k_p}^{k_{p+1}} dk \frac{J_0(kr_\perp)}{k}, \quad (5.11)$$

where the ε_{B_p} are to be understood as the model parameter a_p for which the likelihood function $\mathcal{L}_{\vec{\Delta}}(a_p)$ has to be maximised given the Faraday data $\vec{\Delta}$.

5.2.2 Evaluation of the Likelihood Function

In order to maximise the likelihood function, Bond et al. (1998) approximate the likelihood function as a Gaussian of the parameters in regions close to the maximum $\vec{a} = \{a\}_{\max}$, where $\{a\}_{\max}$ is the set of model parameters which maximise the likelihood function. In this case, one can perform a Taylor expansion of $\ln \mathcal{L}_{\Delta}(\vec{a} + \delta\vec{a})$ about a_p and truncates at the second order in δa_p without making a large error.

$$\begin{aligned} \ln \mathcal{L}_{\Delta}(\vec{a} + \delta\vec{a}) &= \ln \mathcal{L}_{\Delta}(\vec{a}) + \sum_p \frac{\partial \ln \mathcal{L}_{\Delta}(\vec{a})}{\partial a_p} \delta a_p + \\ &\quad \frac{1}{2} \sum_{pp'} \frac{\partial^2 \ln \mathcal{L}_{\Delta}(\vec{a})}{\partial a_p \partial a_{p'}} \delta a_p \delta a_{p'} \end{aligned} \quad (5.12)$$

With this approximation, one can directly solve for the δa_p that maximise the likelihood function \mathcal{L}

$$\delta a_p = - \sum_{p'} \left(\frac{\partial^2 \ln \mathcal{L}_{\Delta}(\vec{a})}{\partial a_p \partial a_{p'}} \right)^{-1} \frac{\partial \ln \mathcal{L}_{\Delta}(\vec{a})}{\partial a_{p'}}, \quad (5.13)$$

where the first derivative is given by

$$\frac{\partial \ln \mathcal{L}_{\Delta}(\vec{a})}{\partial a_{p'}} = \frac{1}{2} \text{Tr} \left[(\Delta\Delta^T - C) \left(C^{-1} \frac{\partial C}{\partial a_{p'}} C^{-1} \right) \right] \quad (5.14)$$

and the second derivative is expressed by

$$\begin{aligned} \mathcal{F}_{pp'}^{(a)} &= - \left(\frac{\partial^2 \ln \mathcal{L}_{\Delta}(\vec{a})}{\partial a_p \partial a_{p'}} \right) = \text{Tr} \left[(\Delta\Delta^T - C) \left(C^{-1} \frac{\partial C}{\partial a_p} C^{-1} \frac{\partial C}{\partial a_{p'}} C^{-1} \right. \right. \\ &\quad \left. \left. - \frac{1}{2} C^{-1} \frac{\partial^2 C}{\partial a_p \partial a_{p'}} C^{-1} \right) \right] + \frac{1}{2} \text{Tr} \left(C^{-1} \frac{\partial C}{\partial a_p} C^{-1} \frac{\partial C}{\partial a_{p'}} \right), \end{aligned} \quad (5.15)$$

where Tr indicates the trace of a matrix. The second derivative is called the curvature matrix. If the covariance matrix is linear in the parameter a_p then the second derivatives of the covariance matrix $\partial^2 C / (\partial a_p \partial a_{p'})$ vanish. Note that for the calculation of the δa_p , the inverse curvature matrix $(\mathcal{F}_{pp'}^{(a)})^{-1}$ has to be calculated. The diagonal terms of the inverse curvature matrix $(\mathcal{F}_{pp'}^{(a)})^{-1}$ can be regarded as the errors $\sigma_{a_p}^2$ to the parameters a_p .

A suitable iterative algorithm to determine the power spectra would be to start with an initial guess of a parameter set a_p . Using this initial guess, the δa_p 's have to be calculated using Eq. (5.13). If the δa_p 's are not sufficiently close to zero, a new parameter set $a'_p = a_p + \delta a_p$ is used and again the $\delta a'_p$ are calculated and so on. This process can be stopped when $\delta a_p / \sigma_{a_p} \leq \epsilon$, where ϵ describes the required accuracy.

5.2.3 Binning and Rebinning

In the used parametrisation of the model given by Eq. (5.11) the bin size, i.e. the size of the interval $[k_p, k_{p+1}]$, is important. Since the power spectrum is measured,

equal bins on a logarithmic scale are chosen as initial binning. However, if the bins are too small then the cross correlation between two bins could be very high and the two bins cannot be regarded as independent anymore. Furthermore, the errors might be very large, and could be one order of magnitude larger than the actual values. In order to avoid such situations, it is preferable to chose either less bins or to rebin by adding two bins together. Note that this oversampling is not a real problem, since the model parameter covariance matrix takes care of the redundancy between data points. However, for computational efficiency and for a better display of the data to the human eye, a smaller set of mostly independent data points is preferable.

In order to find a criterion for rebinning, an expression for the cross correlation of two parameter a_p and $a_{p'}$ can be defined by

$$\delta_{pp'} = \frac{\langle \sigma_p \sigma_{p'} \rangle}{\langle \sigma_p \rangle \langle \sigma_{p'} \rangle} = \frac{\mathcal{F}_{pp'}^{-1}}{\sqrt{\mathcal{F}_{pp}^{-1} \mathcal{F}_{p'p'}^{-1}}}, \quad (5.16)$$

where the full range, $-1 \leq \delta_{pp'} \leq 1$, is possible but usually the correlation will be negative indicating anti-correlation. The used criterion for rebinning is to require that if the absolute value of the cross-correlation $|\delta_{pp'}|$ is larger than $\delta_{pp'}^{\max}$ for two bins p and p' then these two bins are added together in such a way that the magnetic energy $\sum_p \varepsilon_{B_p} * \Delta k_p$ is conserved.

After rebinning the algorithm starts again to iterate and finds the maximum with the new binning. This is done as long as the cross-correlation of two bins is larger than required.

5.2.4 The Algorithm

As a first guess for a set of model parameters ε_{B_i} , the results from a Fourier analysis of the original *RM* map employing the algorithms as described in Chapter 3 were used. However, one can also employ as first guess ε_{B_i} a simple power law $\varepsilon_{B_i} \propto k_i^\alpha$, where α is the spectral index. The results and the shape of the power spectrum did not change.

If not stated otherwise, an iteration is stopped when $\epsilon < 0.01$, i.e. the change in a parameter ε_{B_i} is smaller than 1% of the error in the parameter ε_{B_i} itself. Once the iteration converges to a final set of model parameters the cross-correlation between the bins is checked and if necessary, the algorithm will start a new iteration after rebinning. Throughout the rest of the chapter, a $|\delta_{pp'}| < 0.5$ for $p \neq p'$ is required.

Once the power spectra in terms of $\varepsilon_B(k) = \sum_p \varepsilon_{B_i} \mathbf{1}_{\{[k_p, k_{p+1}]\}}$ is determined, one can calculate the magnetic energy density ε_B by integration of the power spectrum

$$\varepsilon_B(a_p) = \int_0^\infty dk \varepsilon_B(k) = \sum_p \varepsilon_{B_i} \Delta k_p, \quad (5.17)$$

where $\Delta k_p = k_{p+1} - k_p$ is the binsize.

Also λ_B and λ_{RM} are accessible by integration of the power spectrum (see Chapter 3).

$$\lambda_B = \pi \frac{\int_0^\infty dk \varepsilon_B(k)/k}{\int_0^\infty dk \varepsilon_B(k)} = \pi \frac{\sum_p \varepsilon_{B_i} \ln(k_{p+1}/k_p)}{\sum_p \varepsilon_{B_i} \Delta k_p} \quad (5.18)$$

$$\lambda_{RM} = 2 \frac{\int_0^\infty dk \varepsilon_B(k)/k^2}{\int_0^\infty dk \varepsilon_B(k)/k} = 2 \frac{\sum_p \varepsilon_{B_i} (1/k_p - 1/k_{p+1})}{\sum_p \varepsilon_{B_i} \ln(k_{p+1}/k_p)}. \quad (5.19)$$

Since the method allows to calculate errors $\sigma_{\varepsilon_{B_i}}$, one can also determine errors for these integrated quantities. However, the cross-correlations $\delta_{pp'}$ which are non-zero as already mentioned, have to be taken into account. The probability distribution $P(\vec{a})$ of a parameter can often be described by a Gaussian

$$P(\vec{a}) \sim e^{-\frac{1}{2} \delta \vec{a}^T X^{-1} \delta \vec{a}}, \quad (5.20)$$

where X is the covariance matrix of the parameters, $\delta \vec{a} = \vec{a} - \vec{a}_{\text{peak}}$, $\vec{a} = \{a\}_{\text{max}}$ is the determined maximum value for the probability distribution and \vec{a}_{peak} is the actual maximum of the probability function. The standard deviation is defined as

$$\langle \delta \varepsilon_B^2 \rangle = \langle (\varepsilon_B(a) - \varepsilon_B)^2 \rangle = \int d^n a P(a) (\varepsilon_B(a) - \varepsilon_B)^2. \quad (5.21)$$

Assuming that $P(\vec{a})$ follows a Gaussian distribution (as done above in Eq. (5.20)) and using that $\varepsilon_B(a)$ is linear in the $a_p = \varepsilon_{B_i}$ then Eq. (5.21) becomes

$$\langle \delta \varepsilon_B^2 \rangle = \int d^n a P(a) \left[\delta a \frac{\partial \varepsilon_B}{\partial a_p} \right]^2 \quad (5.22)$$

$$= \int d^n a P(a) \sum_p \delta a_p \frac{\partial \varepsilon_B}{\partial a_p} \sum_{p'} \delta a_{p'} \frac{\partial \varepsilon_B}{\partial a_{p'}}. \quad (5.23)$$

Rearranging this equation and realising that the partial derivatives are independent on the a_p since ε_B is linear in the a_p 's this leads to

$$\langle \delta \varepsilon_B^2 \rangle = \sum_{pp'} \frac{\partial \varepsilon_B}{\partial a_p} \frac{\partial \varepsilon_B}{\partial a_{p'}} \int d^n a P(a) \delta a_p \delta a_{p'} \quad (5.24)$$

and finally using Eq. (5.16)

$$\langle \delta \varepsilon_B^2 \rangle = \sum_{pp'} \frac{\partial \varepsilon_B}{\partial a_p} \frac{\partial \varepsilon_B}{\partial a_{p'}} \langle \sigma_p \sigma_{p'} \rangle, \quad (5.25)$$

where $\langle \sigma_p \sigma_{p'} \rangle = \mathcal{F}_{pp'}^{-1}$

A similar argumentation can be applied to the error derivation for the correlation lengths λ_{RM} and λ_B , although the correlation lengths are not linear in the coefficients a_p . If one uses the partial derivatives at the determined maximum, one is still able to approximately separate them from the integral. This leads to the following expressions for their errors

$$\langle \delta \lambda_B^2 \rangle \approx \sum_{pp'} \frac{\partial \lambda_B}{\partial a_p} \Big|_{a_p^{\text{max}}} \frac{\partial \lambda_B}{\partial a_{p'}} \Big|_{a_{p'}^{\text{max}}} \langle \sigma_p \sigma_{p'} \rangle \quad (5.26)$$

and

$$\langle \delta \lambda_{RM}^2 \rangle \approx \sum_{pp'} \frac{\partial \lambda_{RM}}{\partial a_p} \Big|_{a_p^{\text{max}}} \frac{\partial \lambda_{RM}}{\partial a_{p'}} \Big|_{a_{p'}^{\text{max}}} \langle \sigma_p \sigma_{p'} \rangle. \quad (5.27)$$

5.3 Testing the Algorithm

In order to test the algorithm, the maximum likelihood estimator was applied to generated RM maps with a known magnetic power spectrum $\varepsilon_B(k)$. Eq. (3.31) gives a prescription for the relation between the amplitude of RM , $|\hat{RM}(k_\perp)|^2$, and the magnetic power spectrum in Fourier space.

$$\varepsilon_B^{\text{obs}}(k) = \frac{k^2}{a_1 A_\Omega (2\pi)^4} \int_0^{2\pi} d\phi |\hat{RM}(\vec{k}_\perp)|^2. \quad (5.28)$$

or

$$|\hat{RM}(k_\perp)|^2 = \frac{a_1 A_\Omega (2\pi)^3}{k^2} \varepsilon_B^{\text{obs}}(k), \quad (5.29)$$

where A_Ω is the area Ω for which RM 's are actually measured and $a_1 = a_0^2 n_{e0}^2 L$, where L is the characteristic depth of the Faraday screen.

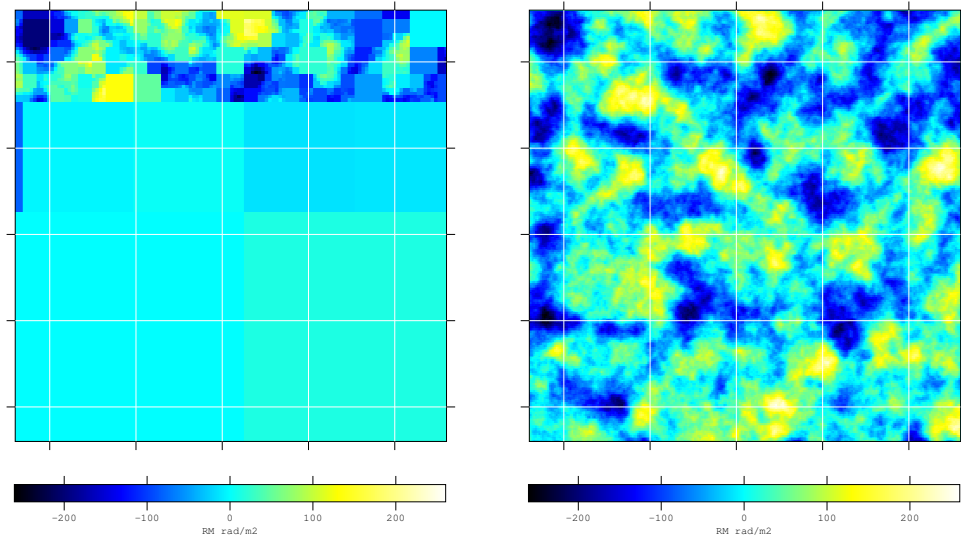


Figure 5.1: On the right panel, a small part (37×37 kpc) of a typical realisation of a RM map which is produced by a Kolmogorov like magnetic field power spectrum for $k \geq k_c = 0.8 \text{ kpc}^{-1}$ and a magnetic field strength of $5 \mu\text{G}$. On the left panel, the RM data used for the data matrix Δ_i is shown where arbitrary neighbouring points were averaged in order to reduce the number of independent points in a similar way as it is done later with the observational data.

As Faraday screen, a box with sides being 150 kpc long and a depth of $L = 300$ kpc is assumed. For the sake of simplicity, a uniform electron density profile is assumed with a density of $n_{e0} = 0.001 \text{ cm}^{-3}$. The magnetic field power spectrum used is expressed by

$$\varepsilon_B^{\text{obs}}(k) = \begin{cases} \frac{\varepsilon_B}{k_0^{1-\alpha} k_c^{2+\alpha}} k^2 & \forall k \leq k_c \\ \frac{\varepsilon_B}{k_0} \left(\frac{k}{k_0}\right)^{-5/3} & \forall k \geq k_c \end{cases}. \quad (5.30)$$

where the spectral index was set to mimic Kolmogorov turbulence with energy injection at $k = k_c$, and

$$\varepsilon_B = \frac{\langle B^2 \rangle}{8\pi} = \int_0^{k_{\max}} dk \varepsilon_B^{\text{obs}}(k), \quad (5.31)$$

where $k_{\max} = \pi/\Delta r$ is determined by the pixel size (Δr) of the used RM map. The latter equation combined with Eq. (5.30) gives the normalisation k_0 in such a way that the integration over the accessible power spectrum will result in a magnetic field strength of B for which $5 \mu\text{G}$ was used. Furthermore, a $k_c = 0.8 \text{ kpc}^{-1}$ was used.

In order to generate a RM map with the magnetic power spectrum $\varepsilon_B(k)$ for the chosen Faraday screen, the real and imaginary part of the Fourier space was filled independently with Gaussian deviates. Then these values were multiplied by the appropriate values given by Eq. (5.29) corresponding to their place in k -space. As a last step, an inverse Fourier transformation was performed. A typical realisation of such a generated RM map is shown in the right panel of Fig. 5.1.

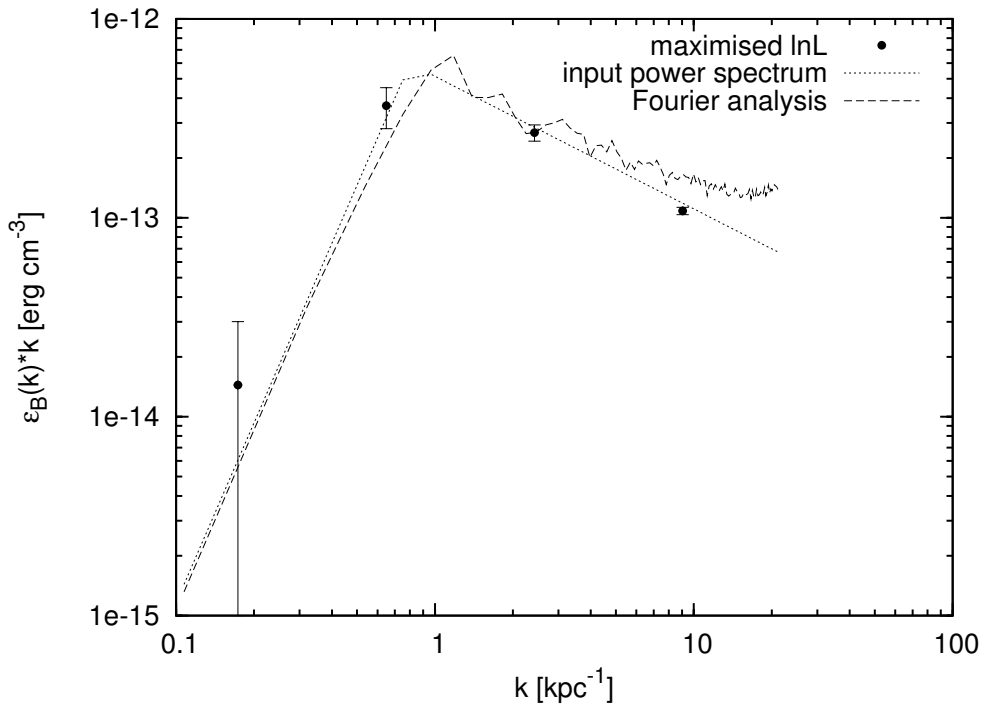


Figure 5.2: Power spectra for a simulated RM map as shown in Fig. 5.1. The input power spectra is shown in comparison to the one found by the Fourier analysis as described in Chapter 3 and the one which was derived by the maximum likelihood estimator developed here. One can clearly see the good agreement within one σ between input power spectrum and the power spectrum derived by the maximum likelihood method.

For the analysis of the resulting RM map only a small part of the initial map was used in order to reproduce the influence of the limited emission region of a radio source. A Fourier analysis as described in Chapter 3 was applied to this part. The resulting power spectrum is shown in Fig. 5.2 as dashed line in comparison with the input power spectrum as dotted line.

The maximum likelihood method is numerically limited by computational power since it involves matrix multiplication and inversion, where the latter is a N^3 process. Thus, not all points of the many which are defined in the maps can be used. However, it is desirable to use as much information as possible from the original map. Therefore, it was chose to randomly average neighbouring points with a scheme which let to a map with spatially inhomogeneously resolved cells. The resulting map is highly resolved on top and lowest on the bottom with some random deviations which makes it similarly to the error weighting of the observed data. $N = 1500$ independent points were used for the analysis. On the left panel of Fig. 5.1, the averaged RM map is shown which was used for the test.

As a first guess for the maximum likelihood estimator, the power spectra derived by the Fourier analysis was used. The resulting power spectrum is shown as filled circles with $1\text{-}\sigma$ error bars in Fig. 5.2. As can be seen from this figure, the input power spectrum and the power spectrum derived by the maximum likelihood estimator agree well within the one σ level. Integration over this power spectrum results in a field strength of $(4.7 \pm 0.3)\mu\text{G}$ in agreement with the input magnetic field strength of $5\mu\text{G}$.

5.4 Application to Hydra A

5.4.1 The Data Δ

The maximum likelihood estimator which was introduced and tested in the last sections is applied in the following to the Faraday rotation map of the north lobe of the radio source Hydra A (Taylor & Perley 1993). The data were kindly provided by Greg Taylor.

For this purpose, a high fidelity RM map was used which was presented in Chapter 4 and was generated by the developed algorithm *Pacman* using the original polarisation data. *Pacman* also provides error maps σ_i by error propagation of the instrumental uncertainties of polarisation angles. The *Pacman* map which was used is shown in the right panel of Fig. 5.3.

For the same reasons as mentioned in Sect. 5.3, the data were averaged. An appropriate averaging procedure using error weighting was applied such that

$$\overline{RM}_i = \frac{\sum_j RM_j / \sigma_j^2}{\sum_j 1 / \sigma_j^2}, \quad (5.32)$$

and the error calculates as

$$\sigma_{\overline{RM}_i}^2 = \frac{\sum_j (1 / \sigma_j^2)}{(\sum_j 1 / \sigma_j^2)^2} = \frac{1}{\sum_j 1 / \sigma_j^2}. \quad (5.33)$$

Here, the sum goes over the set of old pixels $\{j\}$ which form the new pixels $\{i\}$. The corresponding pixel coordinates $\{i\}$ were also determined by applying an error weighting scheme

$$\bar{x}_i = \frac{\sum_j x_j / \sigma_j^2}{\sum_j 1 / \sigma_j^2} \quad \text{and} \quad \bar{y}_i = \frac{\sum_j y_j / \sigma_j^2}{\sum_j 1 / \sigma_j^2}. \quad (5.34)$$

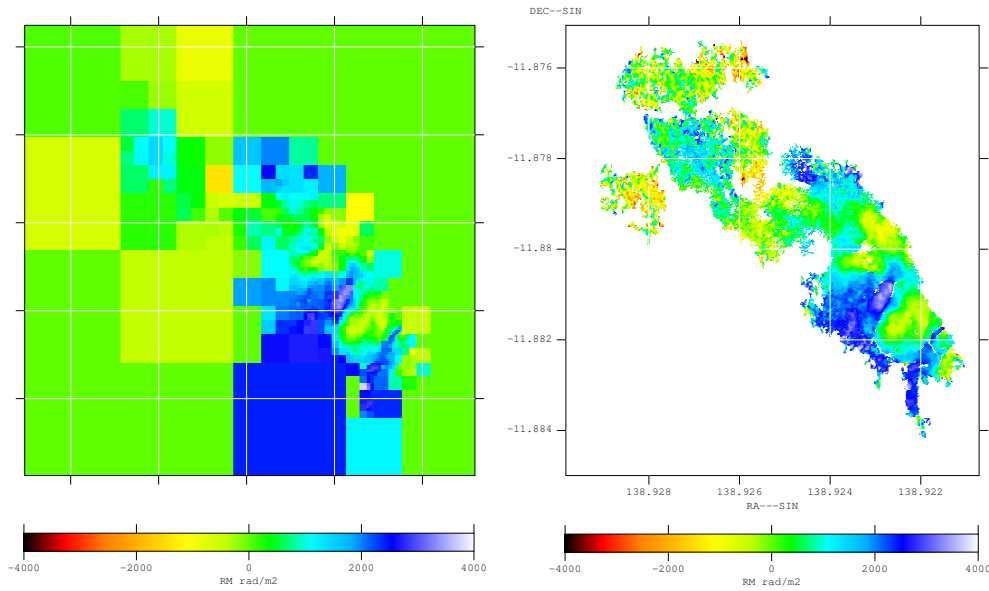


Figure 5.3: The final RM map from the north lobe of Hydra A which was analysed with the maximum likelihood estimator; right: original *Pacman* map, left: error weighted map. Note that the small scale noise for the diffuse part of the lobe is averaged out and only the large scale information carried by this region is maintained. Furthermore, note that each pixel has also a (not displayed) error weighted position.

The analysed RM map was determined by a gridding procedure. The original RM map was divided into four equally sized cells. In each of these the original data were averaged as described above. Then the cell with the smallest error was chosen and again divided into four equally sized cells and the original data contained in the so determined cell were averaged. The last step was repeated until the number of cells reached a defined value N . It was decided to use $N = 1500$. This is partly due to the limitation by computational power but also partly because of the desired suppression of small scale noise by a strong averaging of the noisy regions.

The final RM map which was analysed is shown in the left panel of Fig. 5.3. The most noisy regions in Hydra A are located in the coarsely resolved northernmost part of the lobe. It was chosen not to resolve this region any further but to keep the large-scale information which is carried by this region.

5.4.2 The Window Function

As mentioned in Sect. 5.2.1, the window function describes the sampling volume and, thus, one has to find a suitable description for it based on Eq. (5.6). Hydra A (or 3C218) is located at a redshift of 0.0538 (de Vaucouleurs et al. 1991). For the derivation of the electron density profile parameter, the work by Mohr et al. (1999) was used which was done for ROSAT PSPC data while using the deprojection of X-ray surface brightness profiles as described in the Appendix A of Pfrommer & Enßlin (2004). Since Hydra A is known to exhibit a strong cooling flow as observed in the X-ray studies, a double β -

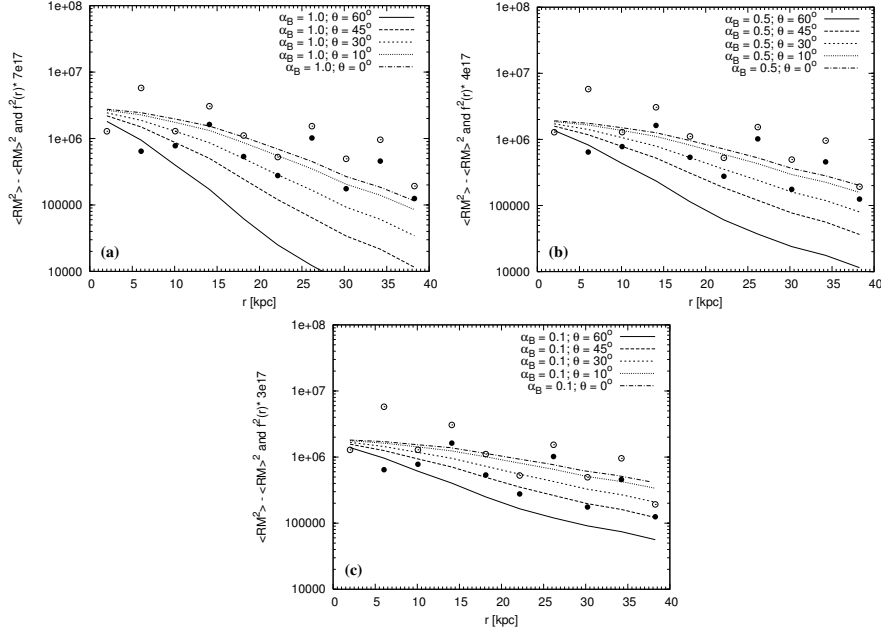


Figure 5.4: The comparison between the integrated squared window function $f^2(r)$ (lines) with the RM dispersion function $\langle RM^2(r) \rangle$ (open circles) and $\langle RM^2 \rangle - \langle RM(r) \rangle^2$ (filled circles). Different models for the window function were assumed. In (a) $\alpha_B = 1.0$, in (b) $\alpha_B = 0.5$ and in (c) $\alpha_B = 0.1$ were used, where the inclination angle θ of the source was varied. It can be seen that models for the window function with $\alpha_B = 0.1 \dots 0.5$ and $\theta = 10^\circ \dots 50^\circ$ match the shape of the dispersion function very well.

profile was assumed¹ and for the inner profile $n_{e1}(0) = 0.056 \text{ cm}^{-3}$ and $r_{c1} = 0.53$ arcmin was used while for the outer profile $n_{e2}(0) = 0.0063 \text{ cm}^{-3}$ and $r_{c2} = 2.7$ arcmin and a $\beta = 0.77$ was applied.

Assuming this electron density profile to be accurately determined, there are two other parameters which enter in the window function. The first one is related to the source geometry. For Hydra A, a clear depolarisation asymmetry between the two lobes is observed known as the Laing-Garrington effect (Garrington et al. 1988; Laing 1988) suggesting that the source is tilted against the xy -plane (Taylor & Perley 1993). In fact, the north lobe points towards the observer. In order to take this into account, an angle θ was introduced which describes the angle between the source and the xy -plane such that the north lobe points towards the observer. Taylor & Perley (1993) determine an inclination angle of $\theta = 45^\circ$.

The other parameter is related to the global magnetic field distribution which is assumed to scale with the electron density profile $B(r) \propto n_e(r)^{\alpha_B}$. In a scenario in which an originally statistically homogeneously magnetic energy density gets adiabatically compressed, one expects $\alpha_B = 2/3$. If the ratio of magnetic and thermal

¹defined as $n_e(r) = [n_{e1}^2(0)(1 + (r/r_{c1})^2)^{-3\beta} + n_{e2}^2(0)(1 + (r/r_{c2})^2)^{-3\beta}]^{1/2}$.

pressure is constant throughout the cluster then $\alpha_B = 0.5$. However, α_B might have any other value. Dolag et al. (2001) determined an $\alpha_B = 0.9$ for the outer regions of the cluster Abell 119.

In order to constrain the applicable ranges of these quantities, one can compare the integrated squared window function with the RM dispersion function $\langle RM(r_\perp)^2 \rangle$ of the RM map used since

$$\langle RM^2(r_\perp) \rangle \propto \int_{-\infty}^{\infty} dz f^2(r_\perp, z), \quad (5.35)$$

as stated by Eq. (3.39). Therefore, the shape of the two functions was compared. The result is shown in Fig. 5.4. For the window function, three different $\alpha_B = 0.1, 0.5, 1.0$ were used and for each of these, five different inclination angles $\theta = 0^\circ, 10^\circ, 30^\circ, 45^\circ$ and 60° were employed, although the $\theta = 0^\circ$ is not very likely considering the observational evidence of the Laing-Garrington effect as observed in Hydra A by Taylor & Perley (1993). The different results are plotted as lines of different style in Fig. 5.4. The filled and open dots represent the RM dispersion function. The solid circles indicate the binned $\langle RM^2 \rangle$ function. The open circles represent the binned $\langle RM^2 \rangle - \langle RM \rangle^2$ function, which is cleaned from any foreground RM signals.

From Fig. 5.4, it can be seen that models with $\alpha_B = 1.0$ or $\theta > 50^\circ$ are not able to recover the shape of the RM dispersion function and, thus, one expects $\alpha_B < 1.0$ and $\theta < 50^\circ$ to be more likely.

5.5 Results and Discussion

Based on the described treatment of the data and the description of the window function, first the power spectra for various scaling exponents α_B were calculated while keeping the inclination angle at $\theta = 45^\circ$. For this investigation, the number of bins was chosen to be $n_l = 5$ which proved to be sufficient. For these calculations, $\epsilon < 0.1$ was used. The resulting power spectra are plotted in Fig. 5.5.

In Fig. 5.5, one can clearly see that the power spectrum derived for $\alpha_B = 1.0$ has a completely different shape whereas the other power spectra show only slight deviation from each other and are vertically displaced implying different normalisation factors, i.e. central magnetic field strengths which increase with increasing α_B . The straight dashed line which is also plotted in Fig. 5.5 indicates a Kolmogorov like power spectrum being equal to $5/3$ in the prescription used. One can clearly see, that the power spectra follow this slope over at least on order of magnitude.

In Sect. 5.4.2, it was not possible to distinguish between the various scenarios for α_B although it was found that an $\alpha_B = 1$ does not properly reproduce the measured RM dispersion. However, the likelihood function offers the possibility to calculate the actual probability of a set of parameters given the data (see Eq. (5.1)). Thus, the log likelihood $\ln \mathcal{L}_\Delta(\vec{a})$ value was calculated for various power spectra derived for the different window functions varying in the scaling exponent α_B and assuming the inclination angle of the source to be for all geometries $\theta = 45^\circ$. In Fig. 5.6, the log likelihood is shown in dependence on the used scaling parameter α_B .

As can be clearly seen from Fig. 5.6, there is a plateau of most likely scaling exponents α_B ranging from 0.1 to 0.8. An $\alpha_B = 1$ seems to be very unlikely for the

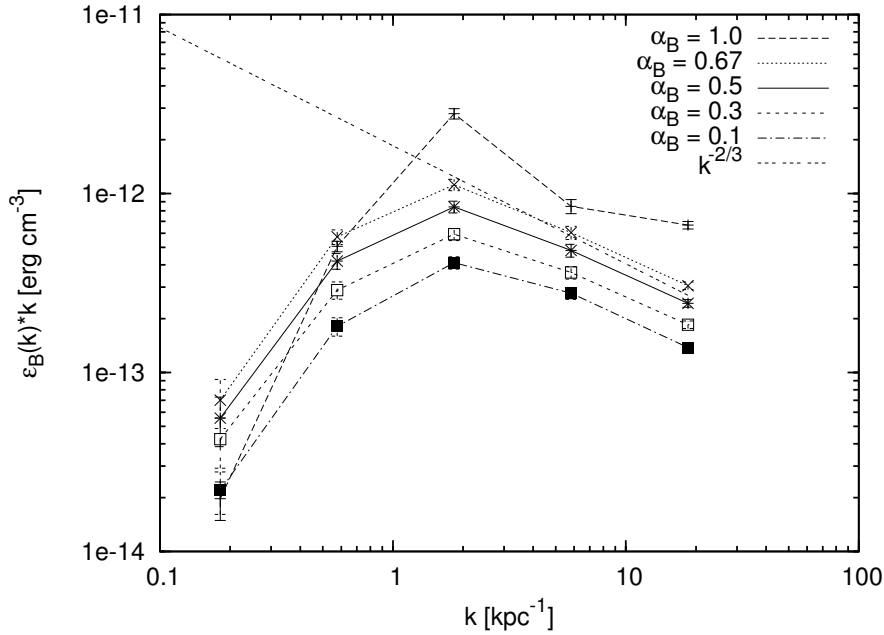


Figure 5.5: Power spectra for $N = 1500$ and $n_l = 5$ are presented. Different exponents α_B in the relation $B(r) \sim n_e(r)^{\alpha_B}$ of the window function were used. The inclination angle of the source was chosen to be $\theta = 45^\circ$.

model used as already deduced in Sect. 5.4.2. The sudden decrease for $\alpha_B < 0.1$ might be due to non-Gaussian effects. The magnetic field strength derived for this plateau region ranges from $9 \mu\text{G}$ to $5 \mu\text{G}$. The correlation length of the magnetic field λ_B was determined to range between 2.5 kpc and 3.0 kpc whereas the RM correlation length was determined to be in the range of 4.5...5.0 kpc. These ranges have to be considered as a systematic uncertainty since one is not yet able to distinguish between these scenarios observationally. Another systematic effect might be given by uncertainties in the electron density itself. Varying the electron density normalisation parameters ($n_{e1}(0)$ and $n_{e2}(0)$) leads to a vertical displacement of the power spectrum while keeping the same shape.

In order to study the influence of the inclination angle on the power spectrum, an $\alpha_B = 0.5$ was used being in the middle of the most likely region derived. Furthermore for this calculations, smaller bins were used and thus, the number of bins was increased to $n_l = 8$. The power spectrum was calculated for two different inclination angles $\theta = 30^\circ$ and $\theta = 45^\circ$. The results are shown in Fig. 5.7 in comparison with a Kolmogorov like power spectrum.

As can be seen from Fig. 5.7, the power spectra derived agree well with a Kolmogorov like power spectrum over at least one order of magnitude. For the inclination angle of $\theta = 30^\circ$, the following field and map properties were derived $B = 5.7 \pm 0.1 \mu\text{G}$, $\lambda_B = 3.1 \pm 0.3 \text{ kpc}$ and $\lambda_{RM} = 6.7 \pm 0.7 \text{ kpc}$. For $\theta = 45^\circ$, it was calculated $B = 7.3 \pm 0.2 \mu\text{G}$, $\lambda_B = 2.8 \pm 0.2 \text{ kpc}$ and $\lambda_{RM} = 5.2 \pm 0.5 \text{ kpc}$. The value of the log likelihood $\ln \mathcal{L}$ was determined to be slightly higher for the inclination angle of $\theta = 30^\circ$. The flattening of the power spectra for large k 's can be explained by

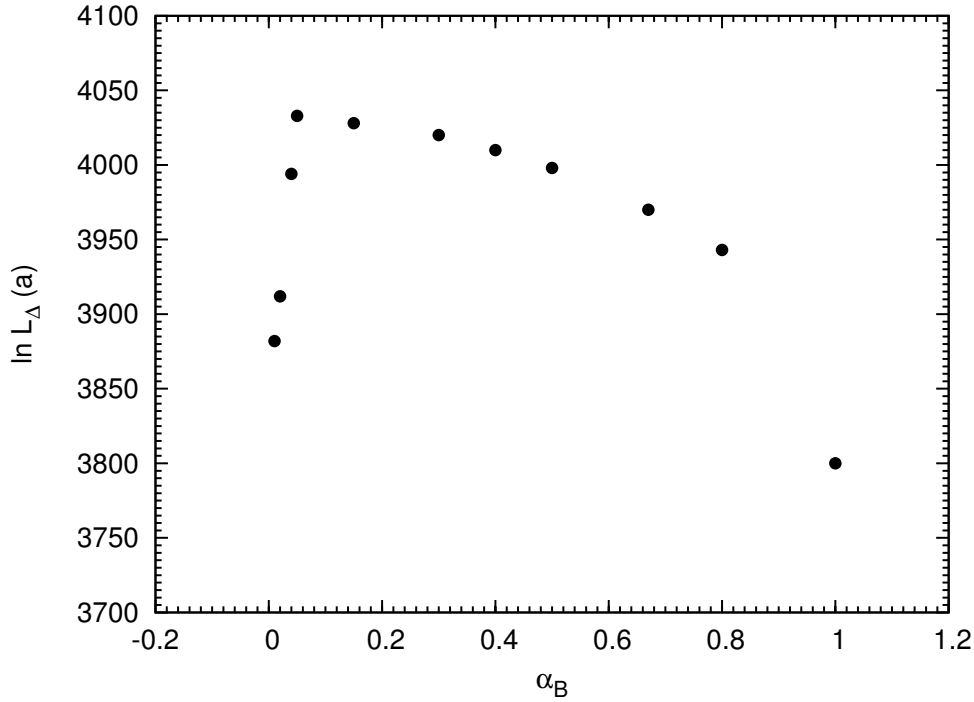


Figure 5.6: The log likelihood $\ln \mathcal{L}_{\Delta}(\vec{a})$ of various power spectra assuming different α_B while using a constant inclination angle $\theta = 45^\circ$ is shown. One can clearly see that $\alpha_B = 0.1 \dots 0.8$ are in the plateau of maximum likelihood. The sudden decrease for $\alpha_B < 0.1$ in the likelihood might be due to non-Gaussian effects becoming too strong.

small scale noise which was not modelled separately.

Although the central magnetic field strength decreases with decreasing scaling parameter α_B , the volume integrated magnetic field energy E_B within the cluster core radius r_{c2} increases. The volume integrated magnetic field energy E_B calculates as follows

$$E_B = 4\pi \int_0^{r_{c2}} dr r^2 \frac{B^2(r)}{8\pi} = \frac{B_0^2}{2} \int_0^{r_{c2}} dr r^2 \left(\frac{n_e(r)}{n_{e0}} \right)^{2\alpha_B}, \quad (5.36)$$

where it is integrated from the cluster centre to the core radius r_{c2} of the second, the non-cooling flow, component of the electron density distribution.

The magnetic field profile was integrated for the various scaling parameters and the corresponding field strengths which were determined by the maximum likelihood estimator. The result is plotted in Fig. 5.8. The higher magnetic energies for the smaller scaling parameters which correspond to smaller central magnetic field strengths are due to the higher field strengths in the outer parts of the cool cluster core. This effect would be much more drastic if one had extrapolated the scaling $B(r) \propto n_e(r)^{\alpha_B}$ to larger cluster radii and integrated over a larger volume.

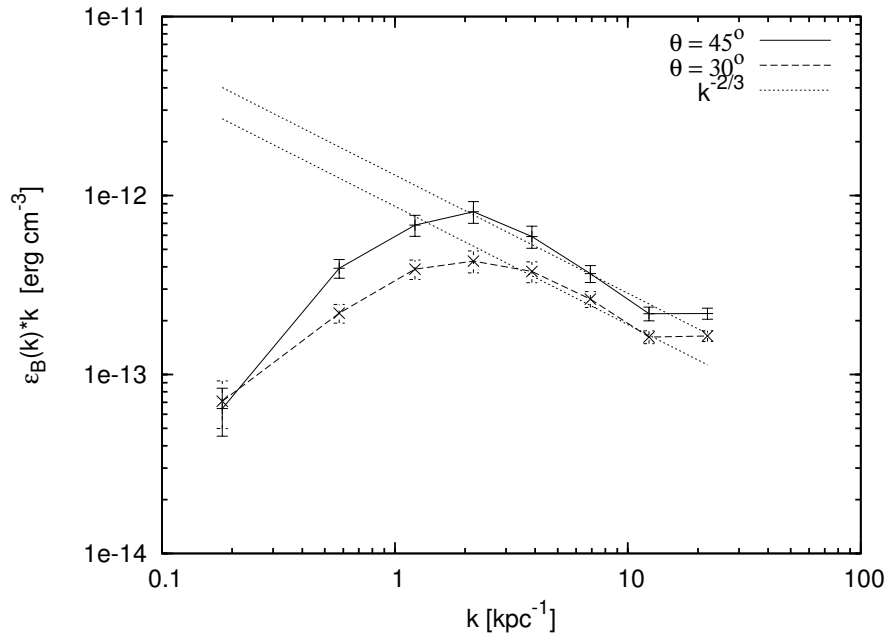


Figure 5.7: Power Spectra for two different inclination angles $\theta = 30^\circ$ and $\theta = 45^\circ$ and an $\alpha_B = 0.5$ are shown. For comparison a Kolmogorov like power spectrum is plotted as straight dashed line. One can clearly see that the calculated power spectra follow such a power spectrum over at least one order of magnitude. Note that the error bars are larger than in Fig. 5.5 because smaller bin size were used.

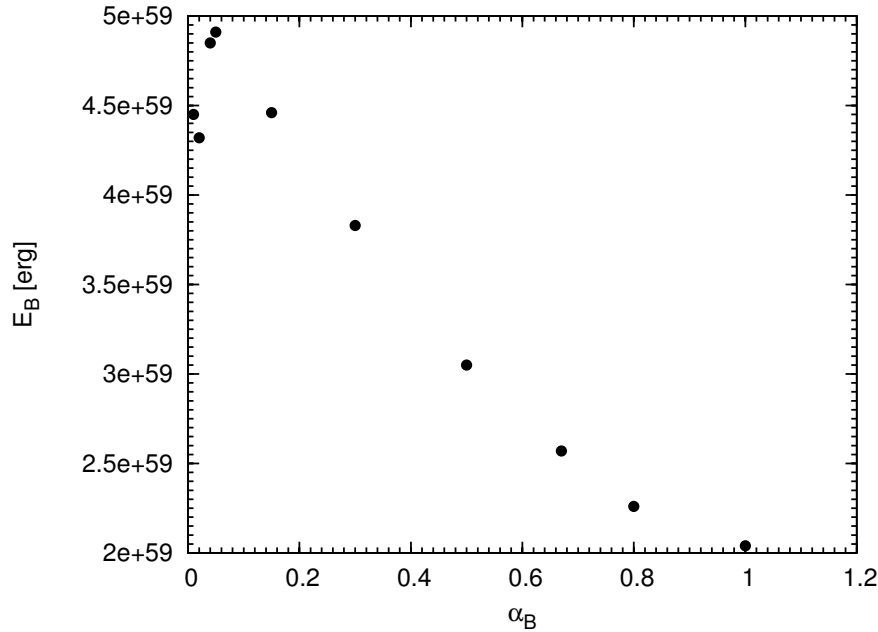


Figure 5.8: The integrated magnetic field energy E_B within the cluster core radius r_{c2} for the various scaling parameters α_B also used in Fig. 5.6 and the corresponding central magnetic field strengths B_0 as determined by the maximum likelihood estimator.

5.6 Conclusions

A maximum likelihood estimator was presented for the determination of cluster magnetic field power spectra from RM maps of extended polarised radio sources. The covariance matrix for RM was introduced under the assumption of statistically homogeneously distributed magnetic fields throughout the Faraday screen. The approach was successfully tested on simulated RM maps with known power spectra.

This approach was applied to the RM map of the north lobe of Hydra A. Different power spectra were calculated for various window functions being especially influenced by the scaling parameter between electron density profile and global magnetic field distribution and the inclination angle of the emission region. The scaling parameter α_B was determined to be most likely in the range of $0.1 \dots 0.8$.

It was realised that there is a systematic uncertainty in the values calculated due to the uncertainty in the window parameters itself. Taking this into account, a central magnetic field strength in the Hydra A cluster of $B = (7 \pm 2) \mu\text{G}$ was deduced and for the magnetic field correlation length was determined to be $\lambda_B = (3.0 \pm 0.5)$ kpc. If the geometry uncertainties could be removed the remaining statistical errors are an order of one magnitude smaller. The difference of these values from the ones found in an earlier analysis of the same dataset of Hydra A which yielded $B = 12 \mu\text{G}$ and $\lambda_B = 1$ kpc (Chapter 3) is a result of the improved RM map using the *Pacman* algorithm (Chapter 4) and a better knowledge of the magnetic cluster profile, i.e. here $\alpha_B \approx 0.5$ (instead of $\alpha_B = 1.0$ in Chapter 3).

The cluster magnetic field power spectrum of Hydra A follows a Kolmogorov like power spectrum over at least one order of magnitude. However, the analysis reveals that there is a dominant scale ~ 3 kpc on which the magnetic power is concentrated.

Conclusions

This work was aimed to understand observational multi-frequency polarisation data sets of extended extragalactic radio sources, their reduction resulting in Faraday rotation maps and the statistical characterisation and analyses of these maps in order to study the properties of the magnetic fields which are associated with the plasma in clusters of galaxies.

Since it is sometimes debated which magnetised medium is mainly responsible for the Faraday rotation, investigations aimed to solve this problem provided confidence that the Faraday rotation is mainly due to the magnetised medium which is external to the source - the intra-cluster gas. In order to gain insight into the cluster magnetic field properties, a statistical approach to analyse the Faraday rotation maps in terms of autocorrelation function and power spectrum was developed and applied to the data. Realising that map making artefacts and noise in the data have a noticeable effect on this analysis, especially for measuring power spectra, a new RM map making algorithm called *Pacman* was introduced. *Pacman* provides high quality RM maps which allows precise estimates of power spectra. In order to use the full potential of these maps, an accurate power spectrum estimator based on Bayesian maximum likelihood methods was developed and successfully applied to characterise cluster magnetic field properties such as magnetic field strength, magnetic field autocorrelation length, and the shape of the magnetic power spectrum.

In this work, it was investigated if there is evidence for co-aligned structures in RM and φ_0 maps of extended radio sources in galaxy clusters. Such structures would strongly argue for source-local RM generating magnetic fields. In the course of this investigation, a *gradient alignment statistic* was introduced which reveals φ_0 and RM correlations regardless of whether there are source intrinsic or due to artefacts in the observation or in the RM map making process. In order to identify map making artefacts, a *gradient vector product statistic* was introduced. Both are valuable indicators of potential problems for RM based ICM magnetic field estimates.

Applying these two statistics to Faraday studies of extended radio sources (i.e. PKS 1246-410, Cygnus A, Hydra A, and 3C465) does not reveal any significant large scale co-alignment leading together with independent pieces of evidence to the conclusion that the RM generating magnetic fields are external to the source and thus, are associated with the cluster gas.

A statistical analysis of RM measurements in terms of correlation functions and equivalently power spectra was developed in order to estimate magnetic field strengths and autocorrelation lengths. This analysis relies on the assumption that the magnetic fields are statistically isotropically distributed throughout the Faraday screen. A window function describing the sampling volume was introduced through which any vir-

tually statistically homogeneous magnetic field can be thought to be observed.

The RM maps of three radio sources (i.e. 3C75 in Abell 400, 3C465 in Abell 2634 and Hydra A in Abell 780) were reanalysed using this method. Power spectra were successfully calculated and magnetic field strengths of $1 \dots 12 \mu\text{G}$ were derived for all three clusters. However, it was found that while this analysis is not suitable for the determination of differential parameters, such as the spectral slopes of power spectra, directly from the Fourier transformed map, the integrated quantities such as the magnetic field strength appears feasible. Furthermore, this analysis is not able to separate the influence of noise on the maps from the astrophysically interesting signal of intra-cluster magnetic fields.

In order to reduce map making artefacts, a new algorithm – *Pacman* – for the calculation of Faraday rotation maps from multi-frequency polarisation data sets was developed. By means of several statistical tests, it was shown that the new algorithm *Pacman* is robust and that it calculates reliable RM maps that suffer less from artefacts. Any statistical analysis will profit from this improvement.

Motivated by the recent success of Bayesian maximum likelihood methods in the determination of power spectra, a maximum likelihood estimator for the analysis of high quality RM maps was developed. It again assumes that the magnetic fields are statistically homogeneously distributed throughout the Faraday screen. It also allows to calculate the statistical uncertainty of any result. Furthermore, this maximum likelihood method takes the limited sampling size properly into account and thus, makes the determination of spectral slopes of power spectra possible.

The maximum likelihood estimator was applied to the *Pacman* RM map of the north lobe of Hydra A. Taking the uncertainty in the geometry of the Faraday screen into account, the central magnetic field strength for Hydra A was determined to be $7 \pm 2 \mu\text{G}$. The calculated power spectrum follows a Kolmogorov like power spectrum over at least one order of magnitude in k -space. The analysis reveals that there is a dominant scale ~ 3 kpc on which the power is concentrated.

This work will be continued in two directions, observationally and theoretically:

- The developed methods will be applied to further existing and upcoming high quality RM data sets in order to gain a statistical sample of cluster field measurements.
- The gained observational information will be used to understand magnetic field generating mechanisms in clusters of galaxies such as turbulent magnetic dynamos and galactic outflows.

Bibliography

- Allen, S. W., Taylor, G. B., Nulsen, P. E. J., et al. 2001, *Mon. Not. Roy. Astron. Soc.*, 324, 842
- Ballarati, B., Feretti, L., Ficarra, A., et al. 1981, *Astron. & Astrophys.*, 100, 323
- Beck, R. 2001, *Space Science Rev.*, 99, 243
- Beck, R., Brandenburg, A., Moss, D., Shukurov, A., & Sokoloff, D. 1996, *Ann. Rev. Astron. & Astrophys.*, 34, 155
- Bevington, P. R. & Robinson, D. K. 2003, Data reduction and error analysis for the physical sciences (Data reduction and error analysis for the physical sciences, 3rd ed., by Philip R. Bevington, and Keith D. Robinson. Boston, MA: McGraw-Hill, ISBN 0071199268, 2003.)
- Bicknell, G. V., Cameron, R. A., & Gingold, R. A. 1990, *Astrophys. Journ.*, 357, 373
- Bolton, J. G. & Wild, J. P. 1957, *Astrophys. Journ.*, 125, 296
- Bond, J. R., Jaffe, A. H., & Knox, L. 1998, *Phys. Rev. D*, 57, 2117
- Bourke, T. L. & Goodman, A. A. 2004, ArXiv:astro-ph/0401281
- Brentjens, M. A. & de Bruyn, A. G. 2004, in The Riddle of Cooling Flows in Galaxies and Clusters of galaxies
- Bridle, A. H. & Fomalont, E. B. 1976, *Astron. & Astrophys.*, 52, 107
- Burbidge, G. R. 1956, *Astrophys. Journ.*, 124, 416
- Burn, B. J. 1966, *Mon. Not. Roy. Astron. Soc.*, 133, 67
- Burns, J. O., Roettiger, K., Pinkney, J., et al. 1995, *Astrophys. Journ.*, 446, 583
- Carilli, C. L. & Taylor, G. B. 2002, *Ann. Rev. Astron. & Astrophys.*, 40, 319
- Cavaliere, A. & Fusco-Femiano, R. 1976, *Astron. & Astrophys.*, 49, 137
- Clarke, T. E. & Enßlin, T. A. 2001, in Clusters of Galaxies and the High Redshift Universe Observed in X-rays
- Clarke, T. E., Kronberg, P. P., & Böhringer, H. 2001, *Astrophys. Journ. Let.*, 547, L111

- Conway, R. G. & Strom, R. G. 1985, *Astron. & Astrophys.*, 146, 392
- Crusius-Waetzell, A. R., Biermann, P. L., Schlickeiser, R., & Lerche, I. 1990, *Astrophys. Journ.*, 360, 417
- D'Agostini, G. 2003, *Reports of Progress in Phys.*, 66, 1383
- David, L. P., Nulsen, P. E. J., McNamara, B. R., et al. 2001, *Astrophys. Journ.*, 557, 546
- Davis, L. J. & Greenstein, J. L. 1951, *Astrophys. Journ.*, 114, 206
- de Bruyn, A. G. 1996, *Tech. Rep. NFRA Note*, 655, ASTRON, Dwingeloo
- de Vaucouleurs, G., de Vaucouleurs, A., Corwin, H. G., et al. 1991, Third Reference Catalogue of Bright Galaxies (Volume 1-3, XII, Springer-Verlag Berlin Heidelberg New York)
- Dolag, K., Bartelmann, M., & Lesch, H. 1999, *Astron. & Astrophys.*, 348, 351
- Dolag, K., Bartelmann, M., & Lesch, H. 2002, *Astron. & Astrophys.*, 387, 383
- Dolag, K., Schindler, S., Govoni, F., & Feretti, L. 2001, *Astron. & Astrophys.*, 378, 777
- Dolag, K., Vogt, C., & Enßlin, T. A. 2004, ArXiv:astro-ph/0401214
- Dreher, J. W., Carilli, C. L., & Perley, R. A. 1987, *Astrophys. Journ.*, 316, 611
- Eilek, J. A. & Owen, F. N. 2002, *Astrophys. Journ.*, 567, 202
- Enßlin, T. A., Biermann, P. L., Klein, U., & Kohle, S. 1998, *Astron. & Astrophys.*, 332, 395
- Enßlin, T. A. & Gopal-Krishna. 2001, *Astron. & Astrophys.*, 366, 26
- Enßlin, T. A. & Hansen, S. H. 2004, ArXiv:astro-ph/0401337
- Enßlin, T. A., Lieu, R., & Biermann, P. L. 1999, *Astron. & Astrophys.*, 344, 409
- Enßlin, T. A. & Vogt, C. 2003, *Astron. & Astrophys.*, 401, 835
- Enßlin, T. A., Vogt, C., Clarke, T. E., & Taylor, G. B. 2003, *Astrophys. Journ.*, 597, 870
- Felten, J. E. 1996, in ASP Conf. Ser. 88: Clusters, Lensing, and the Future of the Universe, 271
- Feretti, L. 1999, in Diffuse Thermal and Relativistic Plasma in Galaxy Clusters, 3
- Feretti, L., Boehringer, H., Giovannini, G., & Neumann, D. 1997, *Astron. & Astrophys.*, 317, 432
- Feretti, L., Dallacasa, D., Giovannini, G., & Tagliani, A. 1995, *Astron. & Astrophys.*, 302, 680

- Feretti, L., Dallacasa, D., Govoni, F., et al. 1999a, *Astron. & Astrophys.*, 344, 472
- Feretti, L., Perley, R., Giovannini, G., & Andernach, H. 1999b, *Astron. & Astrophys.*, 341, 29
- Fusco-Femiano, R., Dal Fiume, D., De Grandi, S., et al. 2000, *Astrophys. Journ. Let.*, 534, L7
- Fusco-Femiano, R., dal Fiume, D., Feretti, L., et al. 1999, *Astrophys. Journ. Let.*, 513, L21
- Fusco-Femiano, R., Dal Fiume, D., Orlandini, M., et al. 2001, *Astrophys. Journ. Let.*, 552, L97
- Fusco-Femiano, R., Orlandini, M., Brunetti, G., et al. 2004, *Astrophys. Journ. Let.*, 602, L73
- Garrington, S. T. & Conway, R. G. 1991, *Mon. Not. Roy. Astron. Soc.*, 250, 198
- Garrington, S. T., Leahy, J. P., Conway, R. G., & Laing, R. A. 1988, *Nature*, 331, 147
- Ge, J. P. & Owen, F. N. 1993, *Astron. Journ.*, 105, 778
- Ginzburg, V. L. & Syrovatskii, S. I. 1964, *The Origin of Cosmic Rays (The Origin of Cosmic Rays, New York: Macmillan, 1964)*
- Giovannini, G., Feretti, L., & Stanghellini, C. 1991, *Astron. & Astrophys.*, 252, 528
- Giovannini, G., Tordi, M., & Feretti, L. 1999, *New Astronomy*, 4, 141
- Giovannini, M. 2004, *International Journal of Modern Physics D*, 13, 391
- Goldshmidt, O. & Rephaeli, Y. 1993, *Astrophys. Journ.*, 411, 518
- Govoni, F., Feretti, L., Giovannini, G., et al. 2001a, *Astron. & Astrophys.*, 376, 803
- Govoni, F., Feretti, L., Murgia, M., et al. 2002, in *ASP Conf. Series: Matter and Energy in Clusters of Galaxies*, arXiv:astro-ph/0211292
- Govoni, F., Taylor, G. B., Dallacasa, D., Feretti, L., & Giovannini, G. 2001b, *Astron. & Astrophys.*, 379, 807
- Hale, G. E. 1908, *Astrophys. Journ.*, 28, 315
- Han, J. L., Manchester, R. N., & Qiao, G. J. 1999, *Mon. Not. Roy. Astron. Soc.*, 306, 371
- Harris, D. E. & Grindlay, J. E. 1979, *Mon. Not. Roy. Astron. Soc.*, 188, 25
- Haves, P. 1975, *Mon. Not. Roy. Astron. Soc.*, 173, 553
- Heiles, C. 1990, in *IAU Symp. 140: Galactic and Intergalactic Magnetic Fields*, 35–40
- Hunstead, R. W. & The Sumss Team. 1999, in *Diffuse Thermal and Relativistic Plasma in Galaxy Clusters*, 19–23

- Ikebe, Y., Makishima, K., Ezawa, H., et al. 1997, *Astrophys. Journ.*, 481, 660
- Jackson, J. D. 1975, *Classical electrodynamics* (New York: Wiley, 1975, 2nd ed.)
- Jaffe, W. 1980, *Astrophys. Journ.*, 241, 925
- Johnson, R. A., Leahy, J. P., & Garrington, S. T. 1995, *Mon. Not. Roy. Astron. Soc.*, 273, 877
- Johnston-Hollitt, M., Ekers, R. D., & Hunstead, R. W. 2003, The Cosmic Cauldron, 25th meeting of the IAU, Joint Discussion 10, 18 July 2003, Sydney, Australia, 10
- Kaiser, N. 2003, Lecture Notes, available at <http://www.ifa.hawaii.edu/kaiser/lectures/>
- Kassim, N. E., Clarke, T. E., Enßlin, T. A., Cohen, A. S., & Neumann, D. M. 2001, *Astrophys. Journ.*, 559, 785
- Kempner, J. C. & Sarazin, C. L. 2001, *Astrophys. Journ.*, 548, 639
- Kim, K.-T., Kronberg, P. P., Dewdney, P. E., & Landecker, T. L. 1990, *Astrophys. Journ.*, 355, 29
- Kim, K.-T., Kronberg, P. P., & Tribble, P. C. 1991, *Astrophys. Journ.*, 379, 80
- Kolatt, T. 1998, *Astrophys. Journ.*, 495, 564
- Kronberg, P. P. 1994, *Reports of Progress in Physics*, 57, 325
- Laing, R. A. 1988, *Nature*, 331, 149
- Lane, W. M., Clarke, T. E., Taylor, G. B., Perley, R. A., & Kassim, N. E. 2004, *Astron. Journ.*, 127, 48
- Lawler, J. M. & Dennison, B. 1982, *Astrophys. Journ.*, 252, 81
- Leahy, J. P. 1991, in *Beams and Jets in Astrophysics*, 100
- Lupton, R. 1993, *Statistics in theory and practice* (Princeton, N.J.: Princeton University Press, 1993)
- Maron, J. & Goldreich, P. 2001, *Astrophys. Journ.*, 554, 1175
- Martin, P. G. 1978, *Cosmic dust. Its impact on astronomy* (Oxford Studies in Physics, Oxford: Clarendon Press, 1978)
- Mathewson, D. S. & Ford, V. L. 1970, *Mem. Roy. Astron. Soc.*, 74, 139
- Melrose, D. B. & Macquart, J.-P. 1998, *Astrophys. Journ.*, 505, 921
- Mohr, J. J., Mathiesen, B., & Evrard, A. E. 1999, *Astrophys. Journ.*, 517, 627
- Murgia, M., Govoni, F., Feretti, L., et al. 2004, accepted by A&A; ArXiv:astro-ph/0406225
- Niklas, S. 1995, Ph.D. Thesis

- Pacholczyk, A. G. 1970, Radio astrophysics. Nonthermal processes in galactic and extragalactic sources (Series of Books in Astronomy and Astrophysics, San Francisco: Freeman, 1970)
- Peres, C. B., Fabian, A. C., Edge, A. C., et al. 1998, *Mon. Not. Roy. Astron. Soc.*, 298, 416
- Perley, R. A. & Carilli, C. L. 1996, The structure and polarization of Cygnus A at λ 3.6cm (Cygnus A – Study of a Radio Galaxy), 168
- Perley, R. A. & Taylor, G. B. 1991, *Astron. Journ.*, 101, 1623
- Petrosian, V. 2001, *Astrophys. Journ.*, 557, 560
- Pfrommer, C. & Enßlin, T. A. 2004, *Astron. & Astrophys.*, 413, 17
- Razin, V. A. 1958, *Soviet Astronomy*, 2, 216
- Reid, A. D., Hunstead, R. W., Lemonon, L., & Pierre, M. M. 1999, *Mon. Not. Roy. Astron. Soc.*, 302, 571
- Reiprich, T. H. & Böhringer, H. 2002, *Astrophys. Journ.*, 567, 716
- Rephaeli, Y. & Gruber, D. 2003, *Astrophys. Journ.*, 595, 137
- Rephaeli, Y., Gruber, D., & Blanco, P. 1999, *Astrophys. Journ. Let.*, 511, L21
- Rephaeli, Y., Gruber, D. E., & Rothschild, R. E. 1987, *Astrophys. Journ.*, 320, 139
- Rephaeli, Y., Ulmer, M., & Gruber, D. 1994, *Astrophys. Journ.*, 429, 554
- Röttgering, H., Snellen, I., Miley, G., et al. 1994, *Astrophys. Journ.*, 436, 654
- Röttgering, H. J. A., Wieringa, M. H., Hunstead, R. W., & Ekers, R. D. 1997, *Mon. Not. Roy. Astron. Soc.*, 290, 577
- Rudnick, L. & Blundell, K. M. 2003, *Astrophys. Journ.*, 588, 143
- Ruzmaikin, A. A. & Sokoloff, D. D. 1979, *Astron. & Astrophys.*, 78, 1
- Ruzmaikin, A. A., Sokolov, D. D., & Shukurov, A. M. 1988, Magnetic fields of galaxies (Moscow, Izdatel'stvo Nauka, 1988, 280 p. In Russian.)
- Rybicki, G. B. & Lightman, A. P. 1979, Radiative processes in astrophysics (New York, Wiley-Interscience, 1979. 393 p.)
- Sarala, S. & Jain, P. 2001, *Mon. Not. Roy. Astron. Soc.*, 328, 623
- Scarrott, S. M., Ward-Thompson, D., & Warren-Smith, R. F. 1987, *Mon. Not. Roy. Astron. Soc.*, 224, 299
- Scheuer, P. A. G., Hannay, J. H., & Hargrave, P. J. 1977, *Mon. Not. Roy. Astron. Soc.*, 180, 163
- Schindler, S. & Prieto, M. A. 1997, *Astron. & Astrophys.*, 327, 37

- Simard-Normandin, M., Kronberg, P. P., & Button, S. 1981, *Astrophys. Journ. Supp.*, 45, 97
- Sokoloff, D. D., Bykov, A. A., Shukurov, A., et al. 1998, *Mon. Not. Roy. Astron. Soc.*, 299, 189
- Struble, M. F. & Rood, H. J. 1999, *Astrophys. Journ. Supp.*, 125, 35
- Sturrock, P. A. 1994, *Plasma Physics, An Introduction to the Theory of Astrophysical, Geophysical and Laboratory Plasmas* (Cambridge University Press, 1994.)
- Subramanian, K. 1999, *Phys. Rev. Let.*, 83, 2957
- Taylor, G. B., Fabian, A. C., & Allen, S. W. 2002, *Mon. Not. Roy. Astron. Soc.*, 334, 769
- Taylor, G. B., Govoni, F., Allen, S. W., & Fabian, A. C. 2001, *Mon. Not. Roy. Astron. Soc.*, 326, 2
- Taylor, G. B. & Perley, R. A. 1993, *Astrophys. Journ.*, 416, 554
- Taylor, G. B., Perley, R. A., Inoue, M., et al. 1990, *Astrophys. Journ.*, 360, 41
- Tribble, P. C. 1991, *Mon. Not. Roy. Astron. Soc.*, 250, 726
- Vallée, J. P. & Kronberg, P. P. 1975, *Astron. & Astrophys.*, 43, 233
- Venturi, T., Bardelli, S., Morganti, R., & Hunstead, R. W. 2000, *Mon. Not. Roy. Astron. Soc.*, 314, 594
- Verschuur, G. L. 1968, *The Observatory*, 88, 15
- Vogt, C., Dolag, K., & Ensslin, T. A. 2004, ArXiv:astro-ph/0401216
- Vogt, C. & Enßlin, T. A. 2003, *Astron. & Astrophys.*, 412, 373
- Wegner, G., Colless, M., Saglia, R. P., et al. 1999, *Mon. Not. Roy. Astron. Soc.*, 305, 259
- White, D. A. 2000, *Mon. Not. Roy. Astron. Soc.*, 312, 663
- Widrow, L. M. 2002, *Reviews of Modern Physics*, 74, 775
- Willson, M. A. G. 1970, *Mon. Not. Roy. Astron. Soc.*, 151, 1

Acknowledgements

Most of all, I am very thankful to Torsten Enßlin who as my supervisor has a great share of the success of this work. I would like to thank him, for all the endless discussions with him, motivations, inspiring thoughts, for pushing me to stay in science and for his support in daily fights. I am thanking him especially for that he never gave up explaining to me the beauty of mathematics. He almost succeeded!

I acknowledge financial support from the Deutsche Akademische Austauschdienst (DAAD) as a "Doktorandenkurzstipendium" which enabled me to go to the US for two months in summer 2002 where I visited the Very Large Array at Socorro. I like to thank Tracy Clarke who introduced me into the mysteries of radio data reduction with AIPS and who never got tired of telling me what a great fun such a thunderstorm can be. I would like to thank her also for being so patient with my slowly developing data reduction and observation skills. I want to thank the National Radio Astronomy Observatory in Socorro for its hospitality and I like to thank the people there for all the barbecues. I had great fun!

I would like to thank Greg Taylor, Jean Eilek, Federica Govoni, Chris Carilli and Frazer Owen for providing already reduced polarisation data sets of various extended radio sources. I want to thank Tracy Clarke, Melanie Johnston-Hollitt, Jean Eilek, Greg Taylor, Klaus Dolag and Phil Kronberg for all the numerous inspiring scientific and non-scientific discussions.

I would like to thank Huub Röttgering who offered me the possibility to go to the Sterrewacht Leiden for a couple of months on a NOVA Marie Curie stipend. I acknowledge financial support from the European Marie-Curie Association which is run by the European Union. A special thanks to Pedro and Inga who helped a homeless astrophysicist in a desperate situation. I would like to thank Melanie, who helped me a lot to survive in Leiden from a scientific point of view.

I acknowledge support from the European Community Research and Training Network *The Physics of the Intergalactic medium*, which I was a member of and which paid three great meetings for me. Furthermore, I would like to thank the International Max-Planck Research School on Astrophysics, which I was a member of during the last three years, for the lectures on astronomy and the social events.

I like to thank ASTRON in Dwingeloo for hosting me for a couple of days and for giving me a home for the next three years. Special thanks going to Robert Braun and Raffaella Morganti in assisting and helping with my Westerbork observation and data reduction.

I would like to thank Michaela, Conny and Juliane, who always listened to me when I called even late at night and who also offered me a bed at their apartment whenever I was around. Special thanks go to Jim who never got tired to motivate me

in his long emails and who always listened to my inner religious fights. I would like to thank Serena for introducing me into the art of driving a car in Munich and for all the pasta. I want to thank Pere for sharing the same addiction to fantasy books. Thanks to the rest of the bunch that you were there and made my life so enjoyable during the last three years.

Last but not least, I would like to thank my family who supported me wherever they could. Danke, dass ihr an mich glaubt!

CURRICULUM VITAE

Birth: August 25, 1976, Görlitz
Nationality: German

Education & Academical History

- *May 2003 - July 2003*
NOVA Marie Curie fellow at Leiden University, Netherlands. Advisor: Dr. Huub Röttgering.
- *June 2002 - August 2002*
Participation in the Synthesis Imaging Summer School in Radio Astronomy (*June 18 - 25, 2002*), Socorro, New Mexico, USA, followed by a visit at the National Radio Astronomy Observatory in Socorro, New Mexico, USA. Advisor: Dr. Tracy E. Clarke.
- *since September 2001*
PhD student of the International Max-Planck Research School (IMPRS) at the Max-Planck Institut für Astrophysik in Garching. Supervisor: Dr. Torsten Enßlin.
Thesis title: "Investigations of Faraday Rotation Maps of Extended Radio Sources in order to determine Cluster Magnetic Field Properties".
Participation in the "European Research Training Network - The Physics of the Intergalactic Medium".
- *September 1999 - June 2001*
Diploma in Physics at the University of Leipzig, Germany.
Thesis: "Untersuchungen zur Porenraumstruktur von porösen Medien mittels NMR-Diffusometrie und -Bildgebung" ("Investigations of porous materials using NMR-Diffusion and -Tomography techniques")
- *September 1998 - August 1999*
First Class Honours BSc. degree in "Environmental Physical Science" at Napier University of Edinburgh, Scotland, UK.
advanced project: "Modelling the energy Balance of the Earth".
- *October 1995 - August 1998*
study of Physics at the University of Leipzig, Germany.
- *June 1995*
Abitur at 4th Gymnasium "Königshufen", Görlitz, Germany.
- *September 1983 - June 1995*
19th Polytechnische Oberschule, after the German reunification 4th Gymnasium "Königshufen", Görlitz, Germany.

Publications

Journals

1. *A Bayesian View on Faraday Rotation Maps – Seeing the Magnetic Power Spectrum in Galaxy Clusters*
Corina Vogt and Torsten A. Enßlin, submitted to *A&A*, (2004).
2. *Pacman II: Application and Statistical Characterisation of Improved RM maps*
Corina Vogt, Klaus Dolag and Torsten A. Enßlin, submitted *MNRAS*, (2004).
3. *Pacman I: A new algorithm to calculate Faraday Rotation Maps*
Klaus Dolag, Corina Vogt and Torsten A. Enßlin, submitted to *MNRAS*, (2004).
4. *Measuring the Cluster Magnetic Field Power Spectra from Faraday Rotation Maps of Abell 400, Abell 2634 and Hydra A*
Corina Vogt and Torsten A. Enßlin, *A&A*, 412, 373-385 (2003).
5. *Are Faraday Rotating Magnetic Fields Local to Intracluster Radio Galaxies?*
Torsten A. Enßlin, Corina Vogt, T. E. Clarke, Greg B. Taylor, *ApJ*, 597, 870-877 (2003).
6. *The Magnetic Power Spectrum in Faraday Rotation Screens*
Torsten A. Enßlin and Corina Vogt, *A&A*, 401, 835-848 (2003).
7. *Self-diffusion studies of pore fluids in unconsolidated sediments by PFG NMR*
Vogt C., Galvosas P., Klitzsch N., Stallmach F., *J. of Appl. Geophys.*, 50, 455-467 (2002).
8. *Fractal Geometry of Surface Areas of Sand Grains Probed by Pulsed Field Gradient NMR*
Stallmach F., Vogt C., Kärger J., Helbig K., Jacobs F., *Phys. Rev. Lett.*, 88, 10, 105505 (2002).

Conference Proceedings

9. *Magnetic fields and cosmic rays in cooling flows,*
Enßlin T. A , Vogt, C., Pfrommer, C, 2003 in *The Riddle of Cooling Flows in Galaxies and Clusters of Galaxies* eds. Reiprich, T. H., Kempner, J. C., and Soker, N., astro-ph/0310028.
To be published electronically at <http://astro.virginia.edu/coolflow/>.
10. *PFG NMR self-diffusion studies of fluid transport and surface-to-volume ratios in sands*
Stallmach F., Vogt C., Galvosas P., Kärger J., Klitzsch N., *Magn. Reson. Imaging*, 19, 584 (2001).